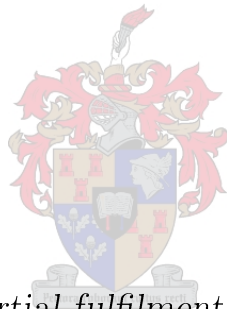


Modelling of a fuel cell propulsion system for multicopters

by

Matthew Kapp



*Thesis presented in partial fulfilment of the requirements for
the degree of Master of Engineering (Mechanical) in the
Faculty of Engineering at Stellenbosch University*

Supervisor: Dr. W.J. Smit

April 2019

Declaration

By submitting this thesis electronically, I declare that the entirety of the work contained therein is my own, original work, that I am the sole author thereof (save to the extent explicitly otherwise stated), that reproduction and publication thereof by Stellenbosch University will not infringe any third party rights and that I have not previously in its entirety or in part submitted it for obtaining any qualification.

Date: April 2019

Copyright © 2019 Stellenbosch University
All rights reserved.



UNIVERSITEIT • STELLENBOSCH • UNIVERSITY
jou kennisvennoot • your knowledge partner

Plagiaatverklaring / Plagiarism Declaration

- 1 Plagiaat is die oorneem en gebruik van die idees, materiaal en ander intellektuele eiendom van ander persone asof dit jou eie werk is.
Plagiarism is the use of ideas, material and other intellectual property of another's work and to present it as my own.
- 2 Ek erken dat die pleeg van plagiaat 'n strafbare oortreding is aangesien dit 'n vorm van diefstal is.
I agree that plagiarism is a punishable offence because it constitutes theft.
- 3 Ek verstaan ook dat direkte vertalings plagiaat is.
I also understand that direct translations are plagiarism.
- 4 Dienooreenkomstig is alle aanhalings en bydraes vanuit enige bron (ingesluit die internet) volledig verwys (erken). Ek erken dat die woordelike aanhaal van teks sonder aanhalingstekens (selfs al word die bron volledig erken) plagiaat is.
Accordingly all quotations and contributions from any source whatsoever (including the internet) have been cited fully. I understand that the reproduction of text without quotation marks (even when the source is cited) is plagiarism.
- 5 Ek verklaar dat die werk in hierdie skryfstuk vervat, behalwe waar anders aangedui, my eie oorspronklike werk is en dat ek dit nie vantevore in die geheel of gedeeltelik ingehandig het vir bepunting in hierdie module/werkstuk of 'n ander module/werkstuk nie.
I declare that the work contained in this assignment, except where otherwise stated, is my original work and that I have not previously (in its entirety or in part) submitted it for grading in this module/assignment or another module/assignment.

Studentenommer / Student number	Handtekening / Signature
Voorletters en van / Initials and surname	Datum / Date

Abstract

Modelling of a fuel cell propulsion system for multicopters

M. Kapp

*Department of Mechanical and Mechatronic Engineering,
University of Stellenbosch,
Private Bag X1, Matieland 7602, South Africa.*

Thesis: MEng (Mech)

April 2019

Multicopters are used in many applications - PwC predicts that drones have a potential market value of \$ 127.3 bn. It is expected that if beyond-visual-line-of-sight becomes legalized, current multicopter flight time will be insufficient in these applications, and investment in increasing multicopter flight time will increase. The most mature technology to increase multicopter UAV flight time is fuel cells. This technology has been proven to increase the flight time two-to threefold, compared to LiPo-based multicopters, the current state-of-the-art technology. However, these multicopter systems are more complex to design, and no publicly-available software design tools exist.

In order to solve this, a software design tool was developed. The components of a fuel cell multicopter system were modelled. Models were developed in Matlab/SimscapeTM. Experimental data was obtained using either the author's own experiments, data from manufacturers or data found in literature. The experimental data was then used to identify the unknown model constants.

The component models are quite accurate, with the error mostly being small in comparison to the effect of varying a parameter. Also, %RMSE values are mostly below 3% and the R^2 values are all greater than 0.97.

These component models were combined to form a design tool. The usefulness of the design tool was demonstrated by running a preliminary optimization study - the flight time was maximized with battery remaining state of charge as a constraint. A theoretical design was obtained with 2.39 hours flight time and 38 % SOC remaining.

Uittreksel

Modellering van 'n brandstofsels-stelsel vir hommeltuie

(“Modelling of a fuel cell propulsion system for multicopters”)

M. Kapp

*Departement Meganiese en Megatroniese Ingenieurswese,
Universiteit van Stellenbosch,
Privaatsak X1, Matieland 7602, Suid Afrika.*

Tesis: MIng (Meg)

April 2019

Multirotors word in baie toepassings gebruik - PwC voorspel dat drones 'n potensiële markwaarde van \$ 127,3 miljard het. Daar word verwag dat indien die buite-visuele lyn van sig gewettig word, die huidige multirotoriese vlugtyd onvoldoende sal wees in hierdie aansoeke, en belegging in toenemende multirotoriese vlugtyd sal toeneem. Die mees volwasse tegnologie om multirotoriese UAV-vlugtyd te verhoog, is brandstofselle. Hierdie tegnologie het bewys dat die vlugtyd twee- tot drievoudig vergroot word, in vergelyking met LiPo-gebaseerde multirotors, die huidige state-of-the-art tegnologie. Hierdie multirotor-stelsels is egter meer kompleks om te ontwerp, en daar bestaan geen publieke beskikbare sagtewareontwerpgereedskap nie.

Om dit op te los, is 'n sagteware-ontwerpinstrument ontwikkel. Die komponente van 'n brandstofsels multirotoriese stelsel is gemodelleer. Modelle is ontwikkel in Matlab/SimscapeTM. Eksperimentele data is verkry deur gebruik te maak van óf die outeur se eie eksperimente, data van vervaardigers of data wat in die literatuur voorkom. Die eksperimentele data is dan gebruik om die onbekende modelkonstantes te identifiseer.

Die komponentmodelle is redelik akkuraat, met die fout meestal klein in vergelyking met die effek om 'n parameter te verander. Ook, % RMSE waardes is meestal minder as 3 % en die R^2 waardes is almal groter as 0.97.

Hierdie komponentmodelle is gekombineer om 'n ontwerpgereedskap te vorm. Die nut van die ontwerpgereedskap is getoon deur 'n voorlopige optimaliseringsstudie uit te voer. Die vlugtyd is gemaksimeer met die oorblywende toestand van die battery as 'n beperking. 'n Teoretiese ontwerp is verkry met 2.39 hure vlugtyd en 38 % SOC oorblywend.

Acknowledgements

I would like to express my sincere gratitude to the following people and organisations ...

I would like to thank my supervisor Dr W.J. Smit. My project is not in line with his normal research focus, so I'd therefore like to thank him for deciding to take me on as a student. I would like to thank him for being hands-on i.t.o. flying a drone with me, and for providing the necessary advice and assistance to complete this thesis. I would like to thank him especially for helping me narrow the scope and obtain a logical, consistent theme throughout the thesis.

I would like to thank HySA Systems. I would like to thank Daniel van Schalkwyk for assisting me with an experimental setup, and providing relevant knowledge. I would like to thank Adrian Parsons for making this project possible. I would like to thank him for providing access to equipment, facilities and funding, and providing assistance.

I would like to thank Graham Newton at Skyhook Remote Aerial Solutions. He has built and rebuilt about 40 drones over the last 9 years. I had the opportunity to obtain some of this knowledge and experience, and get some practical perspective on drones.

I would like to thank STERG. This group provided me with PC equipment and office space. I would like to thank my colleagues in this group, and other students, where the casual conversations gave helpful insights for my project. I would like to thank Jurgens, Dylan and Kemal.

I would like to thank my family and friends for their support. I would like to thank my Lord and Saviour, Jesus Christ, for being a rock during this time, and giving me the motivation and wisdom to complete this project.

Contents

Declaration	i
Abstract	iii
Uittreksel	iv
Acknowledgements	v
Contents	vi
List of Figures	viii
List of Tables	xi
Nomenclature	xiii
1 Introduction	1
1.1 Background	1
1.2 Specific problem	2
1.3 Gap in literature and design tools	3
1.4 Approach to solve the problem	5
1.5 Objectives	8
2 Literature review	9
2.1 Fuel cell power supply system	9
2.2 Battery	17
2.3 Electrical drive system	22
2.4 Propeller	26
3 Power supply subsystem modelling	27
3.1 Overview of data used	29
3.2 Fuel cell	30
3.3 Battery	37
3.4 Power management system	47
3.5 Tank	57

4	Load subsystem modelling	58
4.1	Propulsor system	58
4.2	Thrust duty cycle and parasitic loss	68
5	System model	76
5.1	Initial design	76
5.2	sensitivity study	79
6	Conclusion	81
6.1	Summary of findings	81
6.2	Implications of this work	81
6.3	Limitations of this work	81
6.4	Recommended future research	82
	Appendices	83
A	Discussion of scope limitations in this project	84
B	Modelling of system used to obtain transient fuel cell model	86
B.1	Fuel cell steady-state model	86
B.2	Battery transient model	87
B.3	Battery steady-state model	87
B.4	Diode model	88
B.5	Summary	89
C	Calibration of current sensor	90
D	Battery and fuel cell models for PMS data	92
D.1	Fuel cell	92
D.2	Battery	92
E	Simulation with power management system	95
F	Mechanical motor model and propeller model constants	98
G	Validation of ESC model	100
G.1	Description of model	100
G.2	Data used	101
G.3	Fitting and validating model	102
H	Propulsor system modelling - additional data	105
I	Thrust duty cycle converting - additional data	110
	List of References	111

List of Figures

1.1	Comparing complexity of LiPo and fuel cell propulsion system . . .	4
1.2	Overview of fuel cell multirotor	6
2.1	Operating principle of fuel cell	10
2.2	Functional overview of generalized fuel cell power supply system . .	11
2.3	Hydrogen supply configuration	12
2.4	Closed-cathode	12
2.5	Open-cathode	13
2.6	Humidification	13
2.7	Cooling	14
2.8	Power management	16
2.9	Different modes of operation of passive PMS	18
2.10	Four instances of voltage transients in battery	20
2.11	n-RC equivalent circuit model	20
2.12	Hybrid pulse power characterisation tests	21
2.13	Simplified single phase electrical drive model	22
2.14	Comparison circuit configurations of ESC-BLDC and DC-DC buck converter	24
2.15	DC-DC equivalent circuit model	25
2.16	Three-constant motor electrical model	25
3.1	Overview of power supply system configuration	27
3.2	Components of the power supply system	28
3.3	Overview of data used in Chapter 3	29
3.4	Electrical model of fuel cell	31
3.5	Steady-state fuel cell electrical model	31
3.6	Experimental setup and results from literature, used to obtain fuel cell transient model. The load is stepped from 3 A to 12 A.	32
3.7	Components and sub-components to be modelled	33
3.8	Model parameters obtained, representing experimental setup	34
3.9	Comparison of model and experimental results - indicator of accu- racy of fuel cell transient electrical model	35
3.10	Comparison of experimental versus model results of <i>HES Aerostaks</i> fuel cells	36

3.11	Analysis to obtain mass flowrate versus current relationship	37
3.12	Simulink model of hydrogen fuel consumption	38
3.13	Battery equivalent circuit models	39
3.14	Experimental setup	40
3.15	Phase 1: constant-current discharge curves	43
3.16	Phase 2: Hybrid pulse power characterisation test	43
3.17	Phase 2: constant-current discharge tests	44
3.18	Phase 2: constant-current-constant-voltage charge tests	45
3.19	Experimental setup 1	48
3.20	Experimental setup 2	49
3.21	Data of modes 1 and 2	50
3.22	Operation of charging system	51
3.23	Different phases of battery charging	52
3.24	Charging battery from starting voltage of 21 V	53
3.25	Charging battery from starting voltage of 23 V	54
3.26	Voltage vs current for different fuel cell voltages	55
3.27	Simscape implementation of PMS model	57
3.28	Hydrogen mass versus empty tank mass for discrete tank sizes	57
4.1	Load subsystem model overview	58
4.2	Propulsor system model overview	59
4.3	Mechanical motor model and propeller	60
4.4	Comparison between model fit and manufacturer data - Torque - Modelling friction	61
4.5	Comparison between model fit and manufacturer data - Torque - Not modelling friction	62
4.6	Comparison between model fit and manufacturer data - Thrust	62
4.7	R^2 values of mechanical motor model and propeller model fit	63
4.8	ESC equivalent circuit model	63
4.9	Propulsor model implemented in Simulink	64
4.10	Comparison between model fit and manufacturer data - complex model	65
4.11	Comparison between model fit and manufacturer data - simple model	66
4.12	Comparing R^2 values of complex model with simple model	67
4.13	Measured power during flight test	69
4.14	Thrust versus power of the propulsor used in the flight test	70
4.15	Geometric analysis to estimate thrust duty cycle with a different all-up-mass	71
4.16	Comparison of experimental and model thrust duty cycle versus time	72
4.17	Thrust control system implementation in Simulink	73
4.18	Simulation result - comparing actual and setpoint thrust versus time	74
4.19	Simulink model of parasitic loss	74
5.1	Simulink system model	77

LIST OF FIGURES

x

5.2	Capacity remaining over entire simulation	77
5.3	Simulation measurements over short timespan	78
5.4	Simulation results as a function of varying battery rated capacity and hydrogen tank mass	80
A.1	Proposed overview of larger project	85
B.1	Experimental setup divided into sub-models	86
B.2	Fuel cell model	87
B.3	Battery transient model	87
B.4	Battery steady-state model	88
B.5	Diode data from datasheet - fit with model	89
B.6	Model constants obtained for experimental setup - excluding fuel cell transient model	89
C.1	Obtaining calibration curve	90
C.2	Modifying calibration equation	91
D.1	Fuel cell model	92
D.2	Constant-current discharge data	93
E.1	Validating phase 3 (Equation 3.21)	95
E.2	Validating phase 3 (Equation 3.21)	96
E.3	Validating phase 1 and 2 with different load currents (Equation 3.22)	97
G.1	ESC equivalent circuit model	100
G.2	Experimental setup	101
G.3	Comparison between Gong model and equivalent circuit model - simple model	102
G.4	Comparison between Gong model and equivalent circuit model - complex model	103
G.5	Estimated parameters for different supply voltages - complex model	103
G.6	Comparison between accuracy of complex model and simple model	104
I.1	Battery voltage measured during flight	110

List of Tables

1.1	Comparison of fuel cell multirotor UAV's with LiPo multirotor UAV's	2
1.2	Summary of approach	7
2.1	Categorization of fuel cells	11
3.1	Details of components used in experimental setup	32
3.2	Results of obtaining the fuel cell transient electrical model	33
3.3	Details of components used in experimental setup	41
3.4	Phase 1: Model parameters and %RMSE values	42
3.5	Phase 2: Model parameters	44
3.6	Phase 2: %RMSE and V_0 values	45
3.7	Time duration power values are kept constant	49
3.8	Details of components used in experimental setup	50
3.9	Constants for Equation 3.19 to 3.21	53
3.10	Constants for Equation 3.24	56
4.1	Propulsor combinations: manufacturer data used for fitting model	59
4.2	Propulsor components on quadcopter used in flight test	69
4.3	Comparison of mean and standard deviation for the experimental and model thrust duty cycle	71
4.4	Component masses of power supply system	73
5.1	Components used in initial design system simulation	76
5.2	Simulation results for the initial design	78
5.3	Comparison of initial design with design obtained from sensitivity study	80
D.1	Battery model constants	93
D.2	Battery model parameters altered to better data in Section 3.4	94
F.1	Mechanical motor model and propeller model constants	99
G.1	Details of experimental setup	102
H.1	Model parameters: comparing values obtained from model fit to manufacturer-provided values	106

LIST OF TABLES

xii

H.2

Complex propulsor model values

107

H.2

Complex propulsor model values

108

H.3

Simple propulsor model values

109

Nomenclature

Abbreviations

BEMF	Back electromotive force
BOP	Balance-of-plant
BVLOS	Beyond-visual-line-of-sight
CAN	Controller area network
CC	Constant-current
CCCV	Constant-current-constant-voltage
COTS	Commercial-off-the-shelf
CV	Constant-voltage
ESC	Electronic Speed Controller
ECM	Equivalent circuit model
FC	Fuel cell
HPPC	Hybrid pulse power characterization
HV	High voltage
LiHV	Lithium high voltage
LiPo	Lithium polymer
LV	Low voltage
OCV	Open circuit voltage
PEMFC	Proton exchange membrane fuel cell
PMS	Power management system
RMS	Root mean squared
RMSE	Root mean squared error
SOC	State of charge
SOH	State of health
UAV	Unmanned Aerial Vehicle

Constants

$$F = 96485.333 \text{ C/mol}$$

$$M_{H_2} = 96485.333 \text{ g/mol}$$

$$R_{H_2} = 41242.2 \text{ J/(kg} \cdot \text{K)}$$

Variables

A	Empirical constant	[]
C	Capacity	[Ah]
C	Capacitance	[F]
C	Constant	[]
D	Derivative control gain	[]
D	Diameter	[m]
I	Current	[Ampere]
I	Integral control gain	[]
K	Empirical constant	[]
k	Empirical constant	[]
L	Inductance	[H]
m	Mass	[kg]
\dot{m}	Mass flowrate	[g/s]
N	Filter coefficient	[]
N	Number of cells	[]
P	Power	[W]
P	Pressure	[Pa, bar]
P	Proportional control gain	[]
Q	Torque	[N·m]
R	Resistance	[Ω]
T	Temperature	[K]
T	Thrust	[N]
t	Time	[s]
V	Voltage	[Volts]
Z	Impedance	[Ω]
z	State of charge	[]
α	Duty cycle, throttle	[]
η	Efficiency	[]
Δt	Timestep	[s]
λ	Stoichiometry	[]
ω	Angular velocity	[rad/s]
ρ	Density	[kg/m ³]

Subscripts

bat Battery

bmc	Maximum voltage to which battery is charged
CC	Constant-current
$cond$	Conduction
D	Drain
DD	Drain-to-drain
DS	Drain-to-source
i	Discrete value current timestep
int	Internal
f	Friction
n	Nominal
n	Number
OC	Open circuit
P	Propeller
SW	Switching
Q	Torque
T	Thrust
threshold	Minimum allowable value
0	Maximum, initial or no-load value

Chapter 1

Introduction

1.1 Background

1.1.1 Drone overview

Unmanned Aerial Vehicles (UAV's) can be grouped into three main groups: fixed-wing UAV's, multirotor UAV's and hybrids (a combination of these). All these types of UAV's are loosely referred to as drones. Multirotor UAV's will be the focus of this work.

PWC (2016) predicts that drones have a potential market value of \$ 127.3 bn. Goldman Sachs (2016) predicts that drones have a potential market value of \$ 100 bn over the period of 2016 - 2020. The value of global drone sales in 2017 was R 12 bn (Botha, 2018). Botha (2018) predicts for the year 2018 that the drone industry will contribute R 10.7 bn to the South African economy, with 56 706 jobs created in South Africa.

The current state-of-the-art energy storage technology for multirotor UAV's is lithium polymer (LiPo) batteries. The technology's limited flight time has been a significant problem, but hasn't limited its sales (Guinn and Schauble, 2018). With beyond-visual-line-of-sight (BVLOS) being legalised, it is expected that increased flight time will become worth investing in (Guinn and Schauble, 2018).

There are a number of potential energy storage technologies that could increase the flight time of multirotor UAV's. These include lithium-air, microsupercapacitors, aluminum-air, solid-state lithium-ion and fuel cells. Out of all these technologies, fuel cells are considered to be the most mature (Hoy and Kutnick, 2017; Wang, 2018; Gartner, 2013).

1.1.2 Specifically fuel cell drones

There has been significant interest in the use of fuel cell multirotors. Table 1.1 lists some fuel cell multirotors available. Some of them are compared to the

LiPo equivalent on which they are based, and some are compared to a LiPo multirotor with similar size and payload capacity.

Table 1.1: Comparison of fuel cell multirotor UAV's with LiPo multirotor UAV's (DJI, 2017, 2018^{a,b}; EnergyOr, 2018; Horizon Energy Systems, 2018; Intelligent Energy, 2017; MMC, 2016; FlightWave, 2018)

Fuel cell UAV			Similar LiPo UAV		
Product	Maximum payload	Flight time (no payload)	Product	Maximum payload	Flight time (no payload)
Intelligent Energy (IE) 650 W DJI Matrice M100	500 g	1 hour 15 min	DJI Matrice M100 (2 x TB48D batteries)	493 g	40 min
MMC HyDrone 1800	5 000 g	3 hours	DJI Matrice M600 (TB48S batteries)	5 500 g	40 min
FlightWave Jupiter UAS (using IE system)	1 000 g	3 hours	FlightWave Jupiter UAS (with LiPo)	1 000 g	1 hr
EnergyOr H2QUAD 400	400 g	3 hours 45 min			
HES Hycopter	2 500 g ¹	3 hours 30 min ¹			

Some of these fuel cell multirotors are finding use in commercial and military applications. Intelligent Energy (IE) is working with PINC, a company specializing in yard and warehouse management for vehicle logistics, to use fuel cell multirotors in real-time inventory tracking (FCB, 2017). EnergyOr supplies their fuel cell multirotors to the French Air Force (Ene, 2016).

1.2 Specific problem

Multirotor UAV's are used for a variety of different missions. A multirotor UAV is quite expensive and it is often a compromise between flight time, payload and stability, amongst other factors. It is therefore normally custom-designed for the specific application (DroneTec, 2018). DJI has 12 different

¹Different flight times and payloads are achieved by using different sized tanks

multi-rotor UAV's that were registered with the Federal Aviation Authority (FAA) of USA for commercial use in 2017 (Guinn and Schauble, 2018).

Designing the propulsion system for a LiPo multirotor UAV is a relatively standard process. The propulsion system is composed of a battery, electronic speed controller (ESC), motor and propeller. Characteristic curve data of the ESC/motor/propeller combinations are given by the manufacturers with certain parameters varied, such as supply voltage, KV value, propeller diameter and number of blades (T-motor, 2017a,b; KDE Direct). Batteries can be fairly well characterised by simply knowing the number of cells and capacity (Gatti *et al.*, 2015), which is provided by most manufacturers (Gens Ace Tattu; Turnigy).

A fuel cell propulsion system is more complex than a LiPo propulsion system for the following high-level reasons:

1. The energy is stored in one component (usually a hydrogen tank), and the power is supplied by another component, the fuel cell. With a LiPo system, the energy is stored by the battery and the power is supplied by the battery. This means that with a LiPo system, the energy available scales linearly with battery mass (Gatti *et al.*, 2015). This is not the case with a fuel cell system (Intelligent Energy, 2017).
2. A LiPo battery has quite a high power density. It is therefore able to handle the range of currents drawn by the load. With a fuel cell, this is not the case. It has a higher energy density, allowing longer flight time, but it has a lower power density, meaning it would be sized too large if it were to handle the entire current range. A fuel cell is normally hybridized with a battery to combine the fuel cell's higher energy density with the battery's higher power density.

The resulting increased complexity of the power supply system is shown in Figure 1.1. A battery is replaced with a hydrogen tank, fuel cell, battery and power management system (PMS). Due to the increased complexity of the system, the design and analysis process would naturally also be more complex.

1.3 Gap in literature and design tools

The problem can be defined as follows: there is no computer program design tool that can be used to design a fuel cell propulsion system for a multirotor UAV, for a specific application. There is also limited information or literature available to aid in the design process. However, a fuel cell multirotor can be considered an evolution of two more mature fields: LiPo multirotor UAV's and fuel cell fixed-wing UAV's.

For LiPo multirotors, useful design tools exist, such as e-Calc (xcopterCalc), and MIT's multicopter design software. eCalc contains manufacturer data

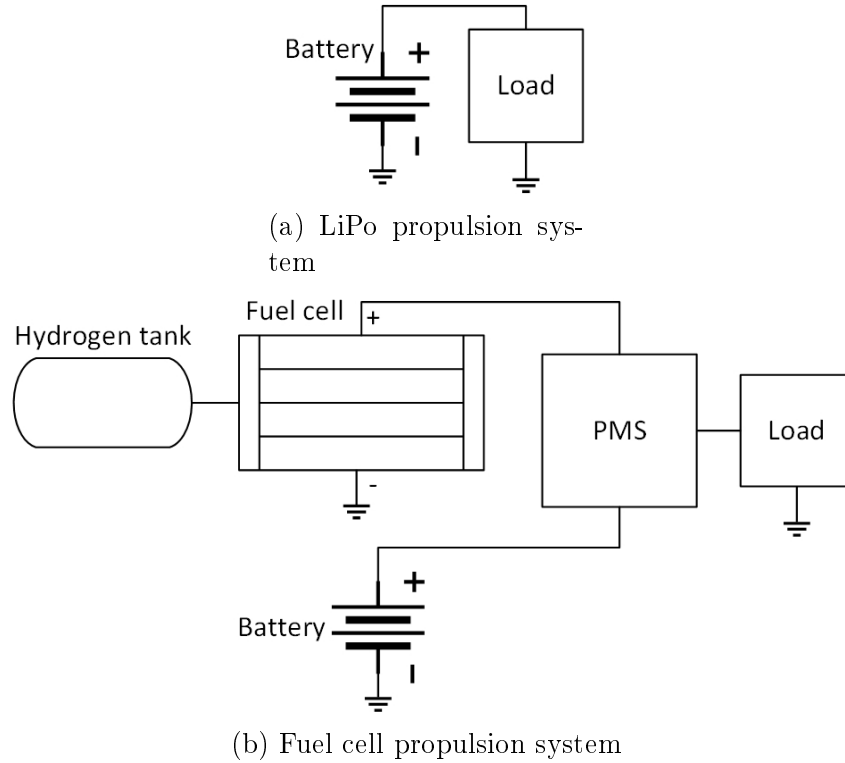


Figure 1.1: Comparing complexity of LiPo and fuel cell propulsion system

of many components by different manufacturers (Müller). This allows the designer to change the components on the software, and obtain information of the predicted performance, feasibility of a design and other information. MIT's software takes things a step further by combining propulsion system, geometry and control system design (Du *et al.*, 2016; Tao Du, Adriana Schulz). However, this software is stored on Github, which makes it less convenient than eCalc, which is an online tool.

There is also a significant amount of academic literature on the design of LiPo multirotors. Mauro Gatti (2015) developed a preliminary design procedure, Ampatis and Papadopoulos (2014) conducted a sensitivity analysis, Eva Saadé Latorre (2011) developed an iterative design procedure and Benito *et al.* (2014) made use of eCalc to compare different designs. Magnussen *et al.* (2014); Bershadsky *et al.* (2016) made use of optimization algorithms to best size the propulsion system.

With fuel cell fixed-wing UAV's there aren't any software design tools, to the author's knowledge. However, there is a significant amount of academic literature. It is known that with these aircraft, due to the constraints of fuel cells, the aircraft needs to be optimized for low power consumption with well matched components (Röckler, 2012). Design optimization studies have been done by Bradley *et al.* (2008); Moffitt *et al.* (2006, 2007).

The most useful information on designing a fuel cell multirotor UAV is a

white paper by Protonex/Ballard, a fuel cell manufacturer (Sisco *et al.*, 2017). The authors did simple calculations to predict the flight time of a DJI Matrice M600, modified to run on a fuel cell system. However, the authors themselves admit that some of their analysis is for illustration purposes only. The authors state that more comprehensive trade studies and design analyses should be conducted, to determine the optimal propulsion system configuration for an application.

1.4 Approach to solve the problem

The problem is the lack of tool available to assist designers in designing a fuel cell multirotor propulsion system. This problem will be solved by developing a partly validated mathematical model that can be used to conduct sensitivity studies, to aid in designing a fuel cell multirotor propulsion system.

The different components of a fuel cell multirotor propulsion system is shown in Figure 1.2. The *flight control system* does not form part of the propulsion system, but the parasitic power loss due to it, is included. Each of the components in Figure 1.2 will be modelled. Different approaches will be followed for each of the components. However most of the approaches will have the following in common:

1. The models will be either mathematical equations, electric circuits or a combination thereof. They will be mainly based on existing literature.
2. The model parameters will be obtained by fitting the model to experimental data. The experimental data will be obtained either from literature or the manufacturer or the author's experiments.
3. The models will be implemented in Matlab/Simulink/Simscape. The fitting will be done using a Matlab function for equations or Simulink's *Parameter Estimation* for circuits.
4. The model output will be compared to the experimental data output. The goodness of fit will be quantified by either %RMSE or R^2 values. If the fit is good, the component model is considered to be validated.

The end goal of the system model is to be able to do sensitivity studies i.e. vary certain parameters, and view the effect of the system output. Therefore, the validity of varying these parameters should be checked. this is done in one of two ways:

1. The model is validated using more than one dataset i.e. with different values of the independent variable.

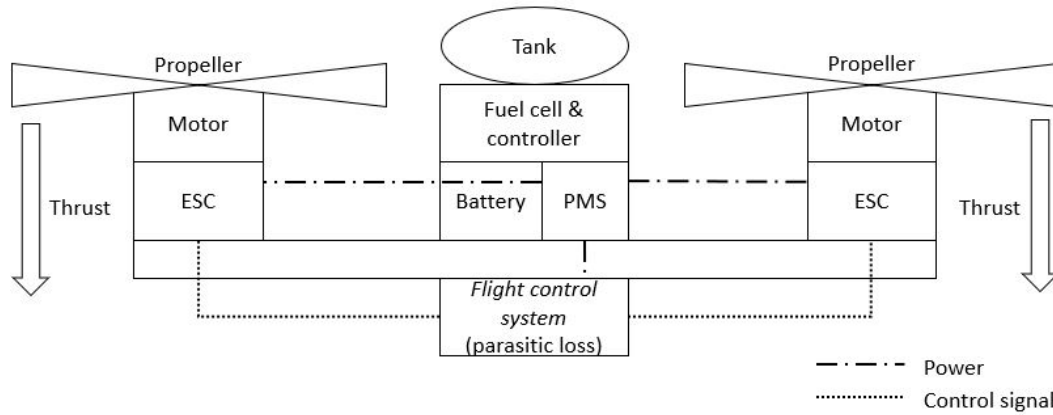


Figure 1.2: Overview of fuel cell multirotor - components that are modelled in this work

2. The model is validated using only one dataset i.e. with only one value for the independent variable. Equations from literature are used to vary the parameters.

A summary of how the data is obtained for each component, how the parameter variation is validated and which parameters can be varied, is summarised in Table 1.2.

The different components can be grouped together according to the following sub-approaches:

1.4.1 Modelling the electrochemical devices

The fuel cell and battery are the electrochemical devices. They will be modelled using a similar approach. The model is divided into a steady-state and a transient model. The transient model reduces to zero with time, resulting in the overall model being equal to the steady-state model with time. Steady-state data is used to validate the steady-state model, and step-response data is used to validate the transient model.

1.4.2 Modelling the propulsor system

The propulsor system refers to the combination of the electronic speed controller (ESC), motor and propeller. Manufacturer data is used. One motor type and one propeller type is used. The propeller model parameters are obtained first, then the model parameters of the motor and ESC are obtained. The model is only validated using steady-state data, and it is set up to change state instantaneously. However, the transients will be modelled, because the thrust duty cycle is a dynamic load profile.

Table 1.2: Summary of approach

Component/ subsystem	Data used	Parameter variation - based on	Parameters varied (discrete or continuous)
Hydrogen tank	Other manufacturer	Data used	Tank mass [kg] (continuous)
Fuel cell	Manufacturer; Literature; Other manufacturer	None	None
Battery	Author's experiments	Literature	Capacity [Ah] (continuous); Number of cells (discrete)
PMS	Literature	Data used	Capacity [Ah] (continuous); Number of cells (discrete)
ESC/motor/ propeller	Manufacturer	Data used	Propeller diameter [inch] (continuous); KV value (discrete)
Thrust duty cycle	Author's experiments	Data used	All-up-mass [kg] (continuous)
Parasitic loss	Author's experiments	None	None

1.4.3 Modelling the power management system

Data from literature is used. A model is developed to fit this data. The data used has fairly simple inputs. It is checked whether the model works for more complex inputs.

1.4.4 Modelling the thrust duty cycle and parasitic loss

Experimental flight data of a LiPo multirotor is obtained with the same flight path, but with different all-up-masses. This data is used to validate a model thrust duty cycle model, that predicts the thrust required as a function of the all-up-mass. The parasitic power loss is also obtained from this data, and implemented as a constant-power sink.

1.5 Objectives

The following objectives are to be achieved:

1. All the component and subsystem models need to be validated.
2. It needs to be demonstrated that the system model shows the dynamic behaviour of the different components.
3. The predicted flight time of the system model needs to be close to that of a similar fuel cell multicopter product.
4. It needs to be demonstrated that the system model can be used for a sensitivity study. This will be done by varying the energy storage parameters i.e. the tank mass and the battery capacity.

The scope is limited in the following way:

1. The system model won't be validated, only the component/sub-system models will be validated.
2. It won't be demonstrated that a sensitivity study can be done with all possible parameters, but will only be done with two parameters.

The reasoning behind deciding which objectives are included in the scope, and which are not, is discussed in Appendix A.

Chapter 2

Literature review

2.1 Fuel cell power supply system

Most of the information and diagrams in this section are adapted from (Barbir, 2013*a,b*), unless otherwise specified.

2.1.1 Fuel cell stack operating principle

There are different types of fuel cells, differentiated by the type of electrolyte used. The type most suited to UAV applications is a proton exchange membrane fuel cell (PEMFC) (Gong and Verstraete, 2017*b*). It uses a thin proton conductive polymer membrane as the electrolyte. This means that the membrane conducts protons, but not electrons.

The operating process is shown in Figure 2.1. Hydrogen and oxygen are at opposite sides of the membrane. There is an attraction between the hydrogen and oxygen to bond and form water. Hydrogen (H_2) dissociates to form two protons (H^+) and two electrons ($-$). The membrane only allows H^+ to pass through. The electron takes a path of less resistance, moving through the external circuit to get to the oxygen. This movement of electrons produces DC current in the external circuit.

At the interface between the electrodes and the membrane is a catalyst. This catalyst is typically composed of platinum supported on carbon. The electrodes are porous structures. The porous media allow the gases to flow through, while increasing the surface area for electrochemical reactions.

2.1.2 Overview of fuel cell power supply subsystem

Figure 2.1 shows the operation of a *fuel cell stack*. In order for the stack to operate, it requires auxiliary functions. The system required to fulfill these auxiliary functions is termed the *balance-of-plant (BOP)*.

The auxiliary functions required to be fulfilled are *water management*, *heat management*, *hydrogen supply* and *oxygen supply*. The *BOP* combined with

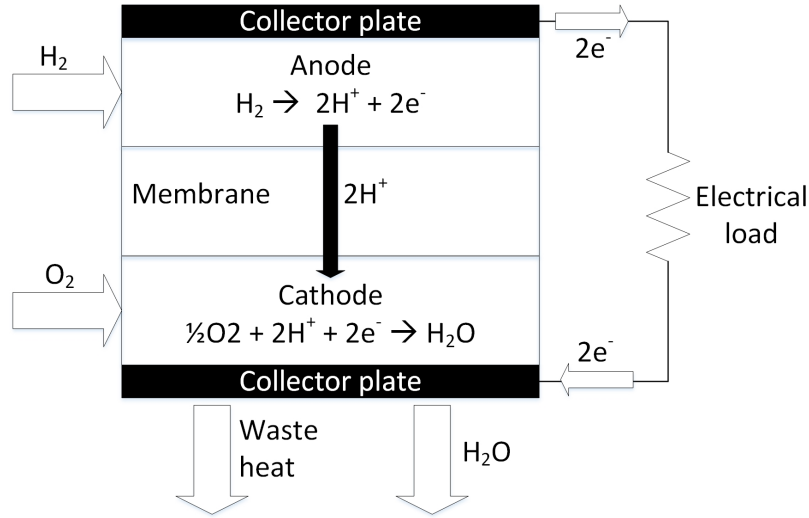


Figure 2.1: Operating principle of fuel cell

the *fuel cell stack* forms the *fuel cell system*, as shown in Figure 2.2. For UAV applications, the *fuel cell system* is hybridized with a *battery* using a *power management system*. The hydrogen also needs to be stored. All of these systems combined forms the *fuel cell power supply system*.

The different functions shown in Figure 2.2 can be performed using different methods. These different methods are summarised in Table 2.1, and described in detail in Sections 2.1.3 to 2.1.8. The *Type used in this work* refers to the methods used in most fuel cell multirotor systems, and more specifically the system procured. These design choices are made by the fuel cell system manufacturers. These choices are most likely made for the following reasons: all these design choices are the simplest and therefore lightest option. These simple solutions seem to work with low-powered applications (around 1 kW) and at low altitude.

2.1.3 Hydrogen supply

Hydrogen needs to be supplied to the anode. If a high pressure tank is used to store hydrogen, a pressure-reducing valve is required to reduce the pressure to the operating pressure of the anode. Hydrogen can be supplied either in dead-end (Figure 2.3a) or flow-through (Figure 2.3b) configuration (Chen *et al.*, 2013).

Dead-end is when hydrogen flow is blocked by a *purge valve* on the outlet of the anode. This causes the hydrogen to remain within the anode, and to be consumed in the chemical reactions. These reactions, combined with movement across the membrane, cause impurities, such as water and nitrogen to build up (Chen *et al.*, 2013). This build-up damages the fuel cell and causes the voltage to drop. Therefore, the purge valve is opened periodically for a

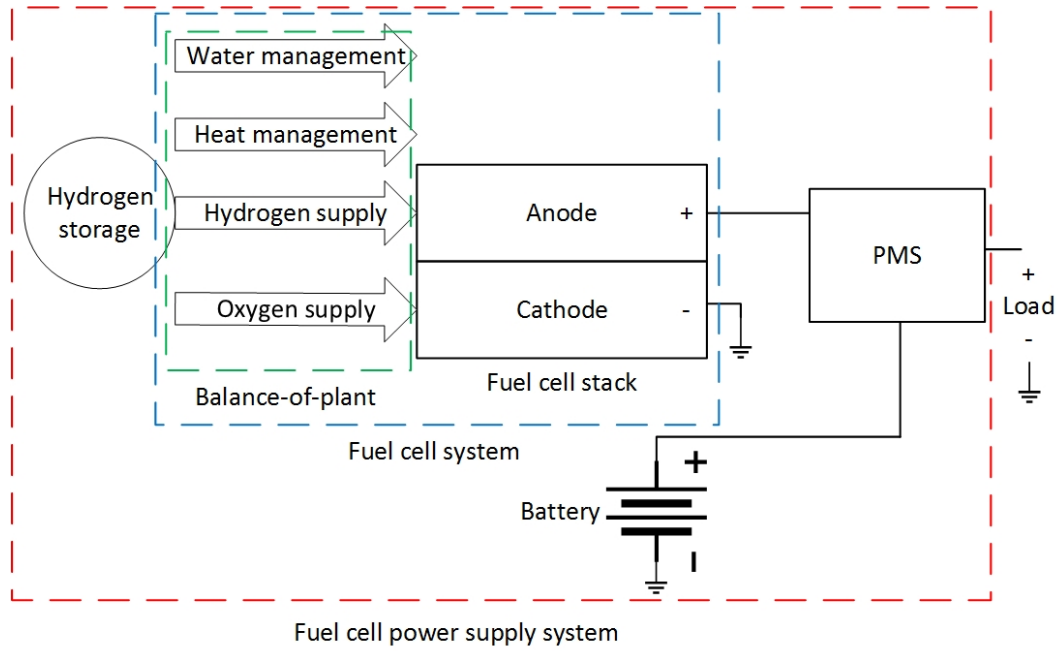


Figure 2.2: Functional overview of generalized fuel cell power supply system

Table 2.1: Categorization of fuel cells

Component	Type used in this work	Other types
Hydrogen supply	Dead-end	Through-flow
Oxygen supply	Open-cathode	Closed-cathode
Water management	Internally (self) humidified	Externally humidified
Heat management	Air-cooled	Liquid coolant cooled
Hydrogen storage	High pressure gas tank	Cryogenic tank (liquid storage); Chemical hydrogen generation
Power management system	Passive	Active

short period of time to remove impurities building up within the anode.

Flow-through is when hydrogen supplied to the anode is allowed to exit. More hydrogen is supplied than required. Some of it is used up in the chemical reactions. Some of it flows out the outlet. This hydrogen that flows out the outlet is captured and recycled i.e. allowed to re-enter the anode. The recycling of hydrogen is done using either a pump or an ejector. A water separator removes water from the hydrogen at the outlet.

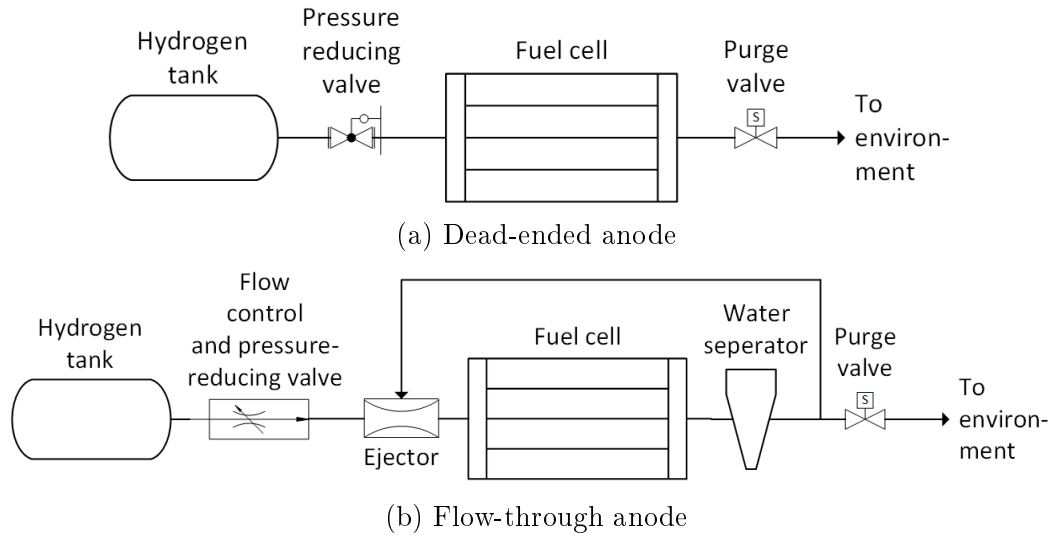


Figure 2.3: Hydrogen supply configuration

2.1.4 Oxygen supply

The cathode is the part of the fuel cell where oxygen is supplied. It can be either an open-cathode or a closed-cathode fuel cell. A close-cathode fuel cell is one where the oxygen flow channel is internal and isolated from the environment. An open-cathode fuel cell is one where the oxygen flow channel is external and open to the environment.

A closed-cathode system (Figure 2.4) requires a relatively high-powered turbo-machine to supply air which can overcome the losses of the internal flow channel. The cathode removes the oxygen from the air in order to perform the chemical reactions. Alternatively a compressed pressure vessel containing oxygen can be used.

In an open-cathode fuel cell, the cathode is open to the environment. Therefore, the cathode can remove the oxygen directly from the air for the chemical reactions. The cells could be stacked in such a way that a low-powered turbo-machine is required to overcome the losses, to supply all the cells' cathodes with oxygen, as shown in Figure 2.5.

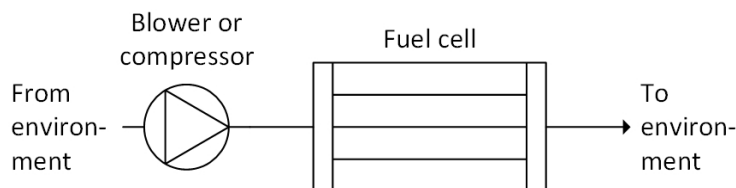


Figure 2.4: Closed-cathode

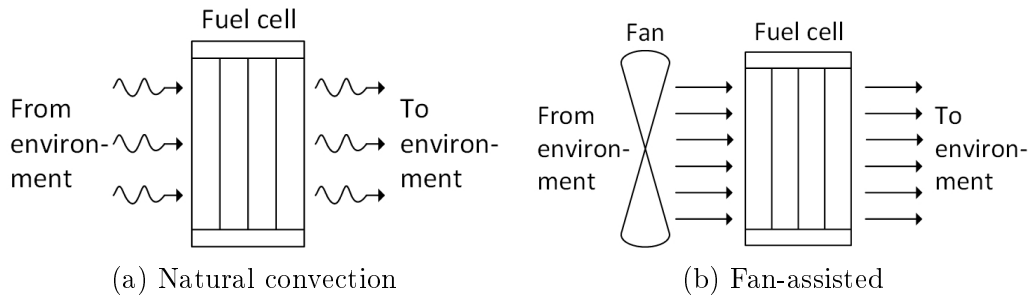


Figure 2.5: Open-cathode

2.1.5 Water management

The anode and cathode is required to be at a certain humidity level in order to obtain the required performance, and to reduce degradation. Humidification can be done either internally or externally.

Internal humidification is when the operation of the fuel cell itself is altered periodically in order to keep the anode and cathode at their required humidity levels. One method of doing this is by periodically disconnecting the fuel cell from the load and short circuiting the fuel cell, as shown in Figure 2.6a.

External humidification is where the hydrogen and air/oxygen is humidified before entering the anode and cathode inlets, as shown in Figure 2.6b.

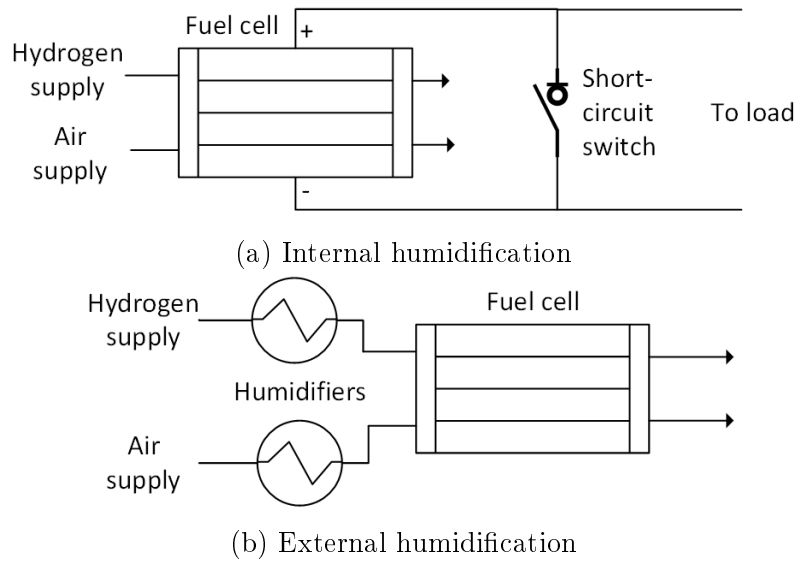


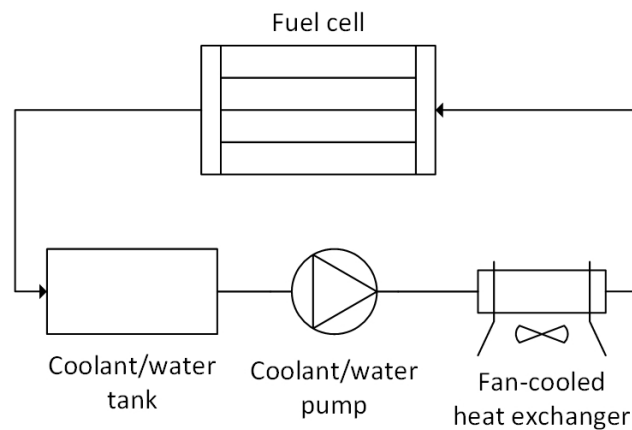
Figure 2.6: Humidification

2.1.6 Heat management

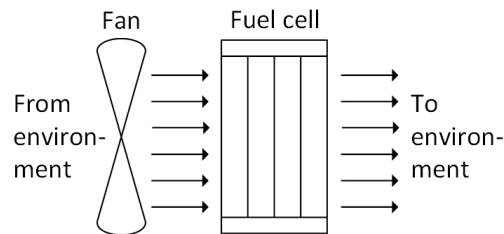
The fuel cell needs to operate at a certain temperature for optimal performance (50 - 80 °C for low-temperature PEMFC). The fuel cell is around 50 % efficient, causing internal heat generation. Cooling is therefore required to remove some of the heat generated. This cooling can be either done internally or externally.

Internal cooling involves flowing a coolant within the fuel cell. This coolant is then cooled externally, as shown in Figure 2.7a. This is normally used for closed-cathode fuel cells.

External cooling involves blowing air onto the fuel cell, as shown in Figure 2.7b. This is normally done in open-cathode fuel cells.



(a) Internal cooling



(b) External cooling

Figure 2.7: Cooling

2.1.7 Hydrogen storage

Hydrogen needs to be stored on board the vehicle, and then supplied to the anode. The different methods of doing this are *compressed gas storage*, *cryogenic liquid storage* and *chemical hydrogen generation*.

With *compressed gas storage*, hydrogen gas is stored in a pressure vessel at a high pressure. The gas pressure is then reduced, using a pressure reducer, to a pressure that is acceptable for the fuel cell.

With *cryogenic liquid storage*, hydrogen is stored at a very low temperature. Hydrogen is then allowed to boil off, to supply the anode with hydrogen gas. A very complex system is used to store hydrogen as liquid.

With *chemical hydrogen generation*, hydrogen is stored as a solid chemical compound. A chemical process occurs, allowing the hydrogen to disassociate from the compound, so that it can be supplied to the anode.

2.1.8 Power management system

In most cases, especially with UAV's, the fuel cell is hybridized with a energy storage component with a higher power density . The component most commonly used is a lithium battery. The power management system (PMS) manages the power flow between three subsystems, namely the fuel cell, the battery and the load. This can be achieved either by a passive system or an active system.

A fuel cell is normally hybridized with another power source, such as a battery, for the following reasons (Gong and Verstraete, 2017b):

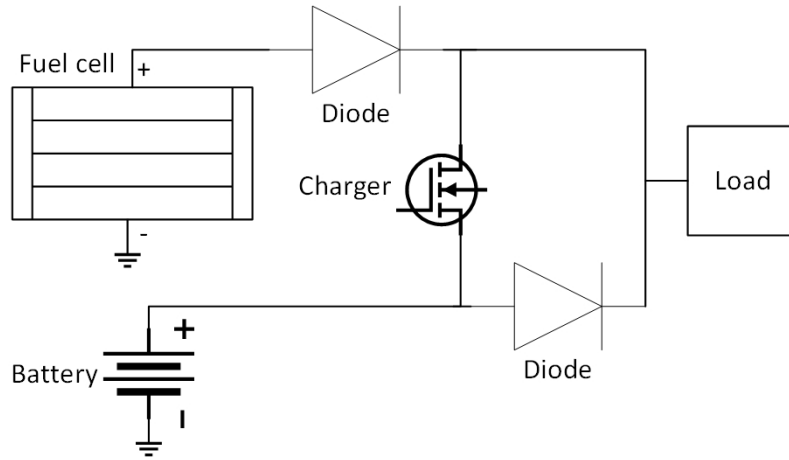
1. It has a low power density, resulting in it having either insufficient power at certain instances of high power required, or being oversized, adding unnecessary mass. This would result in a design far from optimal if only a fuel cell is used. In the case of a multirotor, the specific instances of high power include keeping stable in a wind gust or rapid maneuvering.
2. A fuel cell has a slow response to a sudden increase in power required (Nishizawa *et al.*, 2013).
3. Drawing high current from a fuel cell causes the voltage to drop to a level that damages the fuel cell (Nishizawa *et al.*, 2013).

The system used to hybridize these two power sources is normally referred to as a PMS, and can be categorized as either passive or active (Gong and Verstraete, 2017b; Nishizawa *et al.*, 2013).

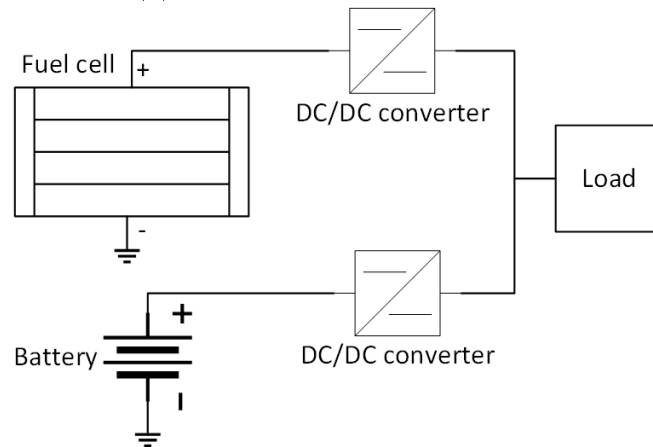
A passive system is one in which the fuel cell, battery and load are directly connected with passive components (such as diodes) in-between them (Nishizawa *et al.*, 2013), as shown in Figure 2.8a. The load voltage determines the power sharing between the fuel cell and battery (Gong and Verstraete, 2017b). However, an active charging system is required to control the power flow between the fuel cell and battery. The diodes can be replaced with *ideal diodes*, which is a controlled switching system that mimics the behaviour of diodes (i.e. prevents reverse current flow), but has lower losses (Howroyd and Chen, 2016).

An active system makes use of actively controlled electronics (such as DC-DC converters) to control the power flow between the fuel cell, battery and load (Blackwelder and Dougal, 2004). The configuration can be either series

or parallel (Howroyd and Chen, 2016), with either the battery (Chen *et al.*, 2013), fuel cell (Han *et al.*, 2014) or both (Tsotoulidis and Safacas, 2011) being connected to a DC/DC converter. An example configuration is shown in Figure 2.8b.



(a) Passive power management



(b) Active power management - Parallel connected with DC/DC converter for fuel cell and battery

Figure 2.8: Power management

2.1.8.1 Operation of passive power management system

There are three modes of operation of a passive PMS. Mode 1 is when power is drawn only from the fuel cell (Figure 2.9a). Mode 2 is when power is drawn from the fuel cell and battery (Figure 2.9b). Mode 3 is when power is drawn from the fuel cell, and additional power is drawn from the fuel cell to charge the battery (Figure 2.9c).

Steady-state operation of modes 1 and 2 is characterised by the following equations (Nishizawa *et al.*, 2013):

$$\begin{aligned} \text{mode 1:} \quad & I_{\text{Load}} = I_{\text{Fuel cell}} \quad \text{when} \quad V_{\text{Fuel cell}} > V_{OC} \\ & I_{\text{Battery}} = 0 \end{aligned} \quad (2.1)$$

$$\begin{aligned} \text{mode 2:} \quad & V_{\text{Fuel cell}} = V_{\text{Battery}} \\ & I_{\text{Load}} = I_{\text{Fuel cell}} + I_{\text{Battery}} \quad \text{when} \quad V_{\text{Fuel cell}} \leq V_{OC}, \end{aligned} \quad (2.2)$$

where V_{OC} is the open-circuit voltage (OCV) of the battery.

Experimental results of modes 1 and 2 is shown in Figure 2.9d. The OCV is 25.2 V. When the load voltage is greater than this, the battery current is zero, and current is only drawn from the fuel cell. When the load voltage is less than the OCV, current is drawn from the fuel cell and battery. Looking at the data points, when $V_{\text{Fuel cell}} \approx V_{\text{Battery}}$ ($21.5V \approx 21.6V$), $I_{\text{Load}} = I_{\text{Fuel cell}} + I_{\text{Battery}}$ ($28.4A \approx 12.6A + 16.1A$), which obeys equation 2.2.

With mode 3, the battery charging is controlled using a MOSFET (Gong and Verstraetey, 2014). If it is a lithium battery, the MOSFET is controlled using a constant-current-constant-voltage algorithm (Gong and Verstraetey, 2014).

2.2 Battery

In this section, the methods most commonly used to model batteries is reviewed. These modelling methods are based on state of charge (SOC). SOC is therefore first described. Certain experiments are used in literature to obtain the necessary data to identify and validate battery models. These experimental procedures and the setups used are reviewed.

2.2.1 State of charge

Most of this section is obtained from (Plett, 2004).

State of charge is defined as the ratio of the remaining capacity to the nominal capacity of the cell. It is mathematically defined as follows:

$$z(t) = z(0) - \int_0^T \frac{\eta I(t)}{C_n} dt \quad \text{where} \quad \eta \begin{cases} = 1 & \text{for discharge} \\ \leq 1 & \text{for charge} \end{cases}, \quad (2.3)$$

where $z(t)$ is the SOC, η is the Coulombic efficiency, I is the instantaneous current (assumed positive for discharge, negative for charge), and C_n is the nominal capacity.

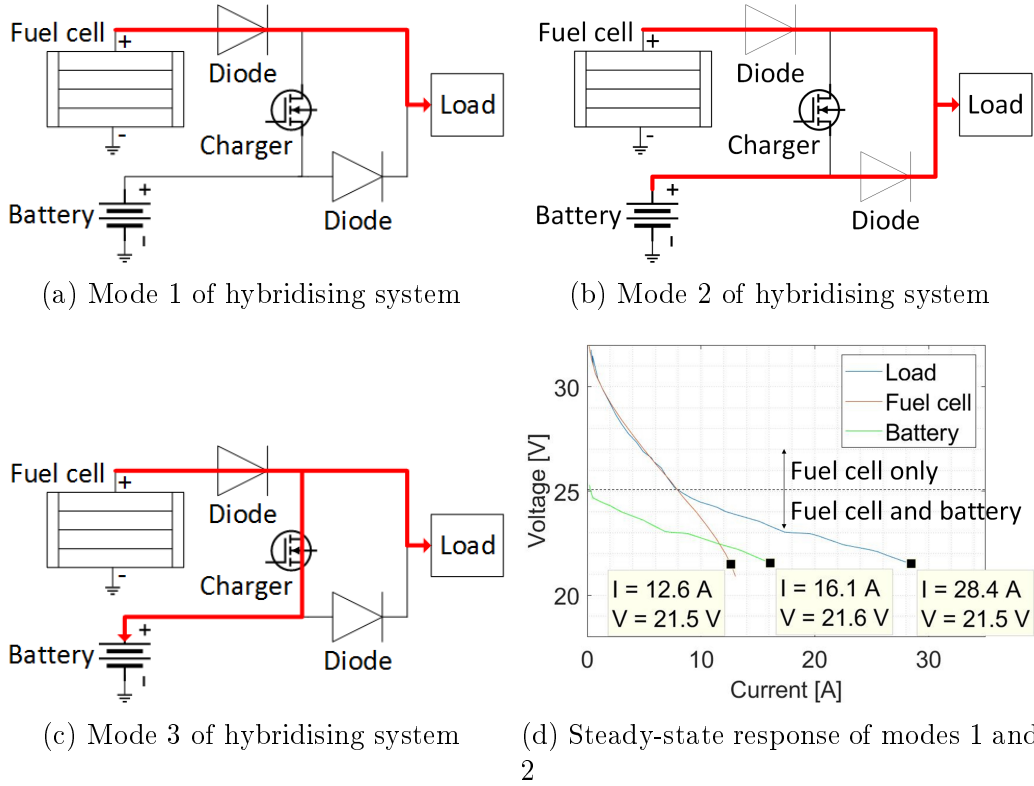


Figure 2.9: Different modes of operation of passive PMS. Adapted from (Nishizawa *et al.*, 2013; Gong and Verstraetey, 2014)

The value of z ranges from 0, for fully discharged, to 1, for fully charged. The nominal capacity is defined as the number of ampere-hours that can be drawn from the cell at room temperature while being discharged at a current value of $C/30$, starting with the cell fully charged. It is normally 5% greater than the rated capacity (the capacity on the label) (Mathworks, 2008).

Using a rectangular approximation for integration and a "suitably small" sampling period Δt , a discrete-time approximate recurrence of Equation 2.3 may then be written as:

$$z_{i+1} = z_i - \left(\frac{\eta \Delta t}{C_n} \right) I_k \quad \text{where} \quad \eta \begin{cases} = 1 & \text{for discharge} \\ \leq 1 & \text{for charge} \end{cases} \quad (2.4)$$

2.2.2 Models

The different methods of modelling batteries include (Farag, 2013): *ideal models*, *behavioural models*, *equivalent circuit models* and *electro-chemical models*. *Behavioural models* and *equivalent circuit models* are mostly used in literature (Hussein and Batarseh, 2011; Nejad *et al.*, 2016). These models are therefore reviewed here.

2.2.2.1 Behavioural model

Plett (2004) compiled the following behavioural models:

$$\text{General Shepherd equation: } V = V_0 - RI - \frac{K}{z} \quad (2.5)$$

$$\text{Unnewehr universal model: } V = V_0 - RI - Kz \quad (2.6)$$

$$\text{Nernst model: } V = V_0 - RI + K_1 \ln(z) + K_2 \ln(1 - z), \quad (2.7)$$

where V is the battery voltage, V_0 is the maximum battery open-circuit voltage, R is the internal resistance, I is the instantaneous current, z is the SOC and K_n are empirical constants.

Plett (2004) then combined these equations to form his *combined model*:

$$V = V_0 - RI - \frac{K_1}{z} - K_2 z + K_3 \ln(z) + K_4 \ln(1 - z) \quad (2.8)$$

The limitation of these models is that they don't model transient effects. Tremblay and Dessaint (2009) used a behavioural model based on Shepherd's model to model transient behaviour. They did this by having the instantaneous current values pass through a low-pass filter. However, transient behaviour is mostly modelled using equivalent circuit models, as described in Section 2.2.2.2.

2.2.2.2 Equivalent circuit model

There is a delayed change in the voltage of a battery when there is a step change in the current (Plett, 2018). Equivalent circuit models (ECMs) characterise this transient behaviour (Rahmoun and Biechl, 2012; Hussein and Batarseh, 2011). There are 4 instances of this delayed voltage response: discharge on, discharge off, charge on and charge off (Rahmoun and Biechl, 2012). These instances are shown in Figure 2.10.

A typical ECM is the n-RC model (Guangming *et al.*, 2014; Jackey *et al.*, 2013; Nejad *et al.*, 2016; Lai *et al.*, 2018), shown in Figure 2.11. The model includes the open-circuit voltage (OCV), V_{OC} , the series resistance, R_0 , and the parallel RC-branches, R_n and C_n . The OCV is a function of SOC (Rahmoun and Biechl, 2012; Hussein and Batarseh, 2011; Nejad *et al.*, 2016; Plett, 2018).

One method of modelling V_{OC} is by using a look-up table with OCV vs SOC values (Jackey *et al.*, 2013; He *et al.*, 2011; Hussein and Batarseh, 2011). A second method is using a behavioural model (such as those in Section 2.2.2.1) and removing the RI term. An example is Plett's combined model (Plett, 2004):

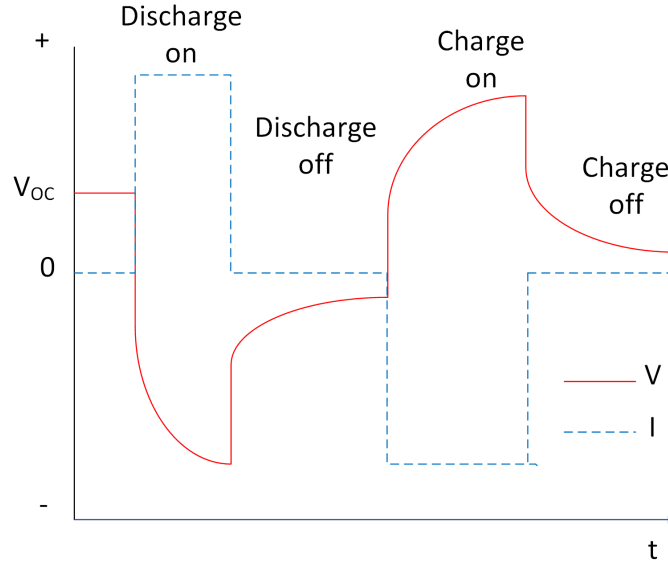


Figure 2.10: Four instances of voltage transients in battery - charge on and off, and discharge on and off. Adapted from (Rahmoun and Biechl, 2012)

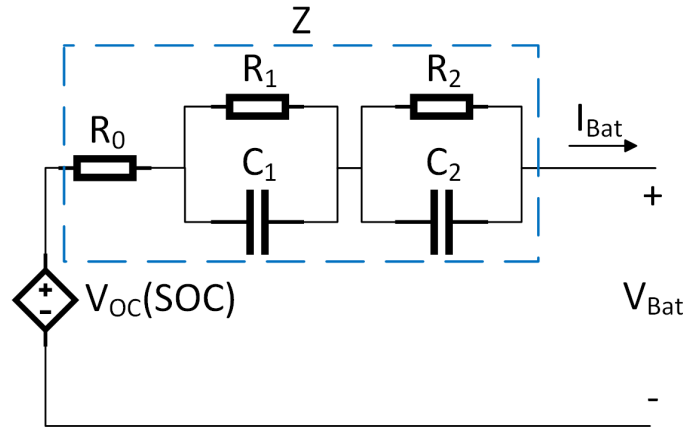


Figure 2.11: n-RC equivalent circuit model. Adapted from (Guangming *et al.*, 2014)

$$V = \underbrace{V_0 - \frac{K_1}{z} - K_2 z + K_3 \ln(z) + K_4 \ln(1 - z)}_{V_{OC} = f(\text{SOC})} - RI \quad (2.9)$$

The drawback of these models is that they require a complex experimental setup, with time consuming procedures.

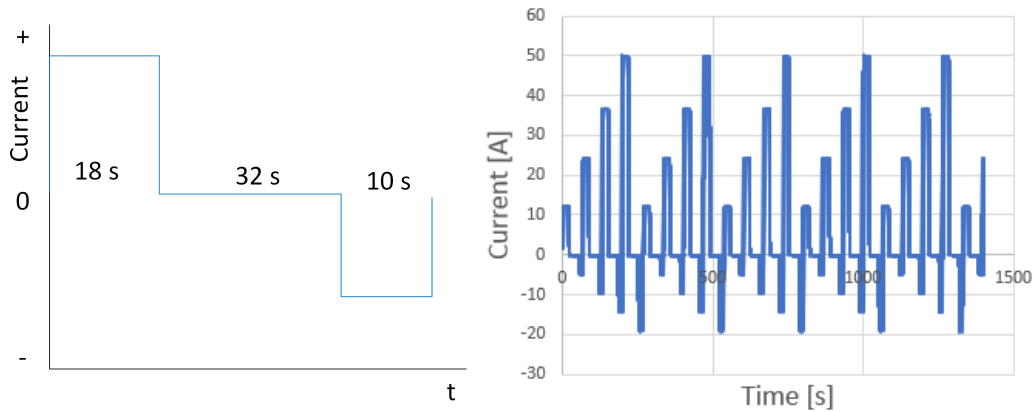
2.2.3 Review of experimental setups and procedures

Experimental setups used for characterizing Lithium batteries is reviewed. This section is divided into the type of experiments done, and the functionality required of the experimental setups.

2.2.3.1 Type of experiments

Here follows a review of the type of experiments done with lithium batteries:

1. *Constant-current discharge*: The battery is discharged at a constant current value from its maximum voltage to its minimum voltage (Lu *et al.*, 2017).
2. *Constant-current-constant-voltage charge*: Constant-current-constant-voltage (CCCV) charging involves charging the battery from being "empty" to being fully charged, using a sequence of first constant current, then constant voltage (Lu *et al.*, 2017). The test is stopped when the charge current reaches a specified lower limit. The voltage and current values are specified by the manufacturer.
3. *Hybrid Pulse Power Characterization*: Hybrid Pulse Power Characterization (HPPC) is a standard test outlined in (Hunt, 2003). It involves discharging, resting and charging the battery in a repetitive manner (Johnson, 2002; Nejad *et al.*, 2016), as shown in Figure 2.12a. An example where the maximum and minimum current values are altered is shown in Figure 2.12b.



(a) Simple HPPC profile - single charge and discharge current values. Adapted from (Nejad *et al.*, 2016)
 (b) Complex HPPC profile - multiple charge and discharge current values. Adapted from (Mocera and Vergori, 2018)

Figure 2.12: Hybrid pulse power characterisation tests

2.2.3.2 Functionality of experimental setups

Here follows a review of the type of functionality required by an experimental setup (Mocera and Vergori, 2018; He *et al.*, 2011; Lai *et al.*, 2018; Lu *et al.*, 2017):

1. *Power sinking*: The system needs to be able to sink power, causing the battery to be discharged.
2. *Power sourcing*: The system needs to be able to source power, causing the battery to be charged.
3. *Temperature control*: The system needs to contain a chamber that can keep the battery at a setpoint temperature.
4. *Measuring/logging*: The system needs to measure and log data. The parameters of interest are current, voltage and temperature of the battery.

2.3 Electrical drive system

The electrical drive system is composed of an electronic speed controller (ESC) and a brushless DC motor (BLDCM). This is a three phase electrical system. However, it can be reduced to a single phase system DC system (Silvagni *et al.*, 2018), because of the following assumptions based on the operation of a BLDC motor: mutual inductance between phases can be ignored, the flux distribution is trapezoidal, the induced currents due to stator harmonic fields, iron and stray losses are neglected. The resulting model of a simplified ESC-BLDC model commonly used is shown in Figure 2.13. This section reviews theory and models of the ESC and BLDCM.

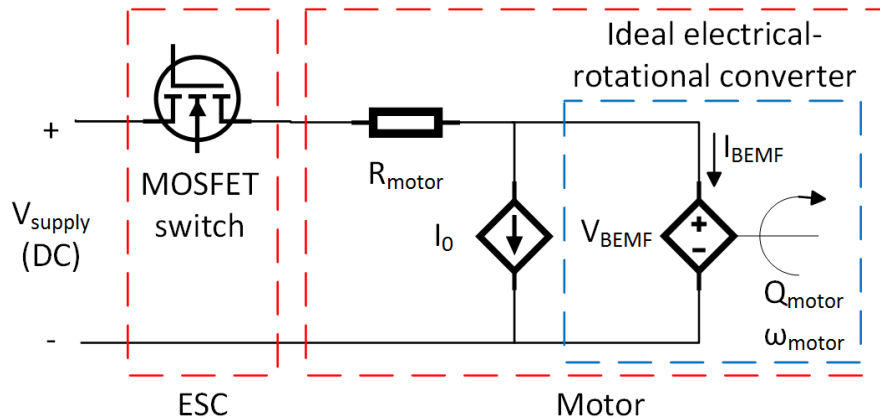


Figure 2.13: Simplified single phase electrical drive model. Adapted from (Green and McDonald, 2015)

2.3.1 Electronic speed controller

The main loss component in an ESC is the MOSFET switch. The losses in a MOSFET can be characterised by Equations 2.10 and 2.11, which take into account the losses during conduction and switching respectively:

$$\text{MOSFET conduction loss: } P_{cond} = I_{D_{RMS}}^2 R_{DS(on)}, \quad (2.10)$$

where $I_{D_{RMS}}$ is the RMS current through the MOSFET (drain current) and $R_{DS(on)}$ is the MOSFET internal resistance (drain-to-source resistance).

$$\text{MOSFET switching loss: } P_{SW} = \frac{1}{2} I_{D(on)} V_{DD} (t_{on} + t_{off}) f_{sw}, \quad (2.11)$$

where $I_{D(on)}$ is the maximum drain current, V_{DD} is the maximum drain voltage, t_{on} is the time taken to switch on the MOSFET, t_{off} is the time taken to switch off the MOSFET and f_{sw} is the switching frequency.

These losses can be modelled using a *behavioural model* or an *equivalent circuit model*.

2.3.1.1 Behavioural model

Gong and Verstraete (2017a) developed Equation 2.12 based on Equations 2.10 and 2.11:

$$\begin{aligned} P_{ESC_{loss}} &= P_{in} - P_{cond} - P_{SW} - P_{idle} \\ &= VI_{D_{RMS}} - DR_{DS(on)}I_{D_{RMS}}^2 - \frac{1}{2}I_{D_{RMS}}V(t_{on} + t_{off})f_{sw} - P_{idle}, \end{aligned} \quad (2.12)$$

where $P_{ESC_{loss}}$ is the total ESC power loss, P_{in} is the power in to the ESC, P_{idle} is the idle power loss, assumed to be a constant, V is the DC input voltage and $I_{D_{RMS}}$ is the DC input current.

The authors fit a modified version of Equation 2.12 to experimental data of UAV ESC-BLDCM's. The authors obtained R^2 values of greater than 0.91.

The main drawback of this approach is that the three-phase electrical signals between the ESC and motor need to be measured (Gong and Verstraete, 2017a; Harrington and Kroninger, 2013). These signals are irregular and at a high frequency (Infineon, 2016; Gong and Verstraete, 2017a). Therefore, expensive equipment is required (Green and McDonald, 2015).

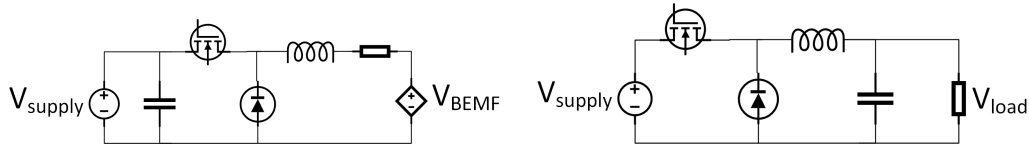
2.3.1.2 Equivalent circuit model

The power loss is modelled using a single resistor, representing the MOSFET drain-to-source resistance, $R_{DS(on)}$, in Equation 2.10 (Ampatis and Papadopoulos, 2014). There are a few problems with this approach: $R_{DS(on)}$ is

unknown (MOSFET product codes aren't provided by ESC manufacturers), and therefore the value is assumed; it is assumed that three phases are conducting simultaneously, which is not the case as only two phases conduct at any given time; this model wasn't validated with experimental data.

2.3.1.3 Comparing ESC to a DC-DC buck converter

The models described above (Sections 2.3.1.1 and 2.3.1.2) merely characterise the power losses in the ESC, but do not characterise the ESC's main function of regulating the speed. The ESC provides the desired voltage amplitude to the motor by use of switching (Marshall *et al.*, 2016), in order to regulate its speed. A DC-DC converter also provides a desired output voltage by use of switching (Erickson; Enrique *et al.*, 2017). The type of DC-DC converter that only reduces the voltage amplitude is a buck converter (Erickson). A comparison of a buck converter topology with an ESC-BLDCM system operating during one phase is shown in Figure 2.14. It can be seen that their topologies and operation is quite similar, the main difference being the capacitor placed at different positions.



(a) One phase of operation of BLDC. (b) DC-DC buck converter. Adapted from (Ramya and Krishna Kumar, 2016)

Figure 2.14: Comparison circuit configurations of ESC-BLDC and DC-DC buck converter

A DC-DC converter can be modelled by dividing it up into an ideal transformer, and losses, as shown in Figure 2.15. With a buck converter, the *voltage conversion ratio* is equal to the *duty cycle* (Erickson). The ideal power conversion equations then become (Mathworks):

$$V_{out} = \alpha V_{in} \quad (2.13)$$

$$I_{in} = \alpha I_{out}, \quad (2.14)$$

where α is the duty cycle, a value from 0 to 1.

2.3.2 Motor

The motor is modelled using a three constant model, with the constants being K_V , R and I_0 . This model is shown in Figure 2.16. The following equations

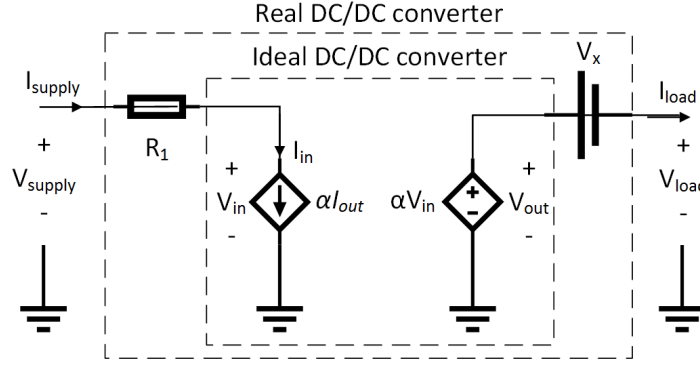


Figure 2.15: DC-DC equivalent circuit model. Adapted from (Enrique *et al.*, 2017)

characterise the electrical-rotational converter component of this model (Green and McDonald, 2015):

$$T_{motor} = K I_{BEMF} \quad (2.15)$$

$$V_{BEMF} = K \omega_{motor} \quad (2.16)$$

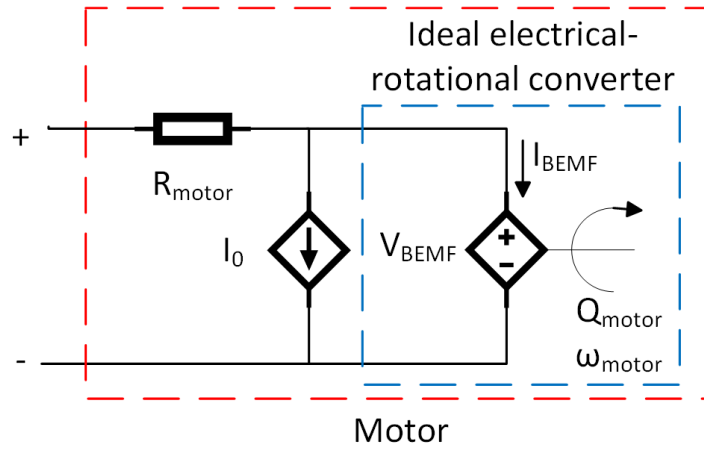


Figure 2.16: Three-constant motor electrical model. Adapted from (Green and McDonald, 2015)

From the manufacturer's datasheet, the following is given: $R_{motor}[\Omega]$, $I_0[A]$ and $K_V[rpm/V]$. K_V is converted to K by the following equation:

$$K = \frac{1}{K_V} \frac{60}{2\pi} \quad (2.17)$$

More complex BLDCM models exist, such as the four-constant model (Carri, 2018). However, this model is inconvenient in that motor manufacturer's provide the constants for the three-constant model.

2.4 Propeller

Propellers can be modelled using basic momentum theory (Silvagni *et al.*, 2018; Eva Saadé Latorre, 2011). With this approach, the propeller is idealised as an infinitesimally thin actuator disk over which a pressure difference occurs. The flow is assumed to be incompressible, inviscid, quasi-steady, one dimensional and ideal. Equations 2.18 and 2.19 are the result of these assumptions:

$$Q_P = C_Q \rho D^5 \omega^2, \quad (2.18)$$

where Q_P is the propeller torque in Nm, C_Q is the torque coefficient, ρ is the air density, D is the propeller diameter in m and ω is the angular speed in rad/s.

$$T = C_T \rho D^4 \omega^2, \quad (2.19)$$

where T is the propeller thrust and C_T is the thrust coefficient.

The following more complex models exist (Eva Saadé Latorre, 2011): *Modified momentum theory*, *Blade element theory* and a combination of momentum and blade element theory (Kuantama *et al.*, 2017).

Chapter 3

Power supply subsystem modelling

A diagram of the power supply system configuration used in this work is shown in Figure 3.1. The components of this system is shown in Figure 3.2. Fuel (hydrogen gas) is stored in the *fuel tank* at a pressure of 300 - 350 bar. The *pressure reducer* reduces the pressure of hydrogen from this high pressure to 0.5 bar (gauge). This lower pressure of hydrogen enters the anode of the *fuel cell*. When the *purge valve* is closed, hydrogen is contained in the fuel cell, between the pressure reducer and the purge valve, at a pressure of approximately 0.5 bar (gauge). Some of the hydrogen leaks, and some of it is used up in the chemical reactions. The chemical reactions cause the buildup of unwanted gases, which is removed by intermittent purging. Purging is when the purge valve is opened for a short period of time.

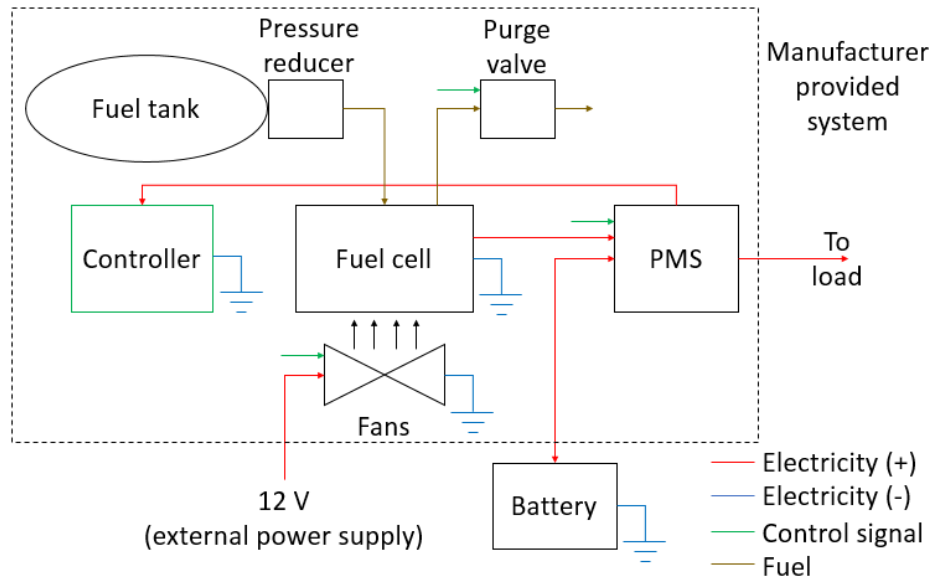


Figure 3.1: Overview of power supply system configuration. Dashed box represents a single manufacturer-provided bought-out system

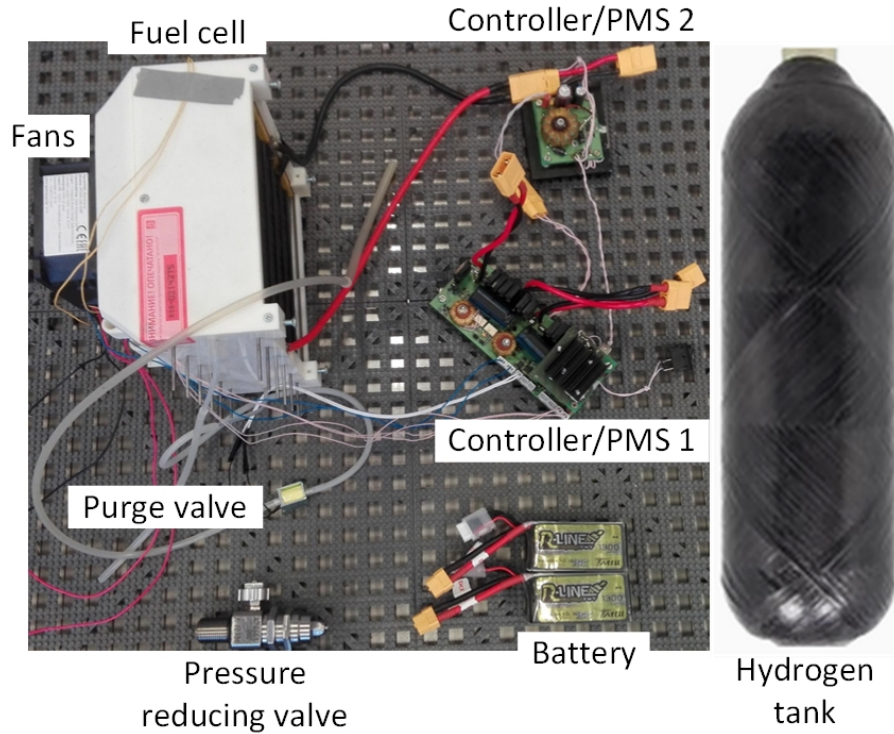


Figure 3.2: Components of the power supply system

The *fans* blow air onto the open cathode of the fuel cell. This achieves two functions. Oxygen from the air is used in the chemical reactions in the fuel cell. The moving air provides forced convection to maintain the fuel cell at a desired temperature. The fans are powered by an external 12 V power supply.

The *Power Management System (PMS)* controls the flow of power. On startup, it channels power from the *battery* to the *controller*. Thereafter it allows the controller to be powered by the fuel cell. It allows power demanded by the load to be drawn from either the fuel cell, or both the fuel cell and battery. It also allows the fuel cell to charge the battery.

The controller controls the fans, purge valve and PMS. The battery and external 12 V power supply are not included in the manufacturer-provided system. For the modelling and analysis, the following assumptions will be made:

1. The power consumed by the fans and controller, as well as the losses in the PMS, will be ignored.
2. Fuel purging will be ignored.
3. The fuel tank used will not be the one provided by the manufacturer.
4. The fuel tank and battery can be altered. Everything else remains fixed.

The components that are modelled in this section are the fuel cell, tank, PMS and battery.

3.1 Overview of data used

An overview of the data used in this chapter is shown in Figure 3.3. The battery is modelled using the author's own experimental data. The tank is not modelled, but is represented by data supplied by another manufacturer. The fuel cell and PMS are a bit more complex.

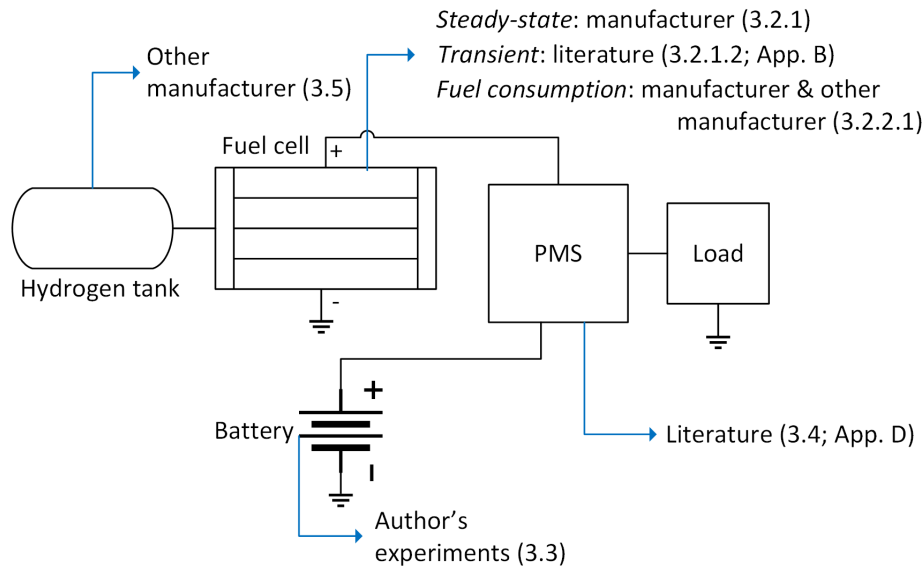


Figure 3.3: Overview of data used in Chapter 3. *Manufacturer* refers to the data supplied by the manufacturer of the procured system. *Other manufacturer* refers to data supplied by a manufacturer other than the supplier of the procured components. *Literature* refers to data found in academic literature of a similar component being tested. *Author's experiments* refers to data obtained from experiments done by the author.

The fuel cell can be divided into sub-models characterising the following phenomena separately: *steady-state response*, *transient response* and *fuel consumption*. The steady-state response is modelled using manufacturer-provided data. The fuel consumption data provided by the manufacturer is limited. Therefore, the fuel consumption model is first validated using another manufacturer's data. Thereafter, the constants are found for the procured manufacturer's fuel cell fuel consumption. For the transient response, data is used from literature. However, in order to use the data to fit the fuel cell transient model, the other components in this literature's experimental setup need to

be modelled. The modelling of these components is done in Appendix A, and the fitting of the transient fuel cell model is done Section 3.2.1.2.

For the PMS, data is used from literature. Again, the other components in the literature experimental setup need to be modelled first. This is done in Appendix C. Thereafter, the PMS itself is modelled in Section 3.4.

3.2 Fuel cell

The fuel cell performs chemical reactions to convert hydrogen into electricity. The fuel cell model will therefore be split up into a component that models the fuel consumption, and a component that models the electrical behaviour. The electrical behaviour will be split up into a steady-state model, and a transient model.

The steady-state electrical model is obtained using manufacturer-provided data. The transient electrical model is obtained using data found in literature of a different fuel cell. The fuel consumption model is obtained from manufacturer-provided data of similar fuel cells (from other manufacturers), and the manufacturer-provided data of this fuel cell.

3.2.1 Electrical model

The proposed fuel cell electrical model is shown in Figure 3.4. It contains the steady-state model, V_{SS} , and the complex impedance, Z_{FC} . The steady-state model is a voltage source as a function of the current drawn, I_{FC} . The complex impedance models the transient behaviour of the fuel cell. The impedance decreases to zero with time, resulting in the fuel cell's voltage being equal to the steady-state voltage. The model, therefore, contains a steady-state component superimposed with a transient component, which reduces to zero with time.

3.2.1.1 Steady-state electrical model

The steady-state behaviour is normally represented by a *polarization curve*, which is a voltage versus current characteristic curve. Two such curves are provided by the manufacturer, to take into account manufacturing tolerances. An average of these curves was taken, as shown in Figure 3.5a. This curve is programmed into a look-up table, and implemented in a Simscape model, as shown in Figure 3.5b.

3.2.1.2 Transient electrical model

The transient model is obtained using data from literature. The experimental setup is shown in Figure 3.6a (excluding measurement instrumentation) with details of the experimental components shown in Table 3.1. The results of one

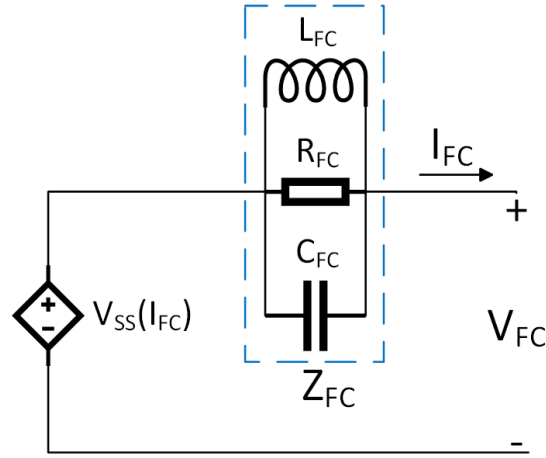
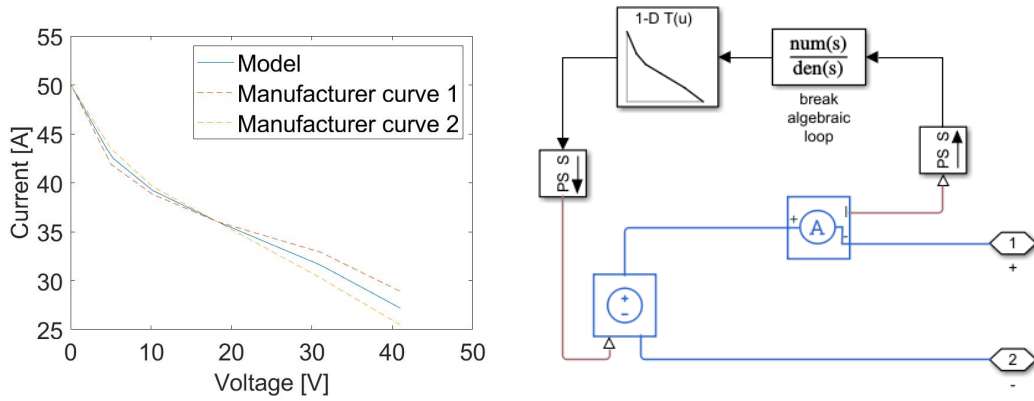


Figure 3.4: Electrical model of fuel cell



(a) Polarisation curves of fuel cell. There is uncertainty in the manufacturing process. Because of this, the manufacturer provides two possible extremes (solid lines). The model is the average of these two lines

(b) Implementation of polarisation curve as a look-up table in Simulink

Figure 3.5: Steady-state fuel cell electrical model

of the experiments is shown in Figure 3.6b. The load current is stepped from a low value to a higher value. The fuel cell current spikes to its maximum value, but then drops off, before returning to its maximum value. During the time that the fuel cell current drops, the battery current makes up for the discrepancy between the load current and fuel cell current.

The data in Figure 3.6b is to be used to obtain a transient fuel cell model. However, the rest of the experimental setup first needs to be modelled. A breakdown of the components and sub-components to be modelled is shown in Figure 3.7. The modelling of the components besides the fuel cell transient

model is described in Appendix B.

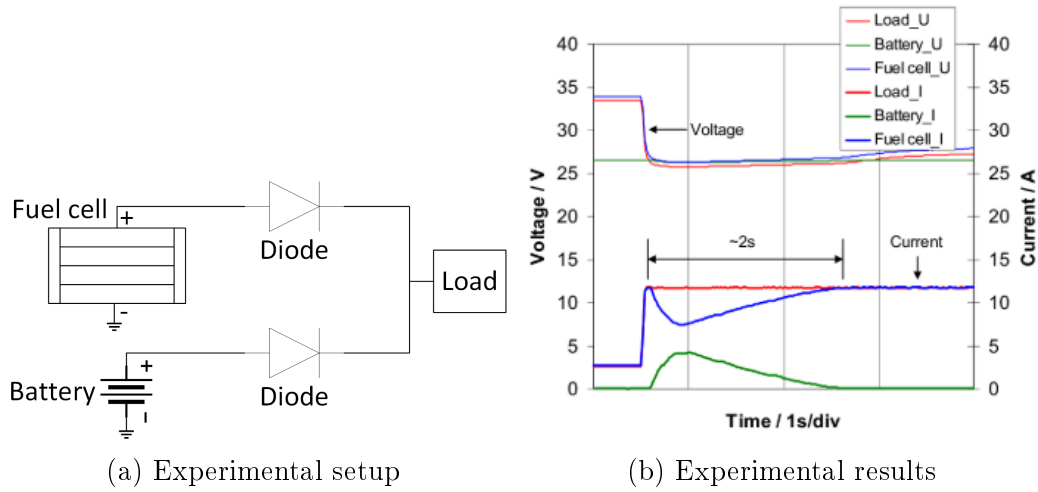


Figure 3.6: Experimental setup and results from literature, used to obtain fuel cell transient model. The load is stepped from 3 A to 12 A.

Table 3.1: Details of components used in experimental setup

Component	Product name
Fuel cell	Schunk FC-42
Battery	Lithium ion module ALM12V60
Diode	Schottky rectifier IOR 40CP060
Electric Load	Elektro-Automatik EL9080-200HP

The resulting model parameters obtained in Appendix B are shown in Figure 3.8. The remaining unknowns are the fuel cell transient model parameters, namely L_{FC} , R_{FC} and C_{FC} . The data in Figure 3.6b is composed of one input, the load current, and five outputs, the battery and fuel cell current, and the load, fuel cell and battery voltage. The model in Figure 3.8 is fit to this data using Matlab's *Parameter estimation*. The resulting parameter values and %RMSE values are listed in Table 3.2. Plots comparing the model versus experimental results are shown in Figure 3.9.

3.2.2 Fuel consumption

The approach of modelling the fuel consumption is divided into two parts. The first part is obtaining the model parameters of the theoretical model. The second part is implementing this model in Simulink. It is assumed that purging can be ignored.

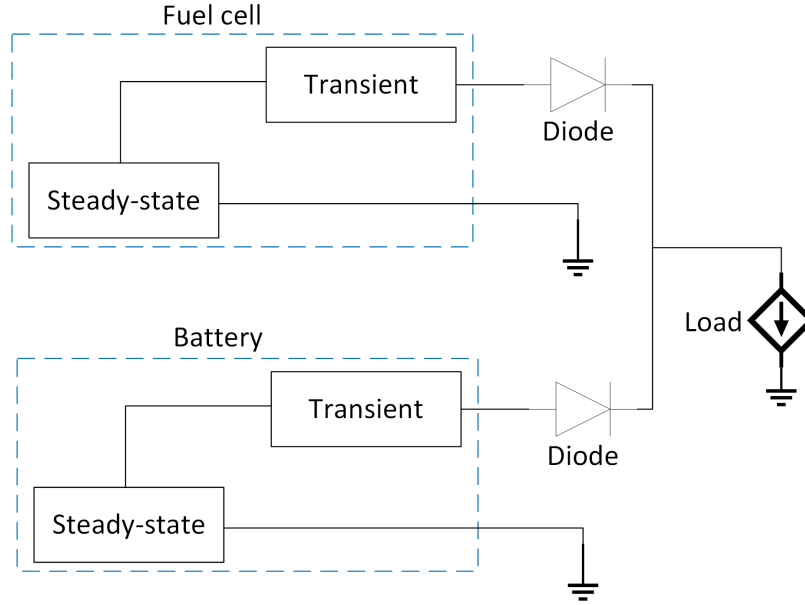


Figure 3.7: Components and sub-components to be modelled

Table 3.2: Results of obtaining the fuel cell transient electrical model

Dataset	%RMSE	Model parameter	Value
Fuel cell current	2.5144 %	C_{FC}	0.77739 F
Battery current	19.5836 %	L_{FC}	0.45235 H
Fuel cell voltage	1.5789 %	R_{FC}	0.93149 Ω
Battery voltage	0.2899 %		
Load voltage	1.9633 %		

3.2.2.1 Theoretical model

This section describes the theoretical model that characterizes fuel consumption, and describes how the model parameters are obtained.

Mass flow according to Faraday's law is:

$$\dot{m}_{H_2} = I \frac{N}{2F} \lambda M_{H_2} \quad [g/s], \quad (3.1)$$

where $F = 96485.333 \text{ C/mol}$, $M_{H_2} = 2 \cdot 1.008 \text{ g/mol}$, N is the number of cells, I is the current drawn in A and λ is the hydrogen stoichiometry. It is defined as:

$$\lambda = \frac{\dot{m}_{\text{feed}}}{\dot{m}_{\text{consumed}}} > 1, \quad (3.2)$$

where \dot{m}_{feed} is the actual mass flowrate flowing through the fuel cell, and $\dot{m}_{\text{consumed}}$ is the mass flowrate consumed in the chemical process. During test-

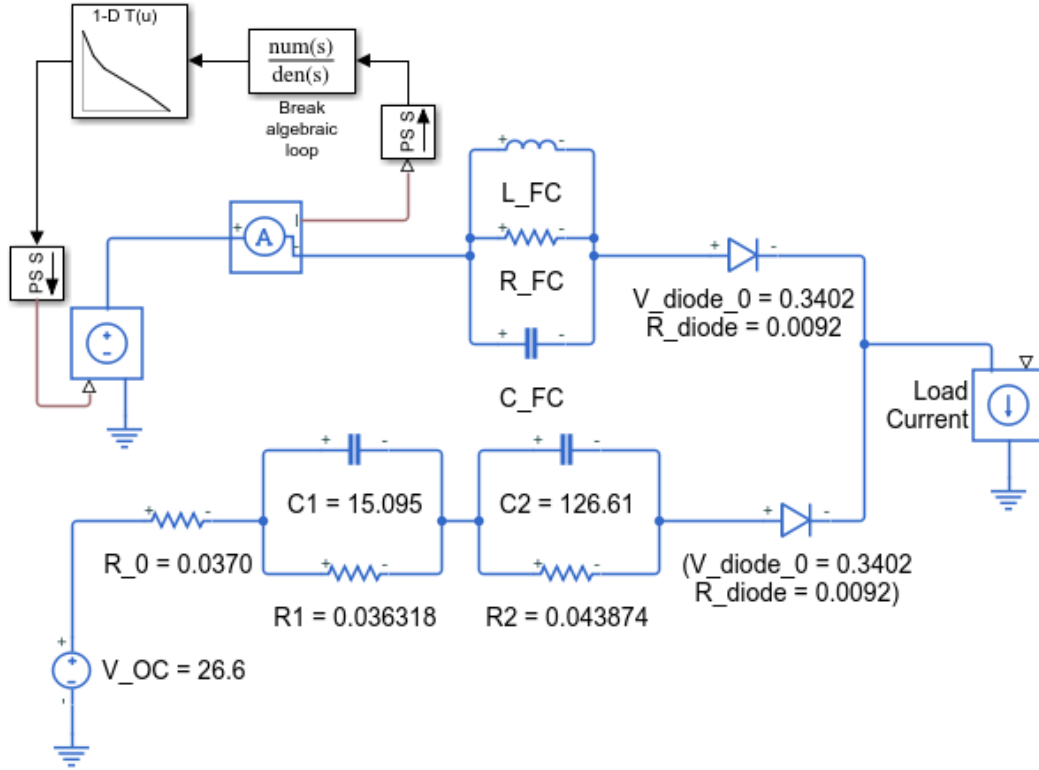


Figure 3.8: Model parameters obtained, characterising the experimental setup. The fuel cell transient parameters are still unknown, namely L_{FC} , R_{FC} and C_{FC}

ing of the fuel cell, it was found that there is significant hydrogen leakage. $\lambda > 1$ would, therefore, be the result of this leakage.

Often in datasheets, the fuel consumption is given in lpm (litres per minute). The mass flow rate obtained using Equation 3.1 can be converted to lpm in the following manner:

$$lpm = \frac{60}{\rho_{H_2}} \dot{m}_{H_2} \quad [l/min], \quad (3.3)$$

where

$$\rho_{H_2} = \frac{P_{H_2}}{R_{H_2} T_{H_2}}, \quad (3.4)$$

where $R_{H_2} = 4124.2 \text{ J/(kg} \cdot \text{K)}$, P_{H_2} is the hydrogen pressure, and T_{H_2} is the hydrogen temperature.

There is limited data supplied by the fuel cell manufacturer used in this work. These equations were, therefore, fitted to the lpm versus current of three HES fuel cells, in order to validate them. The temperature is assumed to be at 273.15 K. The pressure is assumed to be the average of the operating range.

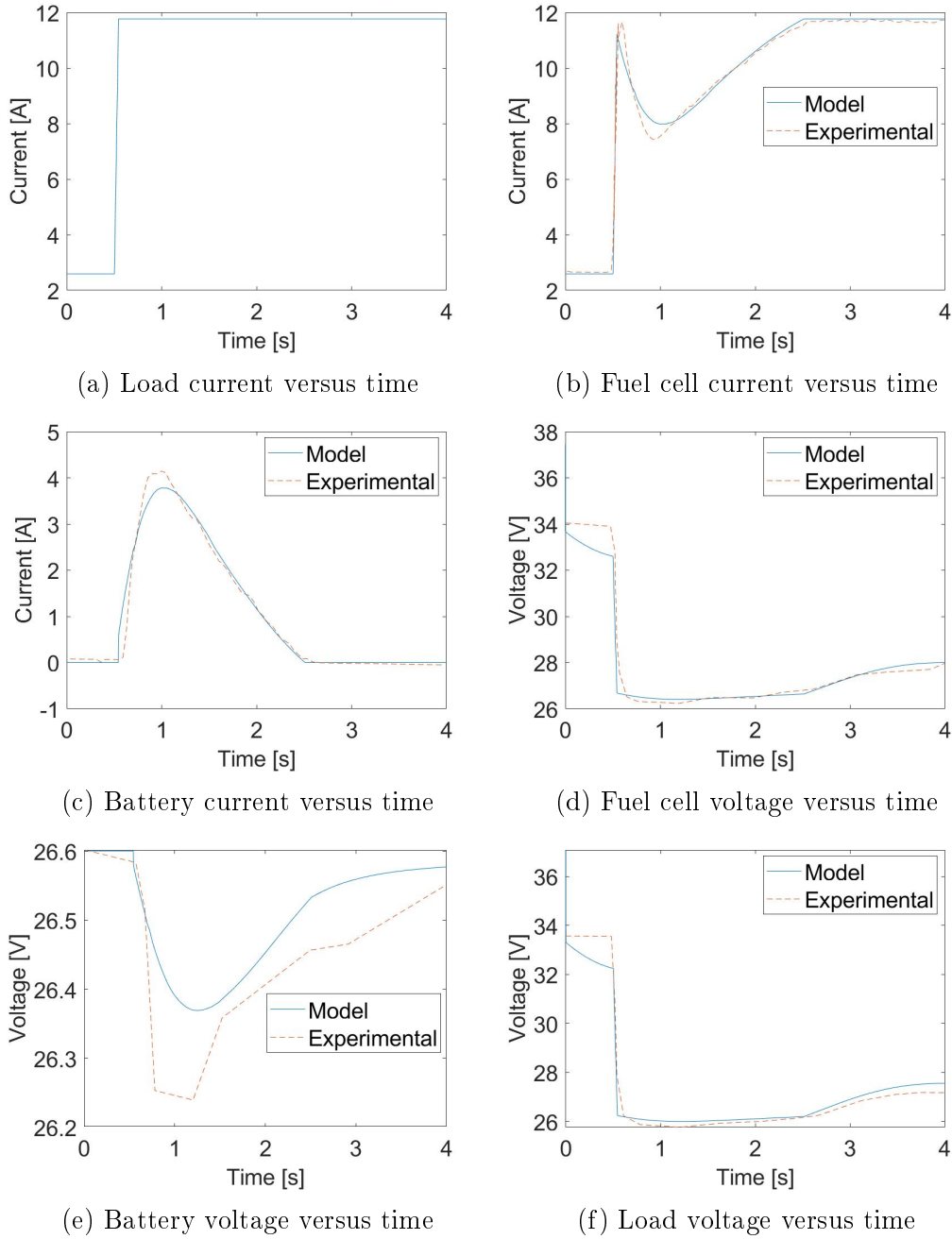
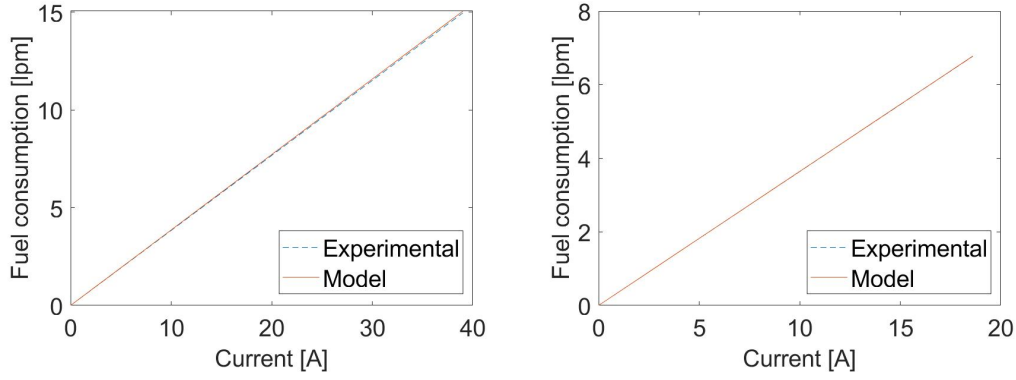


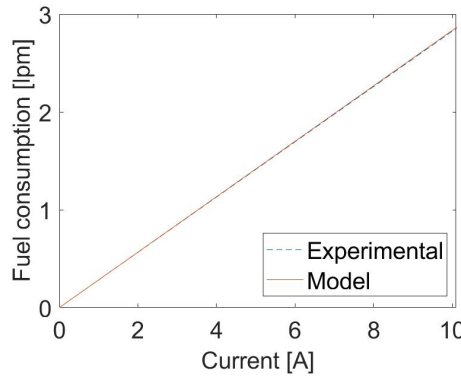
Figure 3.9: Comparison of model and experimental results - indicator of accuracy of fuel cell transient electrical model

λ is assumed to be the same for all three fuel cells. This is because they are assumed to be made of the same cells, with the same proportion of leakage. λ is the only unknown. This fit, along with the required equation constants are shown in Figure 3.10.

The same equations were fit to the data of the fuel cell used in this work.



(a) 1 000 W; N = 50; P = 1.625 bar (abs) (b) 500 W; N = 45; P = 1.55 bar (abs)



(c) 200 W; N = 35; P = 1.55 bar (abs)

Figure 3.10: Comparison of experimental versus model results of *HES Aerostaks* fuel cells. Each sub-figure is a different power rating of this product range. For each sub-figure the power rating, number of cells and operating pressure is specified. $\lambda = 1.6553$

The only fuel consumption data supplied is an lpm value at the operating power. This fit and equation data is shown in Figure 3.11a. The mass flowrate versus current is shown in Figure 3.11b.

3.2.2.2 Model implementation in Simulink

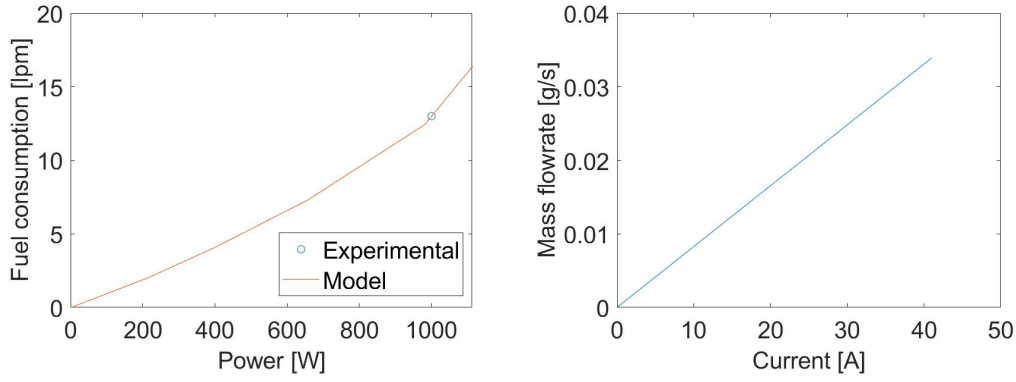
The mass flowrate for a timestep is calculated as follows:

$$\dot{m}_{H_2,i} = K_{\text{consumption}} I \quad [g/s], \quad (3.5)$$

where

$$K_{\text{consumption}} = \frac{N}{2F} \lambda M_{H_2}. \quad (3.6)$$

The mass consumed for a timestep is calculated as follows:



(a) Model is fit to one experimental data point supplied by the manufacturer (b) Resulting mass flowrate versus current relationship

Figure 3.11: Analysis to obtain mass flowrate versus current relationship. Specifications of fuel cell and operating conditions: 1 000 W; $N = 53$; $P = 1.5$ bar (abs). $\lambda = 1.4941$

$$m_{\text{consumed},i} = \dot{m}_{H_2,i}(t_i - t_{i-1}) \quad (3.7)$$

The mass of hydrogen remaining in the tank is calculated as follows:

$$m_{\text{remaining},i} = m_{\text{remaining},i-1} - m_{\text{consumed},i} \quad (3.8)$$

where $m_{\text{remaining},0}$ is the mass of hydrogen stored in a full tank, calculated in Section 3.5.

The simulation stops when the hydrogen mass reaches a critical value:

$$m_{\text{remaining},i} \leq m_{\text{threshold}} \quad (3.9)$$

For simplicity, $m_{\text{threshold}}$ is assumed to be 0 g. This assumption is made because the tank at this state has a pressure of approximately 1 bar (gauge), compared to approximately 300 bar at its full state. It is therefore assumed that there is a negligible amount of hydrogen remaining at this state of 1 bar (gauge).

Equations 3.5 to 3.9 are implemented in a simulink block, as shown in Figure 3.12.

3.3 Battery

The aim of this section is to obtain a model of a LiPo battery, and show how certain parameters can be varied. The model parameters are obtained using the author's own experimental data. First, the approach to obtain the model is described, then the experimental setup is described. Thereafter the modelling procedure is described and lastly it is shown how the parameters can be varied.

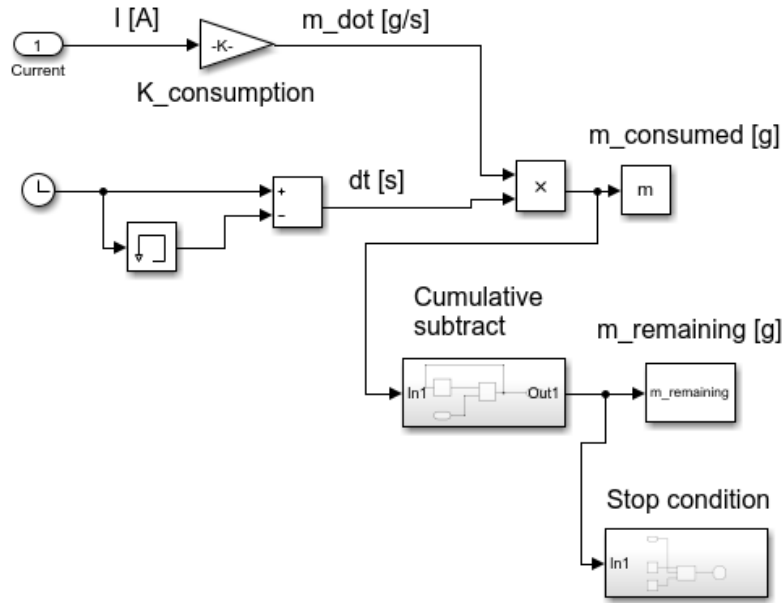


Figure 3.12: Simulink model of hydrogen fuel consumption

3.3.1 Modelling approach

The aim of this section is to obtain a theoretical battery model, where the predicted behaviour is similar to experimental behaviour. The model must be able to predict the battery's behaviour for four instances: discharge on, discharge off, charge on and charge off, as shown in Figure 2.10.

The modelling approach is divided into two phases. The first phase entails fitting a behavioural model to constant-current discharge experimental data. The behavioural model is composed of an open circuit voltage, V_{OC} , which is a function of State of Charge (SOC), and an internal resistance, R , as shown in Figure 3.13a and Equation 3.10.

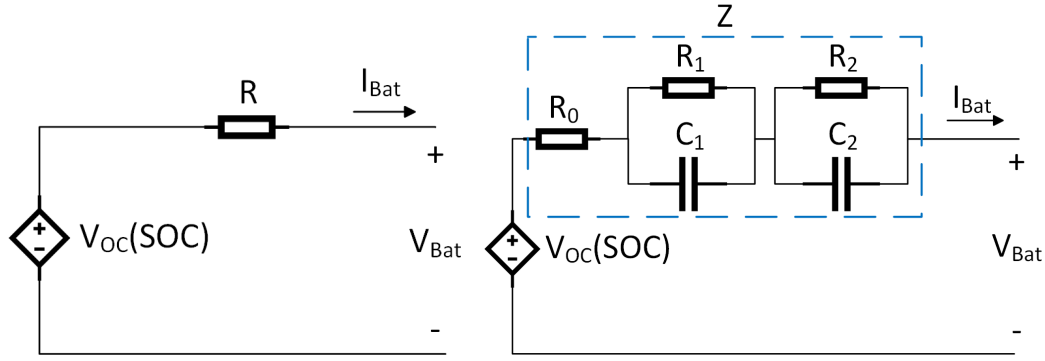
$$V_{bat} = V_{OC} - I \cdot R, \quad (3.10)$$

where V_{bat} is the voltage at the battery's terminals, and I is the current drawn.

The second phase involves replacing the internal resistance, R , with a complex internal impedance, Z , as shown in Figure 3.13b and Equation 3.11. The open circuit model, $V_{OC}(SOC)$ obtained from the first phase remains the same. Pulsed charge and discharge experimental data is used to obtain the circuit parameters of Z .

$$V_{bat} = V_{OC} - I \cdot Z \quad (3.11)$$

The following simplifying assumptions are made:



(a) Battery R_{int} model. Models (b) Battery $n - RC$ model. Models steady-state response only. state and transient response.

Figure 3.13: Battery equivalent circuit models

1. The model only needs to be accurate within the expected current range, which is around $-1.3 \text{ A} \leq 10 \text{ A}$, as found in section [system model].
2. The Coulombic efficiency is 1.
3. The model parameters are independent of State of Health (SoH), temperature, current and whether the battery is charging or discharging.
4. The maximum voltage, V_0 , can vary slightly due to the uncertainty within charging systems. V_0 is either the starting voltage of a discharge test or the ending voltage of a charging test.

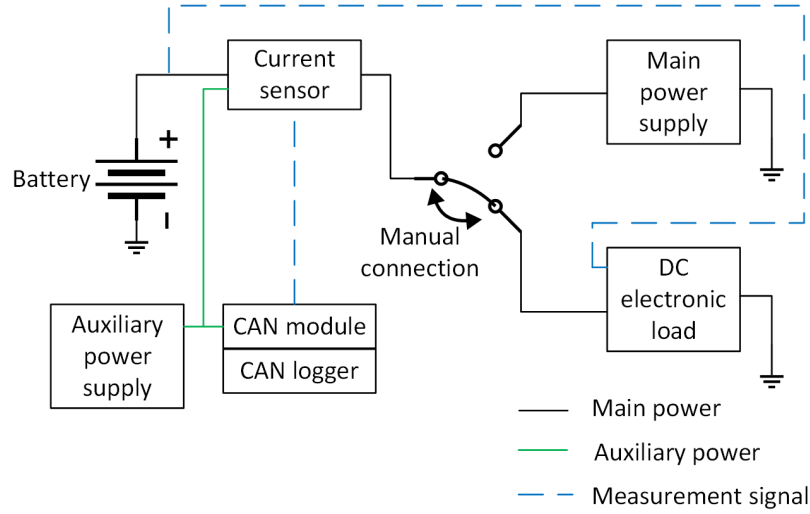
3.3.2 Experimental setup

The experimental setup is shown in Figure 3.14. It was designed to charge and discharge the battery, while measuring and logging the battery's voltage and current. The output of the *current sensor* was connected to the *main power supply*, during charging, and the *DC electronic load* during discharging. The *current sensor* outputs a voltage, which was measured and conditioned by the *CAN module* and logged by the *CAN logger*. This voltage value was converted to a current value using the following relationship:

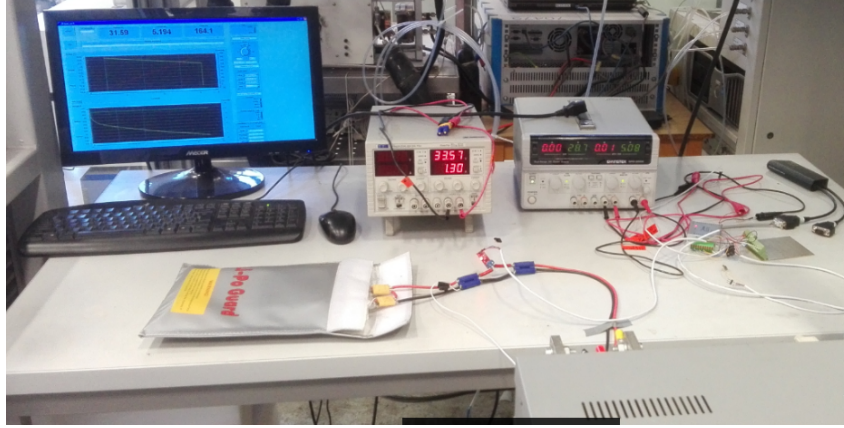
$$I = 10.2644V_{sensor} - 25.3874 \quad [A], \quad (3.12)$$

where V_{sensor} is the voltage output from the sensor. This relationship is obtained in Appendix C.

The *DC electronic load* measures and logs voltage and current. During charging, current values from the *current sensor* were used, and during discharging, current values from the *DC electronic load* were used. The *DC electronic load* has a voltage sense terminal, which was connected to the battery,



(a) Experimental setup - diagram of configuration



(b) Experimental setup - photo of actual setup

Figure 3.14: Experimental setup

to measure and log voltage during charge and discharge. The *DC electronic load*'s duty cycle was programmed on the PC, and the *main power supply* was set using its control panel. The equipment used doesn't balance the individual cells. Therefore, a commercial charger was used to balance charge or discharge the battery between some experiments. Details of the components used in the experimental setup is listed in Table 3.3.

3.3.3 Steady-state behavioural model

The main aim of this section was to obtain a behavioural model of the battery's open circuit voltage, V_{OC} , as a function of the battery's state of charge (SOC) i.e. $V_{OC} = f(SOC)$. This section describes such a behavioural model and describes how experimental data is used to obtain the model parameters.

Table 3.3: Details of components used in experimental setup

Component	Product name
Battery	2 × Tattu R-Line 4S 1300 mAh 75C (series connected to form 8S 1300 mAh 75C)
Main power supply	TTi CPX400A DUAL 60V 20A PSU
Auxiliary power supply	GW Instek SPD-3606
Current sensor	DC/AC current sensor board, 20 A, based on AC712ELC-20 IC
DC electronic load	Höckerl & Hackl GmbH ZS Electronic Load ZS5612
CAN module	PEAK System PCAN-MicroMod IPEH-002207
CAN logger	Kvaser Memorator Pro 2xHS v2
Balancing charger	Ultimate Duo 1400W/30A SKYRC (with power supply: eFuel PSU30A)

The open circuit voltage is the battery's voltage at equilibrium i.e. no current is drawn or has been drawn for a significant period of time. The state of charge is a measure of the amount of capacity remaining in the battery. As it is impractical to measure the open circuit voltage, the R_{int} equivalent circuit model (ECM) was used, described by equation 3.13 and Figure 3.13a.

$$V_{bat}(z, I_{bat}) = V_{OC}(z) - I_{bat} \cdot R_{int}, \quad (3.13)$$

where V_{bat} is the voltage at the battery's terminals, V_{OC} is the open circuit voltage, I_{bat} is the current drawn from the battery, R_{int} is the battery's internal resistance and z is the state of charge. I_{bat} is defined as positive for discharge and negative for charge.

The behavioural model used is based on Plett's *Combined model*, shown in Section 2.2.2.1. It was found that modifying the second term in this model produces a better model fit. The resulting model is:

$$V_{OC}(z) = V_0 - \frac{K_1}{z + A} - K_2z + K_3\ln(z) + K_4\ln(1 - z), \quad (3.14)$$

where V_0 is the open circuit voltage when the battery is fully charged, and K_1 , K_2 , K_3 , K_4 and A are empirical constants.

Equations 3.13 and 3.14 can then be combined to obtain a model, which predicts the battery voltage as a function of SOC and current:

$$\begin{aligned} V_{bat}(z, I_{bat}) &= V_{OC}(z) - I_{bat} \cdot R_{int} \\ &= V_0 - \frac{K_1}{z + A} - K_2z + K_3\ln(z) + K_4\ln(1 - z) - I_{bat} \cdot R_{int} \end{aligned} \quad (3.15)$$

Calculation of SOC is done using Equation 2.4.

Experimental data is required to obtain the model parameters of Equations 3.15 and 2.4. The data required is constant-current discharge data. It was obtained in the following manner: The fully charged battery was discharged at a constant current until it reached its lower limit of 28 V. It was then fully charged using the *commercial charger*. This was repeated with different constant-current discharge values.

Capacity discharged is calculated in the following manner:

$$C_{discharged_{k+1}} = C_{discharged_i} - I_{bat_k} \Delta t, \quad (3.16)$$

where $C_{discharged}$ is the capacity discharged in Ampere-hours (Ah) and Δt is the timestep.

The experimental data was then used to obtain the model parameters in the following way:

The Coulombic efficiency, η_i , is 1 because it was all discharge data. The fully-charged open circuit voltage, V_0 , was calculated by taking the average of the starting voltages in the discharge tests. All other constants were obtained by fitting Equations 3.15 and 2.4 to the experimental discharge curves. The results of the model fit is shown in Table 3.4 and Figure 3.15.

Table 3.4: Phase 1: Model parameters and %RMSE values

Model constant	Value	Experiment	%RMSE
V0	33.4712	1.3 A discharge	0.6057 %
R	0.0953	5 A discharge	0.5506 %
Cn	1.3845	10 A discharge	0.4448 %
A	0.1457	15 A discharge	0.5097 %
K1	-7.7504	20 A discharge	0.6759 %
K2	10.2717		
K3	15.1016		
K4	-0.8932		

3.3.4 Transient equivalent circuit model

The next phase of modelling the battery was to obtain the parameters of the equivalent circuit model (ECM). The model is shown in Figure 3.13b. The open circuit voltage, $V_{OC}(SOC)$ model was obtained in section 3.3.3. It is Equation 3.14, with the parameter values listed in Table 3.4. The ECM must be able to predict the transient voltage change for the four instances shown in Figure 2.10.

There are different methods for obtaining the ECM model parameters. Often the parameters are obtained for different SOC values, and sometimes for

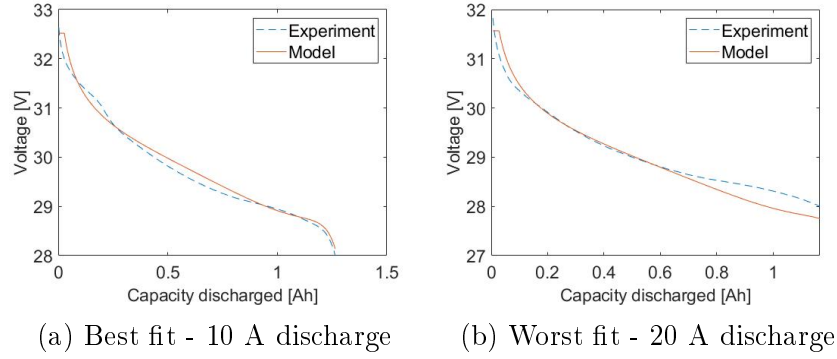


Figure 3.15: Phase 1: constant-current discharge curves

different current values and different current directions. For this work, in order to simplify the model, the same model parameters will be used independent of the SOC, current and current direction. Therefore, the data used to fit the model must contain the four instances (discharge on, discharge off, charge on and charge off) for different SOC and current values.

The current duty cycle to achieve this is shown in Figure 3.16a. It contained pulsed discharges of 2 C, 4 C, 6 C and 8 C, followed by pulsed charges of 1 C. This was followed by a constant-current discharge of 4C, which in turn was followed by the pulsed discharge and charge being repeated. The pulsed discharge and constant-current discharge was achieved by programming the *DC electronic load*. The pulsed charging was achieved by manually switching the output of the *main power supply* on and off. To switch from discharge to charge, the output of the *current sensor* was manually disconnected from the *DC electronic load* and connected to the *main power supply*. Matlab's *Parameter estimation* was used to fit the model to the experimental data. The comparison between the model voltage and experimental voltage is shown in Figure 3.16b. The model parameters obtained is listed in Table 3.5.

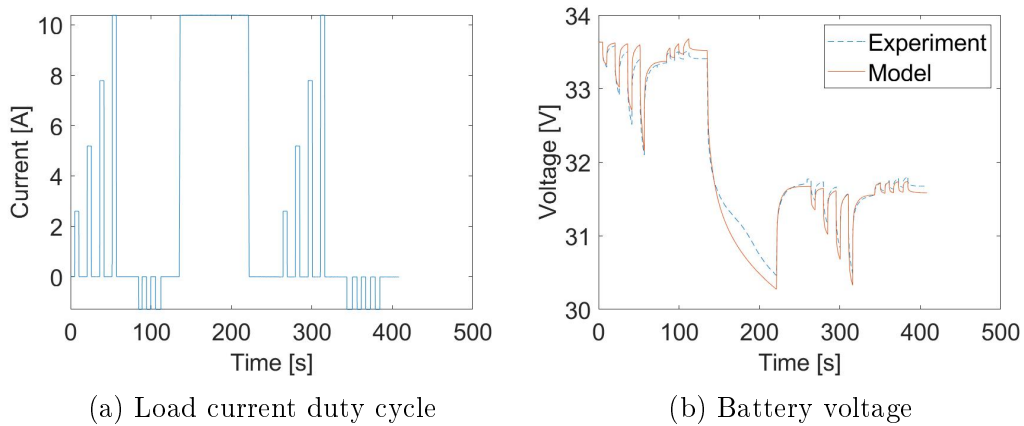


Figure 3.16: Phase 2: Hybrid pulse power characterisation test

Table 3.5: Phase 2: Model parameters

Behavioural model		Equivalent circuit model	
Model constant	Value	Model constant	Value
Cn	1.3845	R0	0.054726
A	0.1457	R1	0.036318
K1	-7.7504	C1	15.095
K2	10.2717	R2	0.043874
K3	15.1016	C2	126.61
K4	-0.8932		

In order to check the model accuracy for different duty cycles, the model was also tested with constant-current discharge data, and constant-current-constant-voltage charge data, for different currents. The constant-current discharge data was obtained in Section 3.3.3. A comparison between this data and the model-predicted voltage is shown in Figure 3.17.

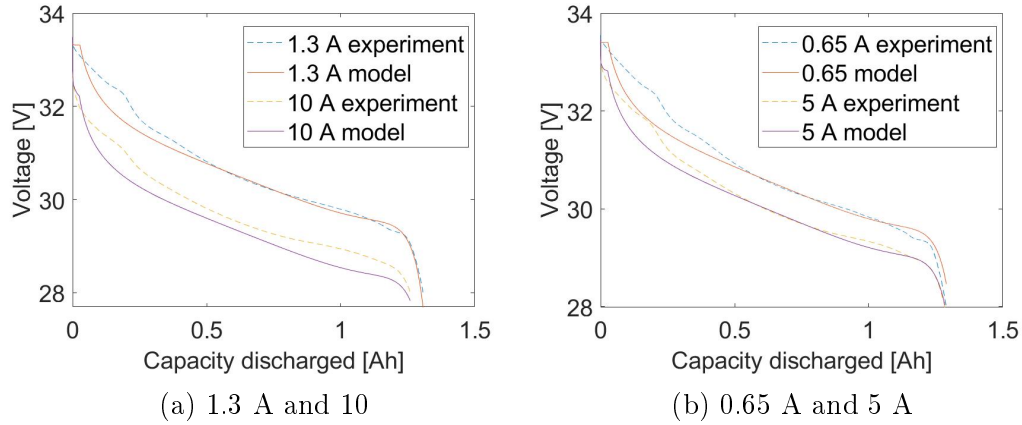


Figure 3.17: Phase 2: constant-current discharge tests

Constant-current-constant-voltage charge data was obtained in the following manner: The *main power supply* was set to the desired current value, with the voltage set to the maximum battery voltage, V_0 , of 33.6 V. This caused the battery to charge first in constant-current mode (the horizontal lines in Figures 3.18a and 3.18c), and then in constant-voltage mode (the decreasing magnitude of current values in Figures 3.18b and 3.18d). A comparison between this voltage data and the model-predicted voltage is shown in Figures 3.18b and 3.18d. The %RMSE values of the model versus experiment comparisons is shown in Table 3.6.

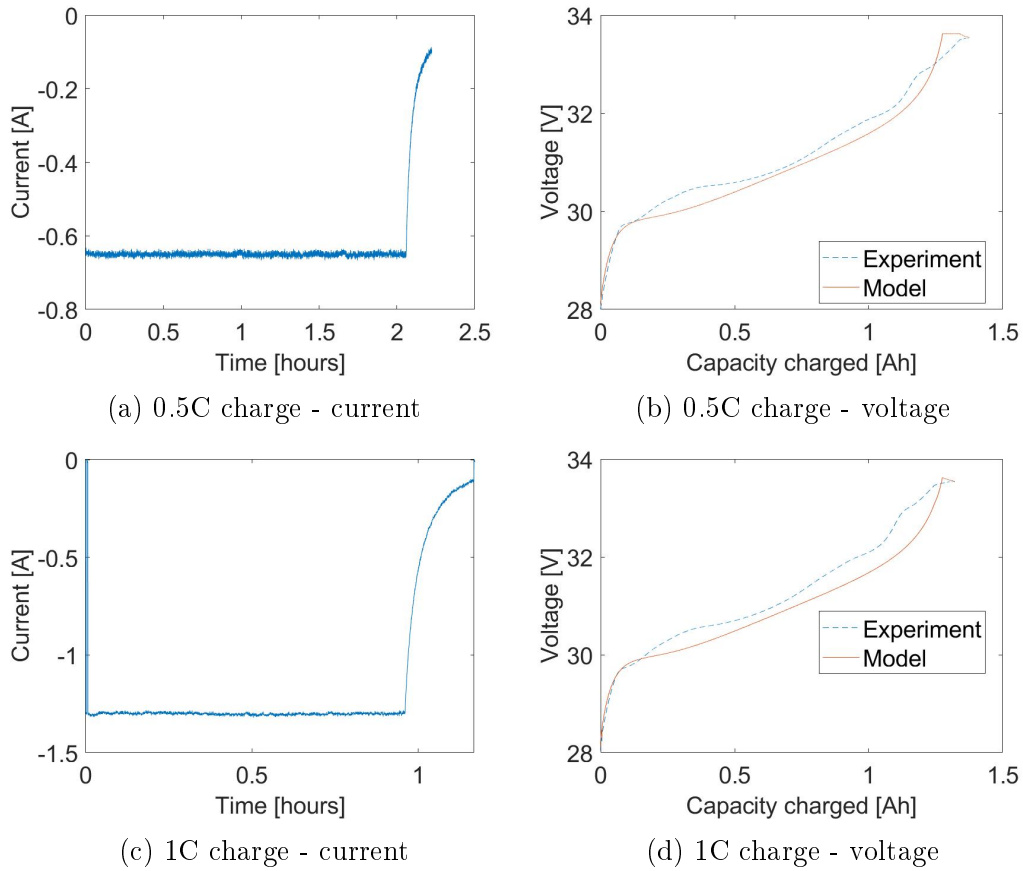


Figure 3.18: Phase 2: constant-current-constant-voltage charge tests

Table 3.6: Phase 2: %RMSE and V_0 values

Experiment type	V_0	Figure reference	Experiment detail	%RMSE
Pulsed charge and discharge	33.6331 V	Figure 3.16	Discharge: 2 C, 4 C, 6 C, 8 C; Charge: 1 C	0.4464 %
Constant-current, constant-voltage charge	33.5348 V	Figure 3.18	0.5 C	0.7290 %
			1 C	1.0311 %
Constant-current discharge	33.49 V	Figure 3.17	0.65 A	0.8210 %
			1.3 A	0.6632 %
			5 A	0.6389 %
			10 A	1.0988 %

3.3.5 Varying parameters

A model was obtained for the Tattu R-Line 4S 1300 mAh 75C (series connected to form an 8S battery). This section describes how the rated capacity can be varied, and how this changes the battery's electrical model and mass.

3.3.5.1 Effect on electrical model

The nominal capacity is a constant factor greater than the rated capacity (Mathworks, 2008). It logically follows from this that the nominal capacity changes as a function of the rated capacity as follows:

$$C_n = C_{n,0} \frac{C_{rated}}{C_{rated,0}}, \quad (3.17)$$

where $C_{n,0}$ and $C_{rated,0}$ refers to the nominal and rated capacity respectively, of the current battery. C_n and C_{rated} refers to the nominal and rated capacity respectively, of the modified battery.

3.3.5.2 Effect on mass

There is a linear relationship between battery mass and number of cells, with a near-zero y-intercept (Bershadsky *et al.*, 2016). There is a linear relationship between battery mass and rated capacity, with a zero y-intercept (Mauro Gatti, 2015). It therefore follows logically that the battery mass can be scaled linearly as a function of rated capacity and number of cells as follows:

$$m_{bat} = m_{bat,0} \frac{C_{rated}}{C_{rated,0}} \frac{N_{cells}}{N_{cells,0}}, \quad (3.18)$$

where $m_{bat,0}$ is the current battery mass and m_{bat} is the modified battery mass.

3.3.6 Discussion

3.3.6.1 Behavioural model

This discussion is based on the results in Section 3.3.3. As can be seen in Figure 3.15, the fit is quite good. This is also shown in Table 3.4, with all the %RMSE values below 0.7 %. The largest discrepancy can be seen with 20 A discharge. This is because the battery heated up, and the model parameters should vary as a function of temperature (Mathworks, 2008), which it doesn't. This shouldn't be a problem, as the battery current is mainly below 10 A in the system model (Figure 5.3c).

3.3.6.2 Equivalent circuit model

This discussion is based on the results in Section 3.3.4. The model obtained has a relatively good fit for a range of different data. The %RMSE values are all below 1.1 % (Table 3.5). The data includes constant-current discharge for a range of currents (Figure 3.17), up to the maximum 10 A expected (Figure 5.3c). It also includes constant-current-constant-voltage charging up to the 1C max charge rate (Figure 3.18). It also includes HPPC data, which contains all four modes (charge on and off, and discharge on and off), with different currents (Figure 3.16).

However, the model is a compromise for the following reasons: Hysteresis is not modelled. Hysteresis causes the voltage to relax after discharge to a higher value than the model predicts (Plett, 2004). Also, the model would be more accurate if it had different resistances for charge and discharge (Plett, 2004).

Because of these things not being modelled, the total resistance of the ECM ($R_0 + R_1 + R_2$) is 41.6 % higher than the internal resistance, R , of the behavioural model. This causes the %RMSE to be higher for the constant-current discharge fit of the ECM model, compared to the behavioural model. Also, there are significant discrepancies with the fits of the HPPC (Figure 3.16) and charge (Figure 3.18), as a result of the simplified model used.

3.4 Power management system

The power management system (PMS) manages the power flow between the fuel cell, battery and load. The configuration of a passive power management system is shown in Figure 2.8a and described in Section 2.1.8.1. There are three modes of operation of such a system. Mode 1 is when power is drawn only from the fuel cell (Figure 2.9a). Mode 2 is when power is drawn from the fuel cell and battery (Figure 2.9b). Mode 3 is when power is drawn from the fuel cell, and additional power is drawn from the fuel cell to charge the battery (Figure 2.9c).

3.4.1 Approach

The modelling approach is divided into two parts. The first part involves fitting a model to experimental data found in literature. A model will be obtained to characterise the three phases in Figure 2.9. The data used for mode 3 is limited in that the fuel cell voltage is kept constant throughout the experiments. The second part involves demonstrating that the model works for varying the load current, which causes the fuel cell voltage to vary.

3.4.2 Data used

Data from literature is used to characterise and model a PMS. Gong and Verstraetey (2014) did various tests on a Commercial-Off-The-Shelf (COTS) system comprising of a fuel cell system, battery and PMS. This system is similar to the one acquired for this work. It was therefore decided to use the results of Gong's experiments to develop a model of a PMS.

Gong makes use of two experimental setups. The first one is to characterise the power flow between the fuel cell and battery, and the load (shown in Figure 3.19). The aim is to characterise the steady-state behaviour of this power flow. The load is kept constant at increasing power values. In order to obtain "quasi-steady-state" behaviour, the power value is kept constant for sufficiently long to obtain close to steady-state behaviour of the fuel cell, while short enough to not discharge the battery too much. The lengths of time power values are kept constant is listed in Table 3.7. The experimental results are shown in Figure 3.21.

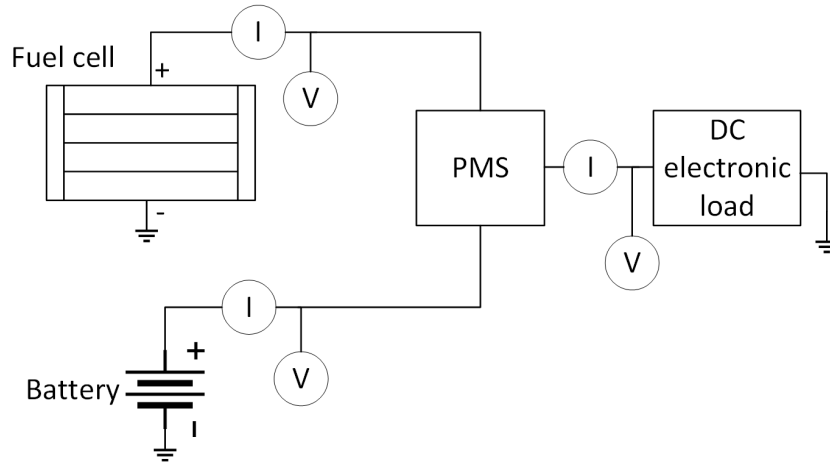


Figure 3.19: Experimental setup 1. Adapted from (Gong and Verstraetey, 2014)

The second setup is to characterise the power flow between the fuel cell and battery during charging. The setup in Figure 3.19 is modified by removing the load and by replacing the fuel cell with a DC power supply. This setup is shown in Figure 3.20. The battery is discharged to a voltage value, the power supply is set to a voltage value, and the battery is charged using the PMS until its voltage doesn't change. This is repeated with different battery starting voltages (21 V and 23 V), with the the same power supply voltage (30 V) (results shown in Figures 3.24 and 3.25). It was repeated with different power supply voltages (23 V, 25 V and 30 V), with the same battery starting voltage (22 V) (results shown in Figure 3.26).

Details of the components used in the experimental setups are listed in Table 3.8.

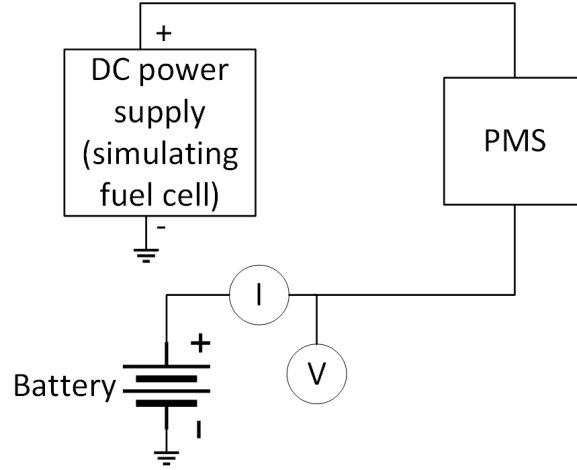


Figure 3.20: Experimental setup 2. Adapted from (Gong and Verstraetey, 2014)

Table 3.7: Time duration power values are kept constant

Power value [W]	Time duration [s]
< 200	100
200 - 400	60
500 - 600	25

3.4.3 Modelling

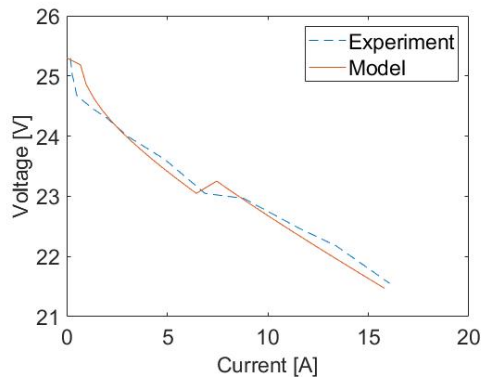
The aim of this section is to model the PMS based on Gong's results. However, a model of the fuel cell system and battery used by Gong is first required. Obtaining these models is described in Appendix D.

Now that there are models for the fuel cell and battery, a model for the PMS can be developed. First a model is developed for modes 1 and 2 (Figures 2.9a and 2.9b). The data used is Gong's first experiment (experimental setup shown in Figure 3.19). The model proposed is the same as in Figure 2.8a, where there is a diode in front of the fuel cell, and in front of the battery, but ignoring the charger. It is assumed that the diodes are ideal, meaning there is no voltage drop or internal resistance. The model and experimental results are compared in Figure 3.21.

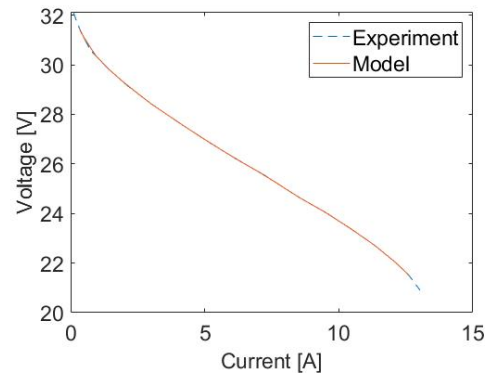
Next mode 3 (Figure 2.9c) is modelled. However, only the power flow between the fuel cell and battery is of interest here. A more detailed diagram of this section of the PMS (which is essentially a battery charger) is shown

Table 3.8: Details of components used in experimental setup

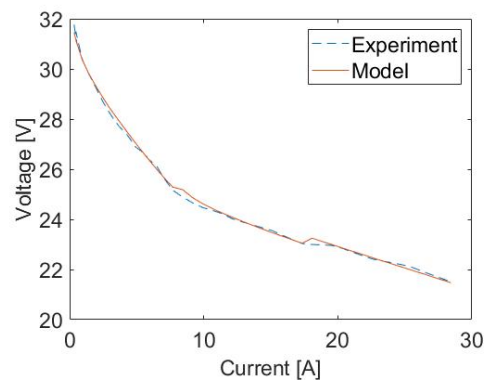
Component	Detail
Hybrid system	AeroPak (by Horizon Energy Systems)
Fuel cell	AEROSTAK AST01-01 (200W) PEM fuel cell
Battery	2 \times ThunderPower 3S 1350mAh 25C G6 Pro Lite connected in series (to form a 6S 1350mAh 25C battery)
Charging component of PMS	LTC3824 voltage step down controller driving a 7463 P-Channel MOSFET
DC electronic load	BK Precision IT8514F-1200
DC power supply	ET System LAB/SMS 435
Voltage and current measurement (low power)	ISOTECH IDM73 multimeter with serial connection
Current measurement (high power)	Eagle Tree Hall sensors



(a) Battery



(b) Fuel cell



(c) Total

Figure 3.21: Data of modes 1 and 2

in Figure 3.22. The control system monitors the current charging the battery and voltage applied at its terminals. It controls the switching duty cycle of the MOSFET. This controls the current and voltage level at the battery side of the MOSFET. Based on Gong's results, there are 3 phases of the charging process (shown in Figure 3.23). In the first 2 phases the current is controlled. In the first phase, current is ramped up to a certain value. In the second phase, the current is kept constant at this value. In the third phase, voltage is controlled. The voltage level is kept constant at the maximum desired voltage of the battery. The battery voltage increases to this value, as the current decreases to close to zero. This is similar to the constant-current constant-voltage algorithm used in most lithium battery chargers. The control system controls the current and voltage. However, to simplify the model, only the behaviour of the current is modelled.

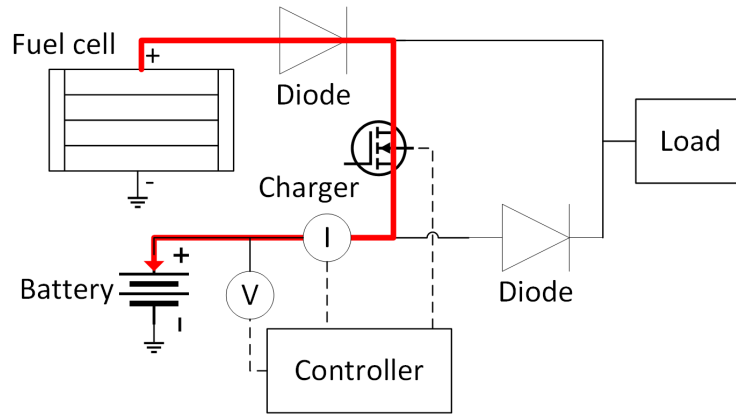


Figure 3.22: Operation of charging system

The first phase is modelled according to the following equation:

$$\text{Phase 1: } I_{\text{charge}}(V_{\text{bat}}, t) = I_{CC} + \frac{I_{CC} - I_{\text{start}}}{t_{CC}}[t - t_{CC}] \quad (3.19)$$

$$\text{if } \begin{cases} t < t_{CC} \\ V_{\text{bat}} < V_{CV}(V_{FC}) \end{cases} ,$$

where I_{charge} is the charging current, V_{bat} is the battery voltage, t is the time since start of charging, I_{CC} is the constant-current charge value, I_{start} is the charge current at $t = 0$ and t_{CC} is the time after start of charging that phase 1 ends.

The second phase is modelled according to the following equation:

$$\text{Phase 2: } I_{\text{charge}}(V_{\text{bat}}, t) = I_{CC} \quad \text{if } \begin{cases} t \geq t_{CC} \\ V_{\text{bat}} < V_{CV} \end{cases} , \quad (3.20)$$

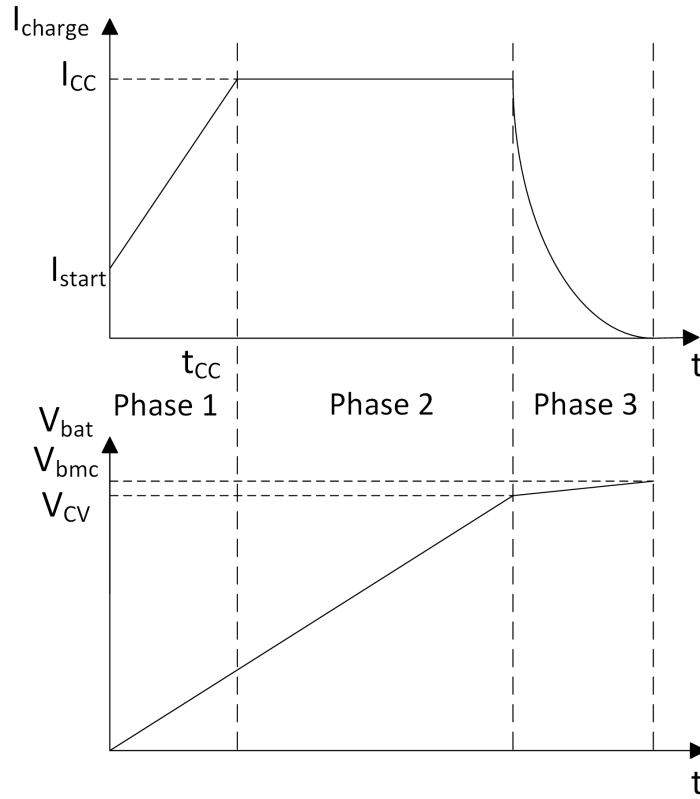


Figure 3.23: Different phases of battery charging

where V_{CV} is the battery voltage at which phase 3, the constant-voltage phase starts.

The third phase is modelled according to the following equation:

$$\begin{aligned} \text{Phase 3: } I_{charge}(V_{bat}, t) &= I_{CC} \left[1 - \frac{1}{\Delta V_{CV}} (V_{bat} - V_{CV}) \right] \\ &\text{if } V_{CV} \leq V_{bat} \leq V_{bmc}, \end{aligned} \quad (3.21)$$

where V_{bmc} is the maximum voltage to which the battery is charged and $\Delta V_{CV} = V_{bmc} - V_{CV}$.

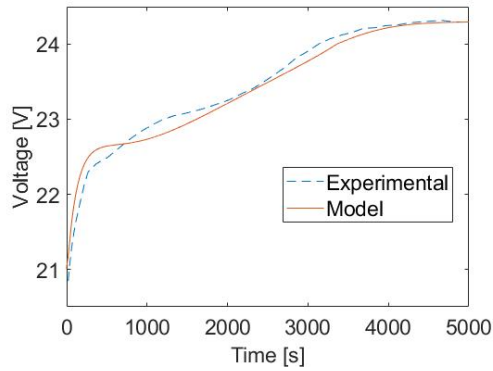
The constants in Equations 3.19 - 3.21 were selected based on observation of Gong's results, and are listed in Table 3.9. Comparison of this model with Gong's data is shown in Figures 3.24 and 3.25.

Next the charger model is modified to take into different fuel cell voltages. The constant current value is higher when the fuel cell voltage is closer to the battery voltage (i.e. lower). The following equation takes this into account:

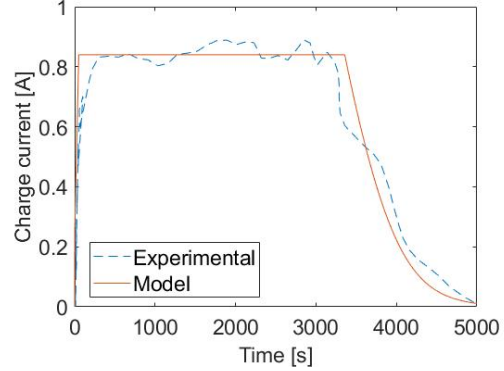
$$I_{CC}(V_{FC}) = -0.012(V_{FC} - V_{bmc}) + 0.9084 \quad (3.22)$$

Table 3.9: Constants for Equation 3.19 to 3.21

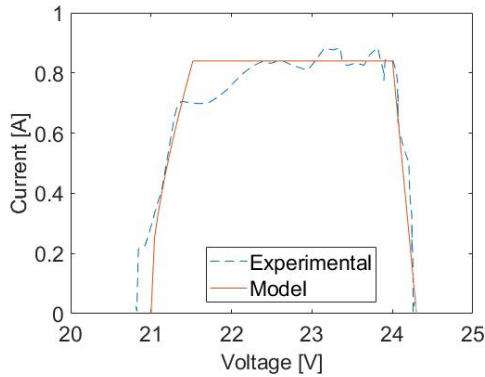
Constants	Equation / value	Unit
I_{CC}	0.84	A
I_{start}	0.25	A
t_{CC}	50	s
V_{bmc}	4.3	V
ΔV_{CV}	0.3	V
V_{CV}	$V_{bmc} - \Delta V_{CV}$	V



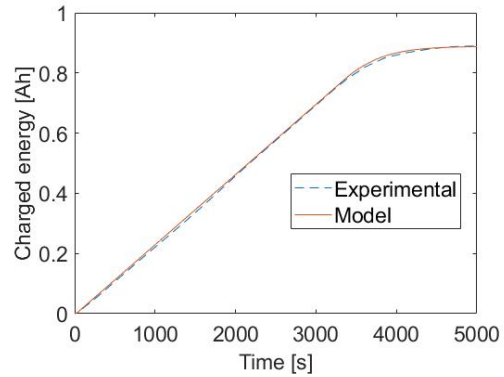
(a) Battery voltage vs time; %RMSE = 0.5308 %



(b) Charge current versus time



(c) Charge current versus voltage



(d) Charge energy vs time; %RMSE = 0.7781 %

Figure 3.24: Charging battery from starting voltage of 21 V. Data obtained using experimental setup 1

If the fuel cell voltage is less than the maximum battery charge voltage, V_{bmc} is altered in the following manner:

$$V_{bmc}(V_{FC}) = \text{minimum}(V_{bmc,K}, V_{FC}), \quad (3.23)$$

where V_{bmc} is the actual maximum voltage that the battery can be charged

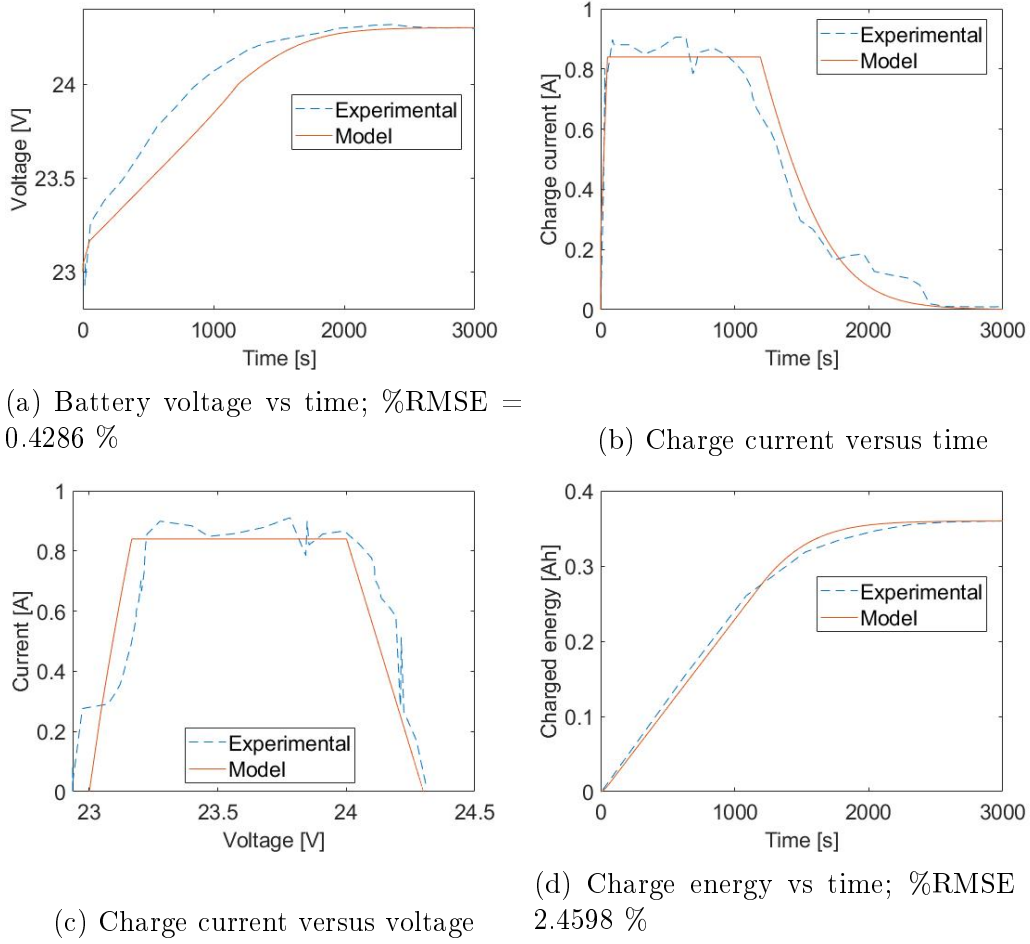


Figure 3.25: Charging battery from starting voltage of 23 V. Data obtained using experimental setup 1

to, $V_{bmc,K}$ is a preprogrammed constant in the charger that limits the maximum battery voltage and V_{FC} is the fuel cell voltage.

The modified model is run and compared to Gongs results (Shown in Figure 3.26).

The charging model was developed for a specific battery, which had a specific number of cells and a specific capacity. It is suggested that this model can be modified to take into account an arbitrary number of cells and capacity. The generalized model is summarized in Equation 3.24, with the constants listed in Table 3.10.

$$\text{Maximum battery voltage: } V_{bmc}(V_{FC}) = \min(V_{bmc,K}, V_{FC}) \quad (3.24a)$$

$$\text{Start of constant-voltage: } V_{CV}(V_{FC}) = V_{bmc}(V_{FC}) - \Delta V_{CV} \quad (3.24b)$$

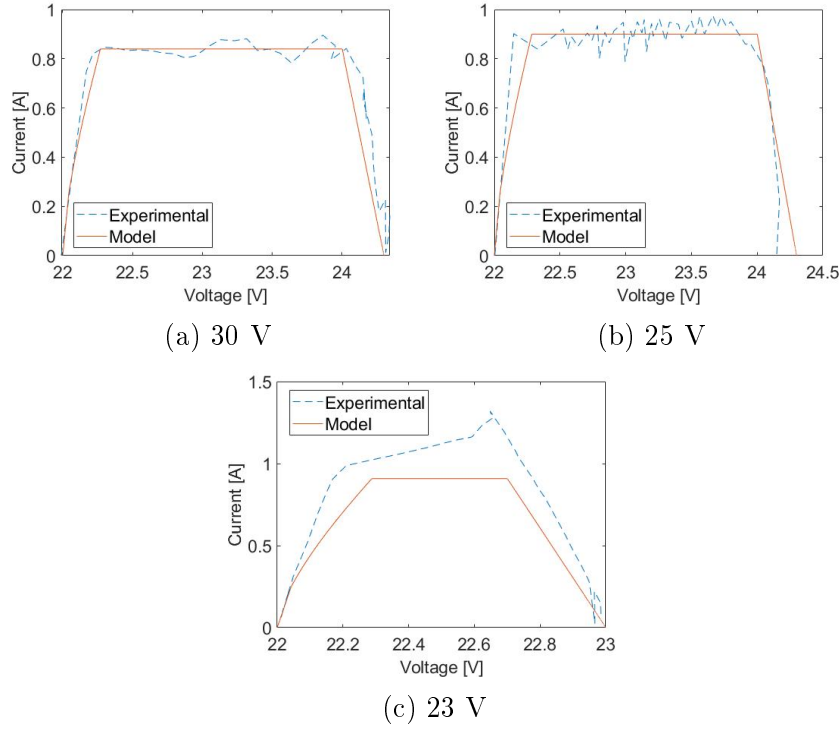


Figure 3.26: Voltage vs current for different fuel cell voltages. Data obtained using experimental setup 2.

Constant current:

$$I_{CC}(V_{FC}) = [-0.012[V_{FC} - V_{bmc}(V_{FC})] + 0.9084] \frac{C_{rated}}{1.35} \quad (3.24c)$$

$$\text{Phase 1: } I(V_{FC}, V_{bat}, t) = I_{CC}(V_{FC}) + \frac{I_{CC}(V_{FC}) - I_{start}}{t_{CC}} [t - t_{CC}] \quad (3.24d)$$

if $\begin{cases} t < t_{CC} \\ V_{bat} < V_{CV}(V_{FC}) \end{cases}$

$$\text{Phase 2: } I(V_{FC}, V_{bat}, t) = I_{CC}(V_{FC}) \quad \text{if } \begin{cases} t \geq t_{CC} \\ V_{bat} < V_{CV}(V_{FC}) \end{cases} \quad (3.24e)$$

$$\text{Phase 3: } I(V_{FC}, V_{bat}, t) = I_{CC}(V_{FC}) \left[1 - \frac{1}{\Delta V_{CV}} [V_{bat} - V_{CV}(V_{FC})] \right] \quad (3.24f)$$

if $V_{CV}(V_{FC}) \leq V_{bat} \leq V_{bmc}(V_{FC})$

3.4.4 Model implementation in Simulink

In section 3.4.3 it was found that the charger model matches experimental data. However, there are limitations to the experimental data used: the power supply (representing a fuel cell) voltage remained constant, and the battery

Table 3.10: Constants for Equation 3.24

Constants	Equation / value	Unit
I_{start}	0.25	A
t_{CC}	50	s
$V_{bmc,K}$	$4.3(N_{cells}/6)$	V
ΔV_{CV}	$0.3(N_{cells}/6)$	V

remained in the charge state, throughout the test. In reality, the load current will vary, causing the fuel cell voltage to change, and the battery to switch between charge and discharge states. It must therefore be shown that the charger model works with a varying load current, and that all the sub-equations in Equation 3.24 are implemented. It must also be shown that the PMS model obtained works with the fuel cell and battery model obtained in Sections 3.2 and 3.3 respectively.

Equation 3.24 can be considered to be complex because of the different modes of operation (phases), dependent on the time since start of charging and the battery voltage. However, Equations 3.24d (Phase 1) and 3.24f (Phase 3) are set up that their value will be greater than 3.24e (Phase 2) if the time or battery voltage is not within the specified bounds. Therefore, Equation 3.24 can be simplified in the following manner:

$$\text{Maximum battery voltage: } V_{bmc}(V_{FC}) = \min(V_{bmc,K}, V_{FC}) \quad (3.25a)$$

$$\text{Start of constant-voltage: } V_{CV}(V_{FC}) = V_{bmc}(V_{FC}) - \Delta V_{CV} \quad (3.25b)$$

Constant current:

$$I_{CC}(V_{FC}) = [-0.012[V_{FC} - V_{bmc}(V_{FC})] + 0.9084] \frac{C_{rated}}{1.35} \quad (3.25c)$$

$$\text{Phase 1: } I_1(V_{FC}, V_{bat}, t) = I_{CC}(V_{FC}) + \frac{I_{CC}(V_{FC}) - I_{start}}{t_{CC}}[t - t_{CC}] \quad (3.25d)$$

$$\text{Phase 2: } I_2(V_{FC}, V_{bat}, t) = I_{CC}(V_{FC}) \quad (3.25e)$$

$$\text{Phase 3: } I_3(V_{FC}, V_{bat}, t) = I_{CC}(V_{FC}) \left[1 - \frac{1}{\Delta V_{CV}}[V_{bat} - V_{CV}(V_{FC})] \right] \quad (3.25f)$$

$$\text{Charge current: } I_{charge} = \min(I_1, I_2, I_3) \quad (3.25g)$$

Figure 3.27 shows the implementation of Equation 3.25 in Simscape. It must be noted that a positive I_{charge} value results in a negative battery current. The fuel cell and battery models are the ones obtained in Sections 3.2 and 3.3 respectively. A load current versus time is applied to the load terminal on the right. Different simulations are run with this model to demonstrate that Equation 3.25 (and therefore Equation 3.24) is implemented in the different modes of operation. This is shown in Appendix E.

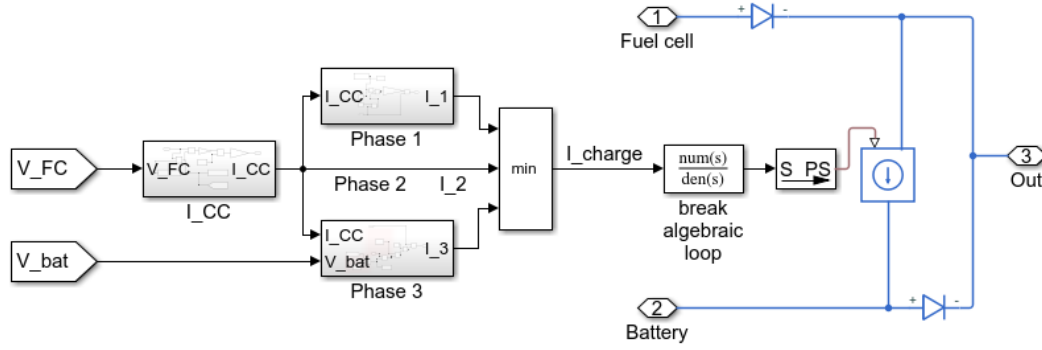


Figure 3.27: Simscape implementation of PMS model

3.5 Tank

Horizon Energy Systems has a range of hydrogen tanks designed for UAV applications (Horizon Energy Systems). The tank has an *empty tank mass* and can hold a certain *hydrogen mass* when full. A plot of this data is shown in Figure 3.28. It is assumed that custom tanks can be made and that the data points can be interpolated and extrapolated. This line is used for the parameter variation in Section 5.2. The hydrogen mass value becomes the $m_{remaining,0}$ value in Section 3.2.2.2.

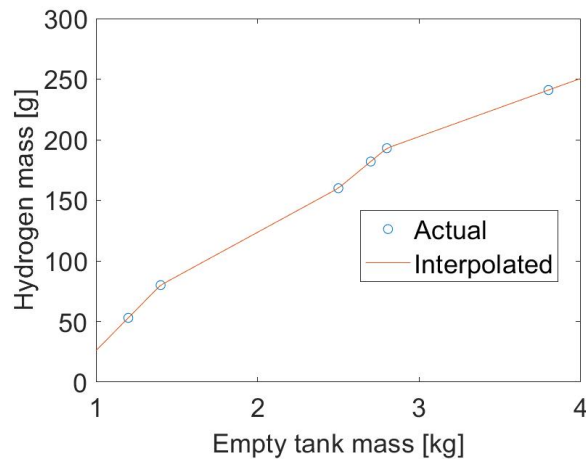


Figure 3.28: Hydrogen mass versus empty tank mass for discrete tank sizes. These discrete points are interpolated and extrapolated to obtain a function of hydrogen mass versus empty tank mass. Adapted from (Horizon Energy Systems)

Chapter 4

Load subsystem modelling

The load subsystem model is shown in Figure 4.1. It is composed of a *parasitic loss* model, four *propulsor* models and the *thrust duty cycle* model. The *parasitic loss* characterises power that is drained due to the flight control system and other auxiliary components. A *propulsor* is composed of an electronic speed controller (ESC), motor and propeller. It is assumed that a quadcopter is being modelled and therefore that there are four *propulsors*. The *thrust duty cycle* is the combined thrust from the four *propulsors* that needs to be applied over time, for the required flight path. These subsystems are modelled in this section.

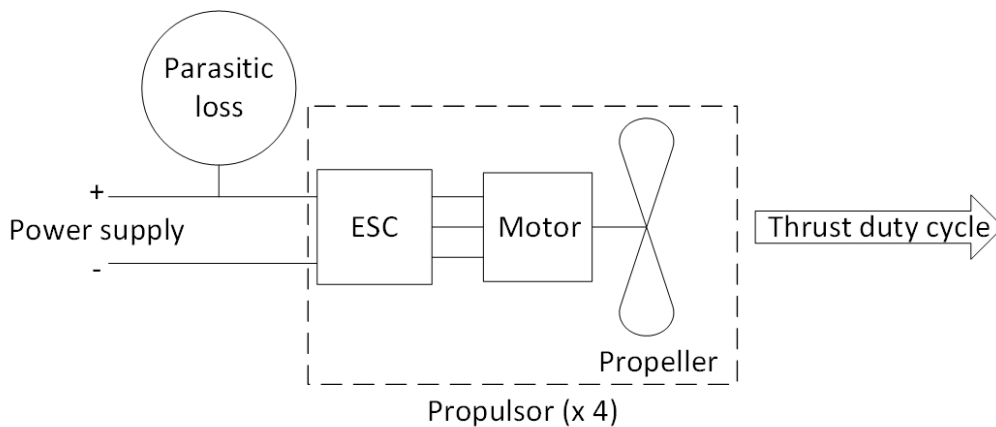


Figure 4.1: Load subsystem model overview

4.1 Propulsor system

A diagram of the propulsor system is shown in Figure 4.2. It is divided into an Electronic Speed Controller (ESC), motor and propeller. The motor is divided into an electrical model and a mechanical model.

Data is obtained from the manufacturer's website (T-motor), and used to fit a model. The manufacturer tests a combination of an ESC, motor and propeller and provides data of these tests. The combinations of components used in this section are listed in Table 4.1.

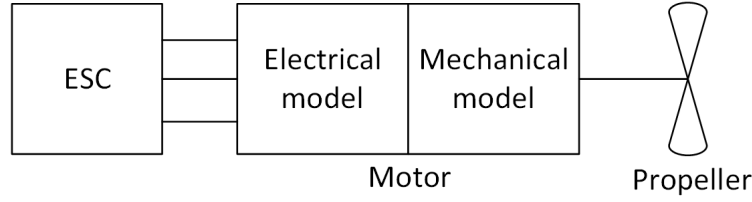


Figure 4.2: Propulsor system model overview

Table 4.1: Propulsor combinations: manufacturer data used for fitting model

ESC model	Motor model	Propeller diameter [inches]	Combination number
Alpha 60 A HV	U8 Lite 85KV	28	1
		29	2
	U8 Lite 100KV	27	3
		28	4
Alpha 60 A LV	U8 Lite 150KV	28	5
		29	6
	U8 Lite 190KV	28	7
		29	8
Alpha 60A HV	MN705-S 125KV	27	9
Flame 60A HV	MN705-S 260KV	27	10

4.1.1 Propeller and mechanical motor model

This section of the propulsor system includes the mechanical motor model and the propeller. Two similar models are developed. A more complex model takes into account the effect of friction. A simpler model doesn't. A diagram of the complex model is shown in Figure 4.3. The simple model is similar to this model, except that it does not include $Q_{motor\ friction}$.

Here follows the derivation of the complex model:

The mechanical resistance to rotation of the motor and propeller is characterised by the torque of the propeller and the mechanical friction of the motor. The propeller torque is mathematically modelled as follows:

$$Q_P = C_Q \rho D^5 \omega^2, \quad (4.1)$$

where Q_P is torque due to the propeller, C_Q is the propeller torque constant, ρ is the air density, D is the propeller diameter and ω is the speed of rotation of the motor shaft and propeller.

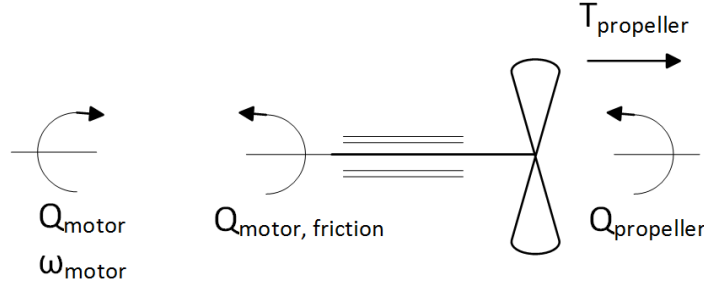


Figure 4.3: Mechanical motor model and propeller

It is assumed that the mechanical motor friction is due to a combination of viscous damping and coulomb friction. This torque is mathematically modelled as follows:

$$Q_f = C_{f,viscous}\omega + C_{f,coulomb}, \quad (4.2)$$

where Q_f is the torque due to friction in the motor, $C_{f,viscous}$ is the constant of viscous friction and $C_{f,coulomb}$ is the constant of coulomb friction.

The torque applied by the motor is equal to the sum of the torque components opposing the rotation of the motor:

$$\begin{aligned} Q_{motor} &= Q_P + Q_f \\ &= C_Q\rho D^5\omega^2 + C_{f,viscous}\omega + C_{f,coulomb}, \end{aligned} \quad (4.3)$$

where Q_{motor} is the total torque of the motor.

For the simple model, Equation 4.3 is modified to only include propeller torque:

$$\begin{aligned} Q_{motor} &= Q_P \\ &= C_Q\rho D^5\omega^2 \end{aligned} \quad (4.4)$$

For the data selected (Table 4.1), all the propellers are the same type (the *Glossy* model), with different diameters. It is assumed that these propellers are geometrically similar and therefore have the same C_Q value. It is assumed that the diameter of the propeller is that which is specified by the manufacturer. It is assumed that each motor model has its own unique construction and therefore its own unique $C_{f,viscous}$ and $C_{f,coulomb}$ values.

Information of the ambient temperature is given by the manufacturer for each test. However, information of the atmospheric pressure is not given. The

company's premises are close to sea level, so standard atmospheric pressure is assumed (101.325 kPa). The air density is calculated using a variation of the ideal gas law:

$$\rho = \frac{R_{air} T_{air}}{P_{air}} \quad (4.5)$$

where R_{air} is the gas constant of air and is equal to $287.05 \text{ J/(kg} \cdot \text{K)}$, T_{air} is the ambient air temperature and P_{air} is the atmospheric air pressure.

The thrust produced by the propeller is mathematically modelled as follows:

$$T = C_T \rho D^4 \omega^2, \quad (4.6)$$

where T is the thrust generated by the propeller and C_T is the propeller thrust constant.

This equation is independent of whether friction is modelled or not. The C_T value is the same for all propeller diameters.

Equations 4.3, 4.4 and 4.6 are fit to the 10 sets of manufacturer data. The resulting model parameters are listed in Table F.1 (Appendix F). The comparison between model fit and test data is shown in Figures 4.4, 4.5 and 4.6. The comparison between the accuracy of the complex and simple model is shown in Figure 4.7a. Combinations 9 and 10 weren't included in the model fit for the simple model. It seems that these motors have high friction values, reducing the accuracy of the fit for all the combinations.

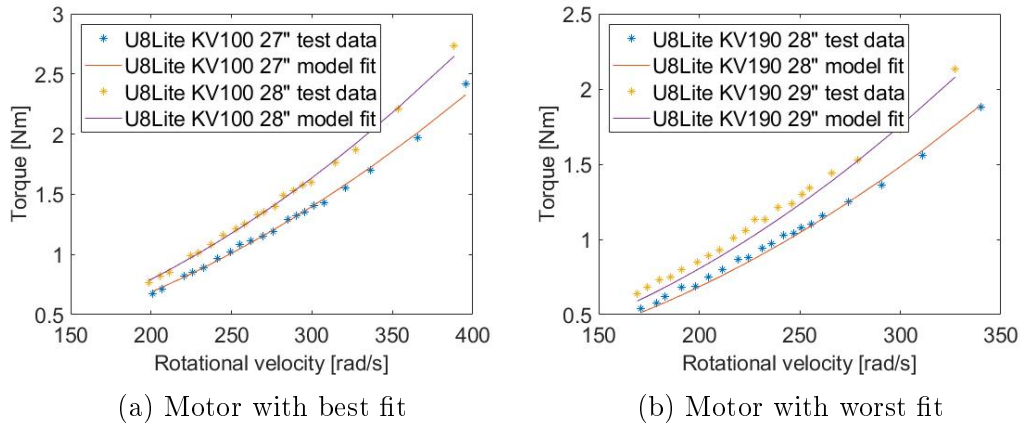


Figure 4.4: Comparison between model fit and manufacturer data - Torque - Modelling friction

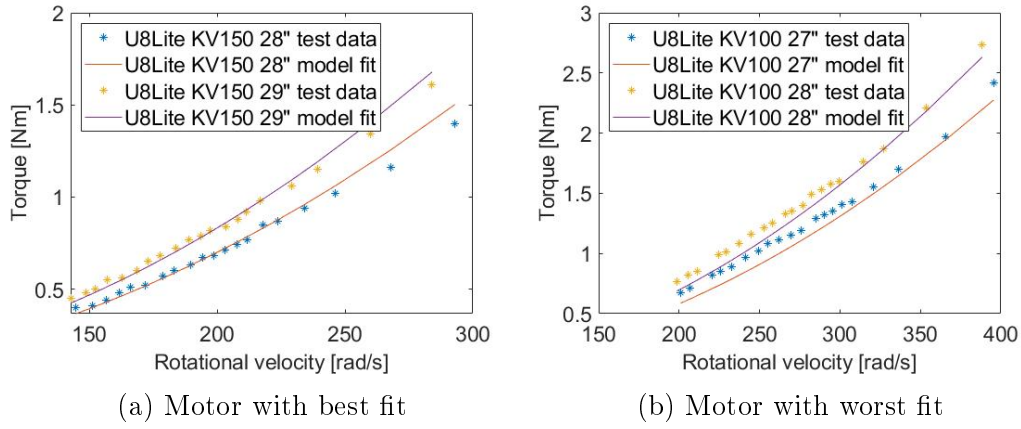


Figure 4.5: Comparison between model fit and manufacturer data - Torque - Not modelling friction

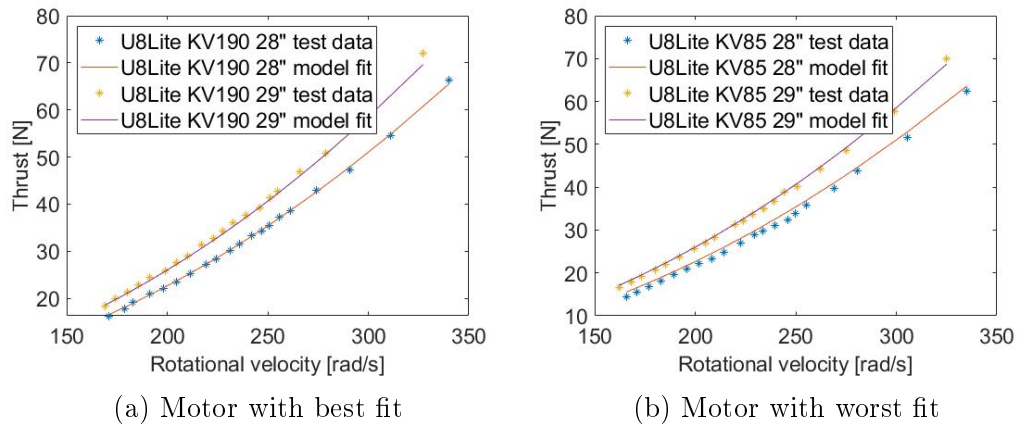


Figure 4.6: Comparison between model fit and manufacturer data - Thrust

4.1.2 Electrical motor model

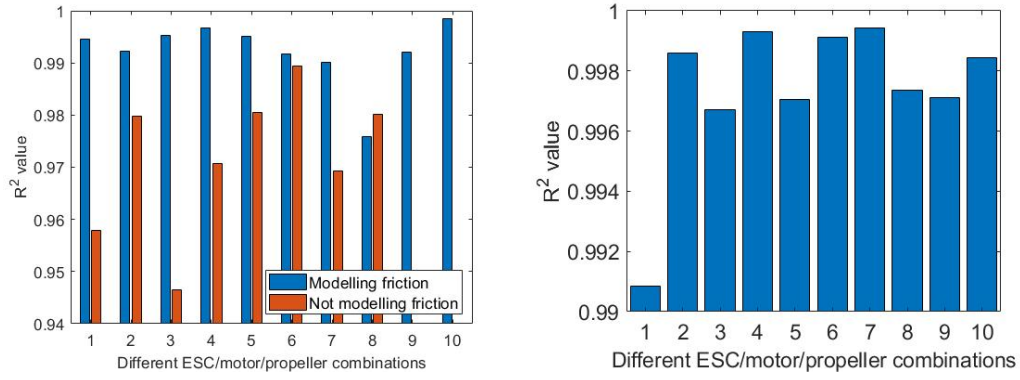
The electrical motor model is shown in Figure 2.13, with the equations described in Section 2.3.2.

4.1.3 Electronic Speed Controller

The ESC model used is shown in Figure 4.8. The validation of this model is shown in Appendix G. The unknown parameters R_1 and R_2 will be obtained in Section 4.1.4.

4.1.4 Total propulsor system

The aim of this section is to obtain a propulsor model. Component models previously described are combined to form the propulsor model. Experimental



(a) Comparing R^2 values of modelling friction to not modelling friction - Torque

(b) R^2 values - Thrust

Figure 4.7: R^2 values of mechanical motor model and propeller model fit

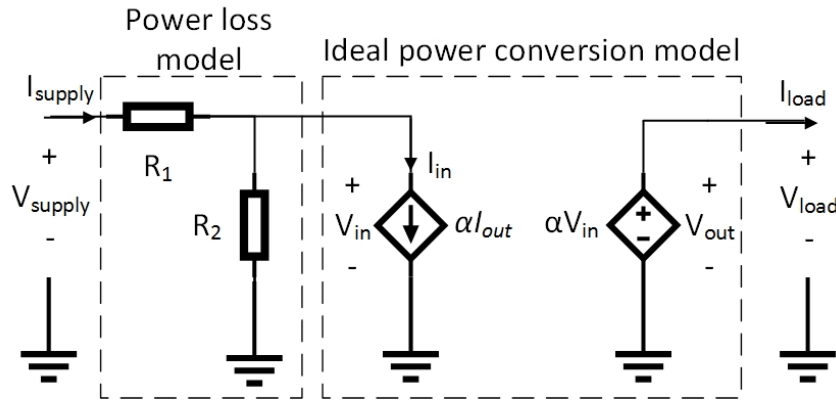


Figure 4.8: ESC equivalent circuit model

data of combinations 1 - 8 (Table 4.1) is fit to the model to obtain the unknown parameters. The propulsor Simscape model is shown in Figure 4.9.

So far constants have been obtained for the mechanical motor model and propeller model. Constants for the electrical motor model can either be obtained from manufacturer data, or can be obtained by the fitting process. The ESC parameters need to be obtained by the fitting process. Two models will be used, one complex and one simple.

The complex model contains the complex motor(mechanical)/propeller model, where friction is modelled. Different ESC parameters are fit for different motors i.e. the ESC parameter will change if it's connected to a different motor. The motor parameters will be obtained during fitting and will be allowed to be $\pm 15\%$ different to the manufacturer values.

The simple model contains the simple motor(mechanical)/propeller model, where friction isn't modelled. The ESC model parameters for an ESC will be the same regardless of the motor. The motor parameters will be the manufac-

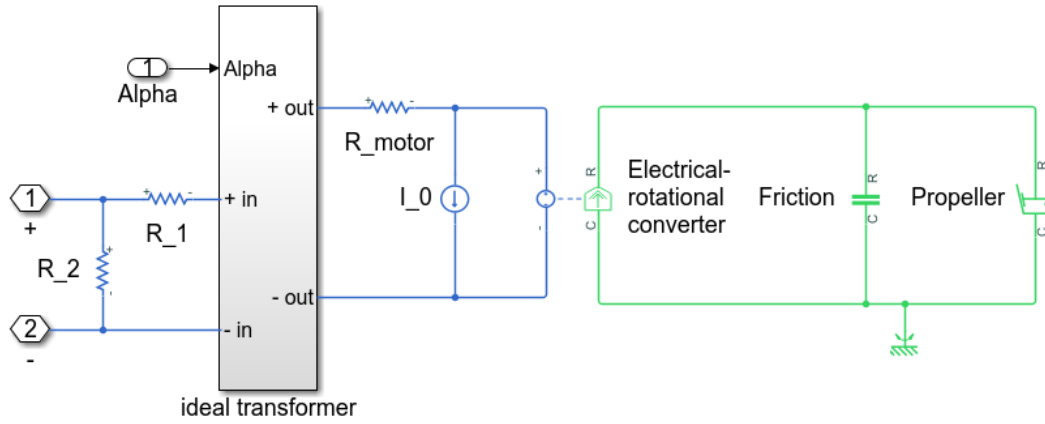


Figure 4.9: Propulsor model implemented in Simulink

turer values.

The resulting model fit is shown in Figure 4.10 for the complex model and Figure 4.11 for the simple model. A comparison of the accuracy between the two models is shown in Figure 4.12. Additional data, such as the constants of the two models, can be found in Appendix H.

4.1.5 Discussion

4.1.5.1 Propeller and mechanical motor model

This discussion is based on the results in Section 4.1.1. Two models were compared - one including friction (complex) and one not (simple). These models characterise the torque versus speed relationship. The model needs to be accurate enough that the error is small in comparison to the effect of changing a design parameter. The design parameter in this case is the propeller diameter, D .

Figure 4.5b shows the torque versus speed relationship predicted using the simple model. It can be seen that at lower speeds, the error is of a similar magnitude to the difference between the experimental data of the two propellers. This means that if the input to the model is $D = 28''$, it will predict results close to the experimental results of $D = 27''$, which is incorrect. This error reduces at higher speeds. However, multirotors are normally designed to not operate the motors at close to their maximum speeds.

The results in this figure (Figure 4.5b), are combinations 3 and 4 in Table 4.1. These combinations have R^2 values of approximately 0.945 and 0.97 respectively, for the simple model (Figure 4.7a). Other combinations are in this range, and close to this (mostly below $R^2 = 0.98$). This means that there is a low level of confidence in the predicted torque versus speed when varying the propeller diameter, for different motors.

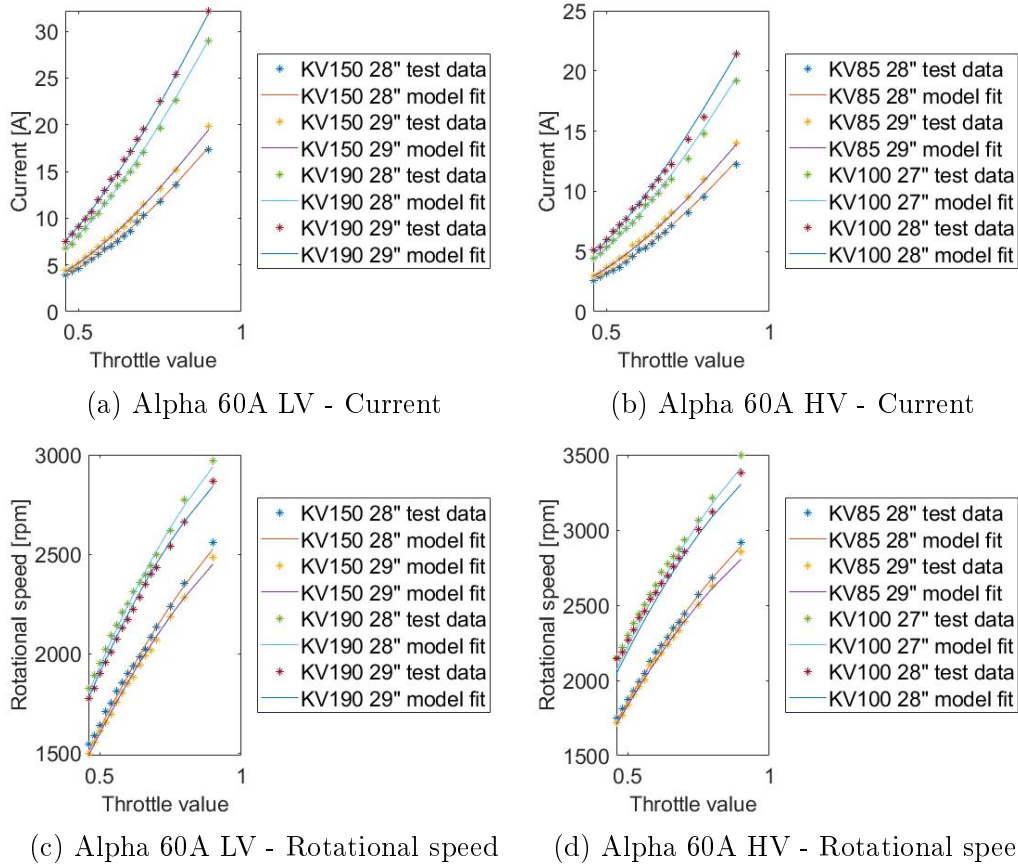


Figure 4.10: Comparison between model fit and manufacturer data - complex model

Figure 4.4b shows the torque versus speed relationship predicted using the complex model. For the 29" propeller (combination 8 - Table 4.1), the predicted results come close to the experimental results of the 28" propeller. However, the discrepancy is still better than with the simple model (Figure 4.5b). Also, this combination is an outlier, having an R^2 value of approximately 0.975, whereas the other combinations have an R^2 value of greater than 0.99. This means that most combinations modelled using the complex model have a goodness of fit similar to that shown in Figure 4.4a. This means that there is a high level of confidence in the predicted torque versus speed when varying the propeller diameter, for different motors.

Figure 4.6 shows the thrust versus speed relationship predicted. For combination 1 (Figure 4.6b), there is a discrepancy between the model and experimental results. However this is insignificant in comparison to the difference in experimental results between the two propeller sizes. Also this fit is an outlier, in that it has an R^2 value of approximately 0.991. The other combinations have an R^2 value of greater than 0.996, which can be seen in the model and experimental results being practically equal (Figure 4.6 - combinations 2, 7

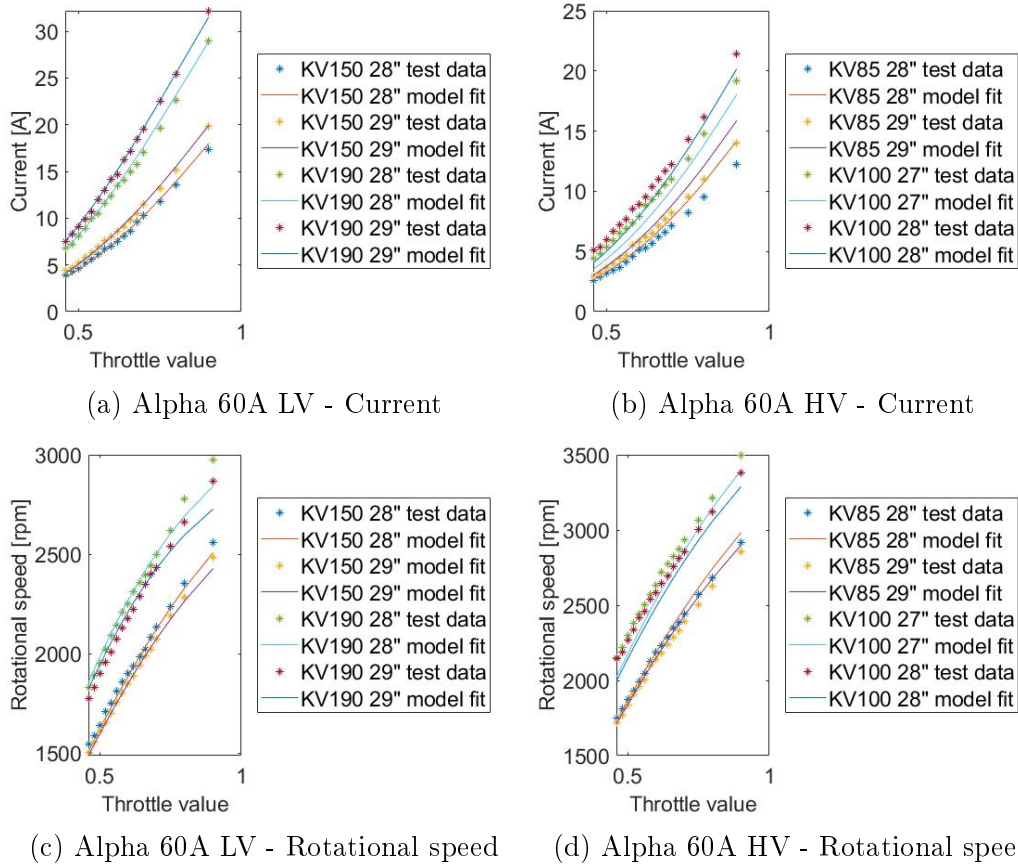


Figure 4.11: Comparison between model fit and manufacturer data - simple model

and 8).

It can therefore be concluded that with the complex model, the torque versus speed and thrust versus speed error is small in comparison to the experimental effect of varying the propeller diameter. This is not the case with the simple model.

4.1.5.2 Electronic speed controller

This discussion is based on the results in Appendix G and Section 4.1.3. Figure G.1 (and 4.8) shows the model proposed. This model is useful as it is easier to implement in Simscape than Equation G.2, which was validated in literature. Two complexities of this model were compared - one where the constants are dependent on the supply voltage (complex), and one where the constants are independent of the supply voltage (simple).

It can be seen that the accuracy of the simple model is quite low compared to the complex model. This can be seen by comparing the worst fits (Figures G.3b and G.4b), and by comparing the R^2 values in Table G.6. The R^2 values

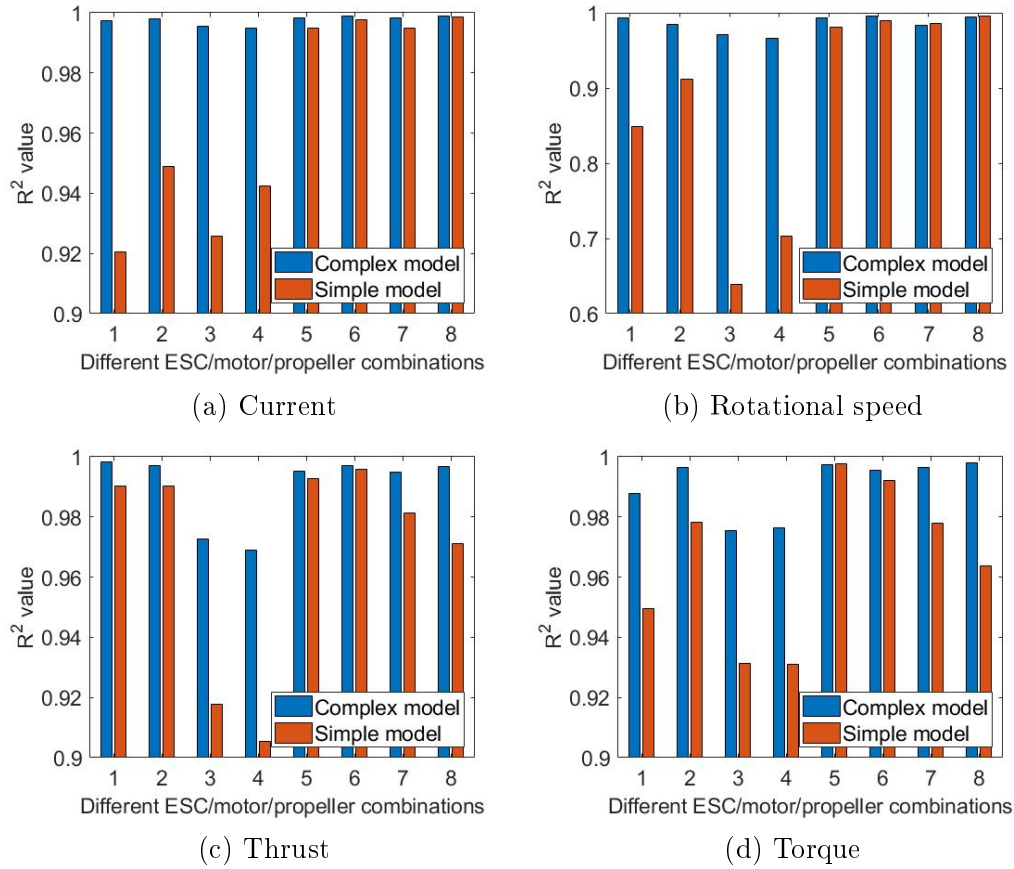


Figure 4.12: Comparing R^2 values of complex model with simple model

are only similar for supply voltages of 9 V and 10 V, because the simple model was fit using a supply voltage of 9.5 V. The further the supply voltage is from 9.5 V, the more inaccurate the simple model is. The implications of this will be discussed in Section 4.1.5.3.

With the complex model it can be seen that the higher the supply voltage, the lower the accuracy (Figures G.4 and G.6). The implications of this will be discussed in Section 4.1.5.3. It is interesting to note that there is a mathematical relationship for the constants as a function of the supply voltage, with a near-perfect fit (Figure G.5). This means that these equations can be used to extrapolate the model parameters beyond the supply voltages tested at.

4.1.5.3 Total propulsor system

This discussion is based on the results in Section 4.1.4. The best fit obtained is for the complex model with combinations 5 - 8. These combinations have a supply voltage of 24 V, and therefore make use of a low voltage ESC. It can be seen in Figures 4.10a and 4.10c that the model and experimental results are almost identical. The difference between the model lines, and between the

experimental lines, are of a similar magnitude. This gives confidence to the predicted results when varying the propeller diameter. Also, the R^2 values of these combinations are all above 0.98 for current, rotational speed, thrust and torque (Table 4.12). Additionally, the fit motor parameter values are close to the manufacturer-provided values (Table H.1), further confirming the accuracy of the model for these combinations. This accuracy is useful, as combination 5 is used in the system model (Section 5).

However, there is a shortcoming of using the complex propulsor model for combination 5 in the system model. The model parameters were obtained using a supply voltage of 24 V. However, the load voltage in the system simulation is 30 V – 40 V, during a certain timespan (Figure 5.3d). This load voltage is the supply voltage to the propulsors. As discussed in Section 4.1.5.2, the model parameters should be different for different supply voltages. The supply voltage in the system simulation is significantly higher than the supply voltage used to obtain the model parameters. This implies that the ESC model is inaccurate in the system simulation.

The accuracy is slightly worse for the high voltage combinations (1 - 4) using the complex model, as shown in Figures 4.10b and 4.10d. This is because of the decreasing ESC model accuracy with increasing supply voltage discussed in Section 4.1.5.2. The accuracy is even worse for the low voltage combinations (5 - 8) using the simple model, as shown in Figures 4.11a and 4.11c. This is because of the inaccuracy of not modelling friction discussed in Section 4.1.5.1. The high voltage combinations (5-8) using the simple model has the worst accuracy, as shown in Figures 4.11b and 4.11d. This is due to the combination of inaccuracies previously discussed.

4.2 Thrust duty cycle and parasitic loss

A LiPo quadcopter was flown by the authors using a pre-programmed flight path. The multirotor used was a quadcopter (four *propulsors*) with the details of the *propulsors* in Table 4.2. The flight was done without a payload and with a payload of 2 kg, resulting in the same flight, but with different take-off-masses. The current and voltage of the battery were measured and logged during flight. Power versus time was calculated using this data. This is shown in Figure 4.13.

From figure 4.13 it can be seen that the minimum power is non-zero and is the same for both all-up-masses. This is seen most clearly for time 170 s - 180 s. It is assumed that this power is due to parasitic loss from auxiliary components, and that the remaining power is due to the four *propulsors*.

Table 4.2: Propulsor components on quadcopter used in flight test - all components manufactured by T-motor

Component	Detail
ESC	Air 40 A
Motor	U8 Pro KV135
Propeller	Carbon fiber - glossy 27*8.8

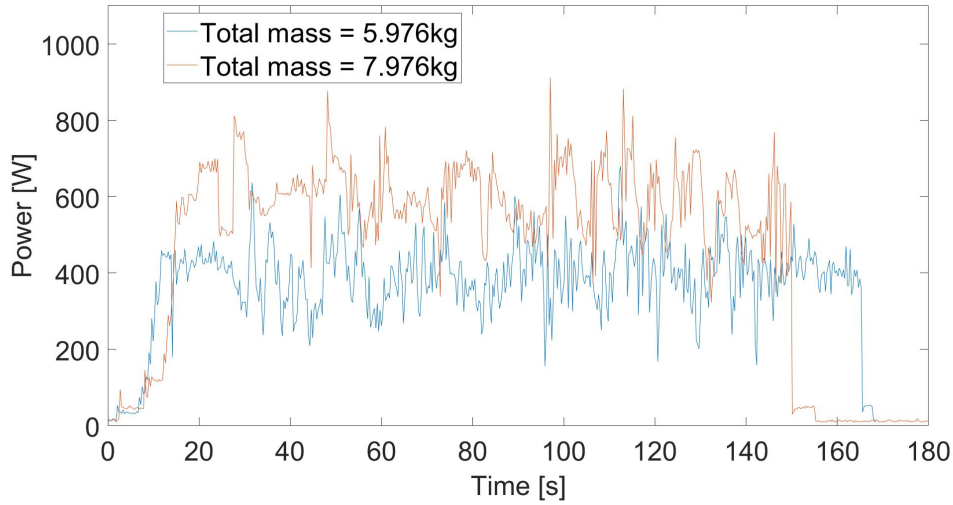


Figure 4.13: Measured power during flight test

4.2.1 Thrust duty cycle

4.2.1.1 Converting thrust duty cycle method

This section describes a method to predict the thrust duty cycle of a multirotor as a function of its mass. Experimental flight data is obtained from a multirotor. A model is developed to use this data to obtain a thrust duty cycle for a multirotor being designed with a different mass. It is assumed that the new multirotor will fly the same path, and that the frame, flight dynamics, etc. are similar enough that the duty cycle varies only as a function of the all-up-mass. The model will be used to convert the thrust duty cycle of the 5.976 kg flight (Figure 4.13) to a predicted thrust duty cycle for the 7.976 kg flight. This predicted thrust duty cycle is compared to the actual 7.976 kg flight thrust duty cycle.

In order to obtain a thrust duty cycle, the power duty cycle in Figure 4.13 needs to be converted to thrust. According to basic momentum theory, propeller power is related to its thrust (Silvagni *et al.*, 2018):

$$T = C_T \rho D^4 \omega^2 \quad (4.7a)$$

$$P_P = C_P \rho D^5 \omega^3 \quad (4.7b)$$

$$\therefore P_P = KT^{3/2}, \quad (4.7c)$$

where P_P is propeller power and K is a constant.

It follows logically that the *propulsor* power is related to thrust. The manufacturer supplies static power and thrust data for the *propulsor* system in Table 4.2 (T-motor). It is assumed that all four *propulsors* provide equal thrust and therefore draw equal power. The manufacturer data for thrust and power is therefore scaled by a factor of four, and shown in Figure 4.14. It is fit with a quadratic polynomial:

$$T_{total} = -4.1482 \cdot 10^{-6} P_{total}^2 + 0.0149 P_{total} + 1.0673 \quad [kg], \quad (4.8)$$

where T_{total} is the total thrust of the four *propulsors* and P_{total} is the total power drawn from the four *propulsors*.

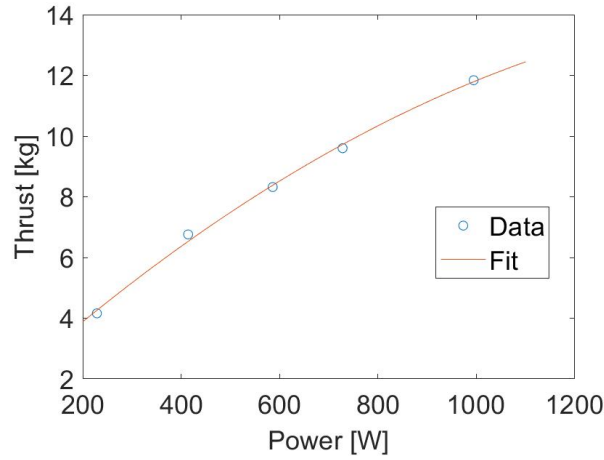


Figure 4.14: Thrust versus power of the propulsor used in the flight test

Now that the thrust duty cycle is obtained, the method used to convert the thrust duty cycle is described. It is described by Figure 4.15 and Equation 4.9:

$$T_{1,y} = m_1 k_1 \quad (4.9a)$$

$$T_{1,x} = \sqrt{T_1^2 - T_{1,y}^2} \quad (4.9b)$$

$$T_{2',x} = T_{1,x} \quad (4.9c)$$

$$T_{2',y} = m_2 \quad (4.9d)$$

$$T_{2'} = \sqrt{T_{2',y}^2 + T_{2',x}^2} \quad (4.9e)$$

$$T_2 = k_2 T_{2'}, \quad (4.9f)$$

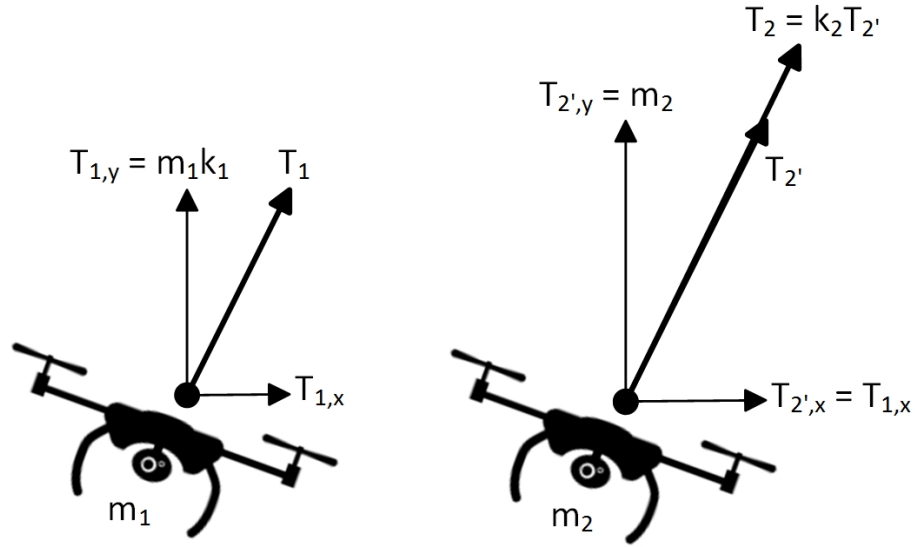


Figure 4.15: Geometric analysis to estimate thrust duty cycle with a different all-up-mass

where T_1 is T_{total} (Equation 4.8) for multirotor 1, T_2 is the predicted thrust duty cycle for multirotor 2, m_1 and m_2 are the all-up-masses for multirotor 1 and 2 respectively, and k_1 and k_2 are empirical constants.

Multirotor 1 and 2 refer to the all-up-masses of 5.976 kg and 7.976 kg respectively (Figure 4.13). The output of T_2 from Equation 4.9 is fit to the output of Equation 4.8 for multirotor 2, to obtain the empirical constants k_1 and k_2 . The results of the fit is listed in Table 4.3, with a comparison of the thrust duty cycles shown in Figure 4.16.

Table 4.3: Comparison of mean and standard deviation for the experimental and model thrust duty cycle, both for an all-up-mass of 7.976 kg

	Experimental	Model	Percentage error
Mean	8.4178 kg	8.4102 kg	-0.0909 %
Standard deviation	0.8550 kg	0.8547 kg	-0.0358 %

4.2.1.2 Converting thrust duty cycle for design case

Now that the thrust converting model (Equation 4.9), has been validated, it will be used with m_2 being the all-up-mass of the fuel cell multirotor being designed. An initial design will be selected in this section, to obtain a thrust duty cycle that will be used in Section 5.1. In Section 5.2, the all-up-mass will be varied as a result of varying certain design parameters.

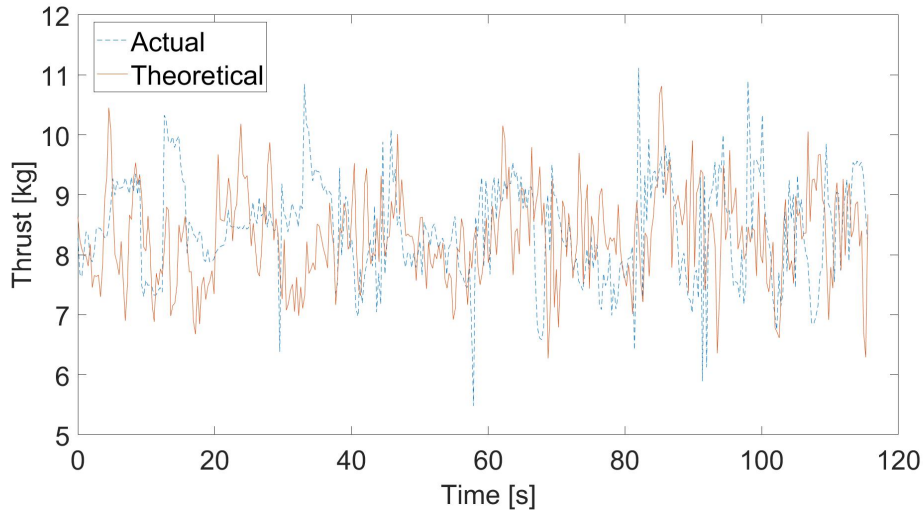


Figure 4.16: Comparison of experimental and model thrust duty cycle versus time, both for an all-up-mass of 7.976 kg

The following assumptions are made:

1. The current multirotor weighs 3 600 g without the battery or any payload. The new multirotor will weigh this amount as well, as it is a similar size, with similar *propulsor* components.
2. The new multirotor will have a payload of 1 000 g.
3. Half the hydrogen mass of a full tank is carried throughout the flight.

The power supply components of the new multirotor are shown in Figure 3.2 and listed with their masses in Table 4.4. The hydrogen mass of a full tank is calculated in Section 3.5. The total mass of the new multirotor is therefore:

$$\begin{aligned}
 m_{\text{new multirotor}} &= m_{\text{current multirotor}} + m_{\text{power supply}} + m_{\text{payload}} + \frac{1}{2}m_{H_2, \text{full tank}} \\
 &= 3600g + 5384g + 1000g + \frac{193g}{2} \\
 &= 10\,080.5g
 \end{aligned} \tag{4.10}$$

The method in Section 4.2.1.1 is then used to convert the thrust duty cycle with the current multirotor mass of 5 976 g (including the battery) to the new drone multirotor mass of 10 080.5 g. This theoretical thrust duty cycle is shown in Figure 4.18.

Table 4.4: Component masses of power supply system

Components	Mass [g]
Hydrogen tank	2 800
Fuel cell & fans	1 646
Pressure reducing valve	145
Controller/PMS 1	299
Controller/PMS 2	166
Battery 1	164
Battery 2	164
Total	5 384

4.2.1.3 Thrust control system

The *propulsor* system is modelled to have a throttle value as an input, with thrust as an output, and power drawn as an effect thereof. This is to represent how the system is physically operated. However, it is required to have thrust as an input. This is in order to have the thrust duty cycle described in Sections 4.2.1.1 and 4.2.1.2 as an input. The system describes how a PID controller is implemented in Simulink in order to convert a thrust input to a throttle input.

A PID compensator controller is used with the following equation:

$$P + I\frac{1}{s} + D\frac{N}{1 + N\frac{1}{s}}, \quad (4.11)$$

with the following constants: $P = 1$, $I = 1$, $D = 10^{-3}$, $N = 100$. These are the default settings of the PID compensator controller block in Simulink.

The implementation of the control system in Simulink is shown in Figure 4.17, with the simulation result in Figure 4.18.

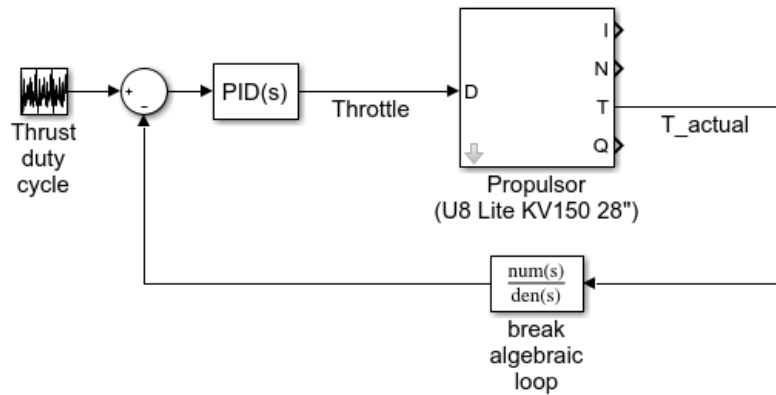


Figure 4.17: Thrust control system implementation in Simulink

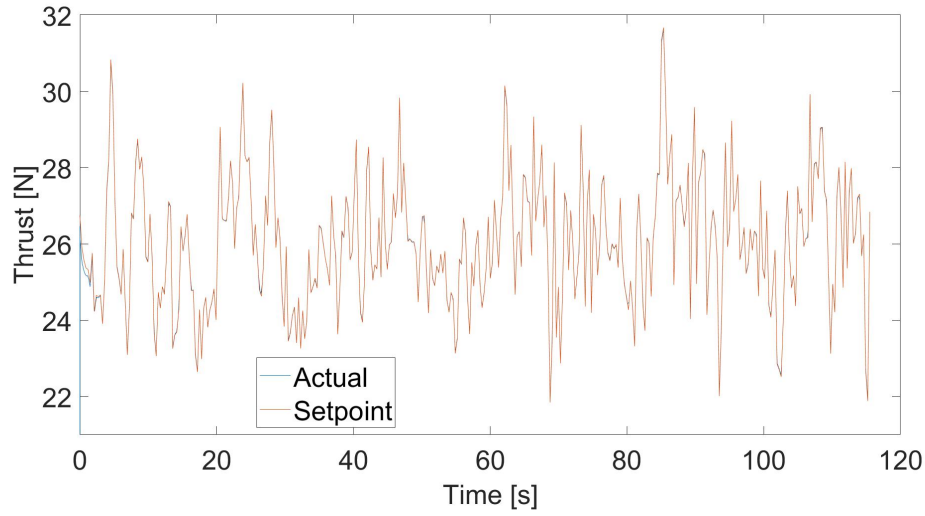


Figure 4.18: Simulation result - comparing actual and setpoint thrust versus time

4.2.2 Parasitic loss

As is described in the introduction of Section 4.2, there is a parasitic loss component of the power drawn. It is assumed that a constant power of 13 W is drawn, based on Figure 4.13. It is implemented in Simulink as a voltage-controlled current source, according to the following equation:

$$I = \frac{P_{\text{parasitic}}}{V}, \quad (4.12)$$

where I is the current drawn, V is the voltage measured and $P_{\text{parasitic}}$ is the desired constant power.

The Simulink model is shown in Figure 4.19.

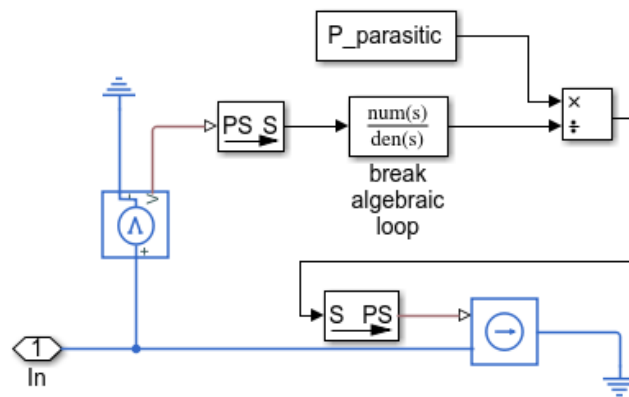


Figure 4.19: Simulink model of parasitic loss

4.2.3 Discussion

4.2.3.1 Thrust duty cycle

This discussion is based on the results in Sections 4.2.1.1 and 4.2.1.2. As can be seen in Table 4.3, the theoretical thrust duty cycle is similar to the actual one, in that the means and standard deviations are similar. Also, it can be seen from Figure 4.16 that the theoretical and actual thrust duty cycles have similar amplitudes.

However, there are the following limitations in the analysis:

1. Only one dataset was used to obtain the model parameters and validate the model. More datasets with different all-up-masses should be obtained.
2. The model was validated using an all-up-mass of 33.5 % greater. The thrust duty cycle for the initial design case is 68.7 % higher. There is a significant difference in these masses. Data should therefore rather be obtained from the new heavier multirotor, as this would avoid perturbing from the validated model too much.
3. the following assumption is made when using Equation 4.8: the supply voltage is 22.2 V throughout the flight, as this is the supply voltage at which the data in Figure 4.14 is obtained. However, it can be seen in Figure I.1 (Appendix I) that the supply voltage does vary during flight, with the first flight (5.976 kg) being mainly above 22.2 V, and the second flight (7.976 kg) being mainly below 22.2 V.

4.2.3.2 Thrust control system

This discussion is based on Figure 4.18. In the first few seconds, there is a discrepancy between the actual and setpoint thrust. Thereafter, the actual and setpoint is equal. The control system, therefore, performs its function.

4.2.3.3 Parasitic loss

This discussion is based on Section 4.2.2. The parasitic loss in this instance is 13 W, compared to the mean power drawn of about 900 W in the initial design (Figure 5.3b). This is about 1.4 % relative power loss, which might not seem that significant. However, it is useful to have this block for when more information is available on the type of payload used, and the power drawn from that. Based on the experience of a multirotor manufacturer, the parasitic loss from a payload can be significant, especially if the flight time is long.

Chapter 5

System model

The subsystem models from Chapters 3 and 4 are combined to form the system model. Simulations are done with this model. The *initial design* section shows the results of simulations with the thrust duty cycle obtained in Section 4.2.1.2. The *sensitivity study* section shows the results of varying the battery capacity and hydrogen tank mass.

5.1 Initial design

The system Simulink model is shown in Figure 5.1. The components used in the simulation are listed in Table 5.1. The simulation is run, with the input being the thrust duty cycle obtained in Section 4.2.1.2. The simulation is set to stop once the hydrogen mass remaining is zero (Equation 3.9), or if the battery voltage reaches its minimum (28 V). The results are shown in Figures 5.2 and 5.2, and Table 5.2.

Another simulation is run with the fuel cell model removed. This simulates what would happen if the fuel cell stops working. The reason for this simulation is that emergency flight time seems to be a design requirement of existing fuel cell multirotors (Gong and Verstraetey, 2014; Intelligent Energy, 2017; Horizon Energy Systems, 2012, 2014). The results of this simulation are also listed in Table 5.2.

Table 5.1: Components used in initial design system simulation

Component	Detail
Battery	2 x Tattu R-Line 4S 1300 mAh 75C (series connected to form 8S 1300 mAh 75C)
Hydrogen tank	2.8 kg (7.2 l; 300 bar; 163 g hydrogen)
ESC	Alpha 60 A LV
Motor	U8 Lite KV150
Propeller	28" Glossy (carbon fibre)

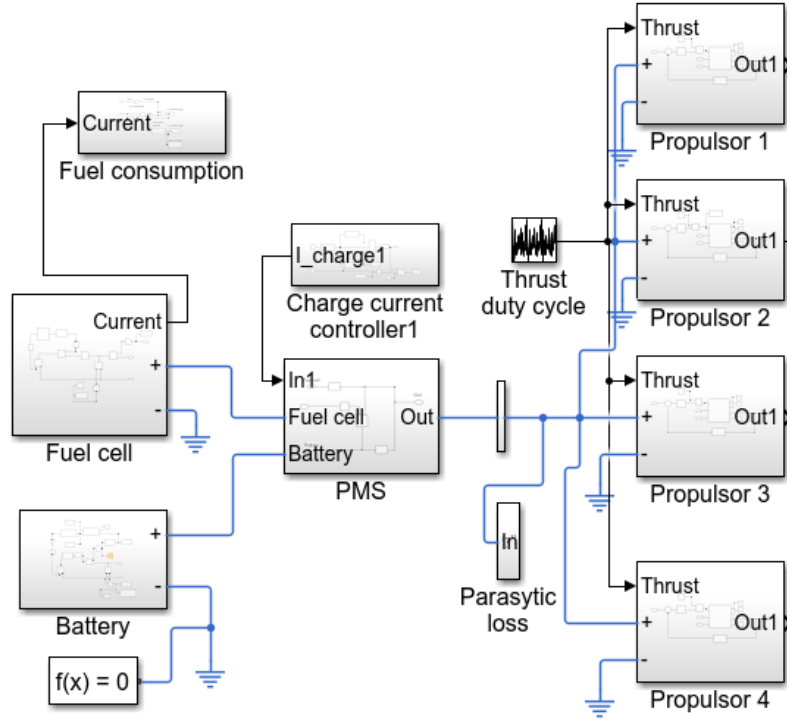
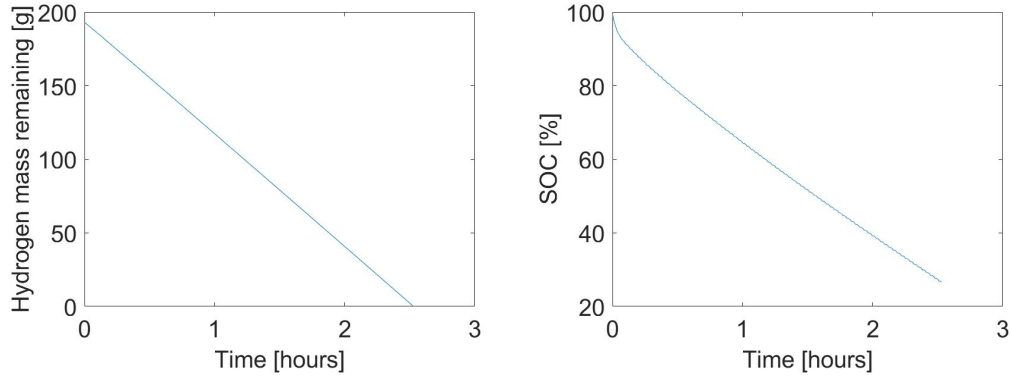


Figure 5.1: Simulink system model



(a) Hydrogen mass remaining over entire simulation (b) Battery SOC over entire simulation

Figure 5.2: Capacity remaining over entire simulation, for the two energy sources, hydrogen tank and battery

5.1.1 Discussion

The theory of operation of a passive PMS (Section 2.1.8.1) can be seen in Figures 5.3c and 5.3d. When the load current is low, the load voltage is high (Figure 2.9d). If the load voltage is above the battery's OCV, the fuel cell

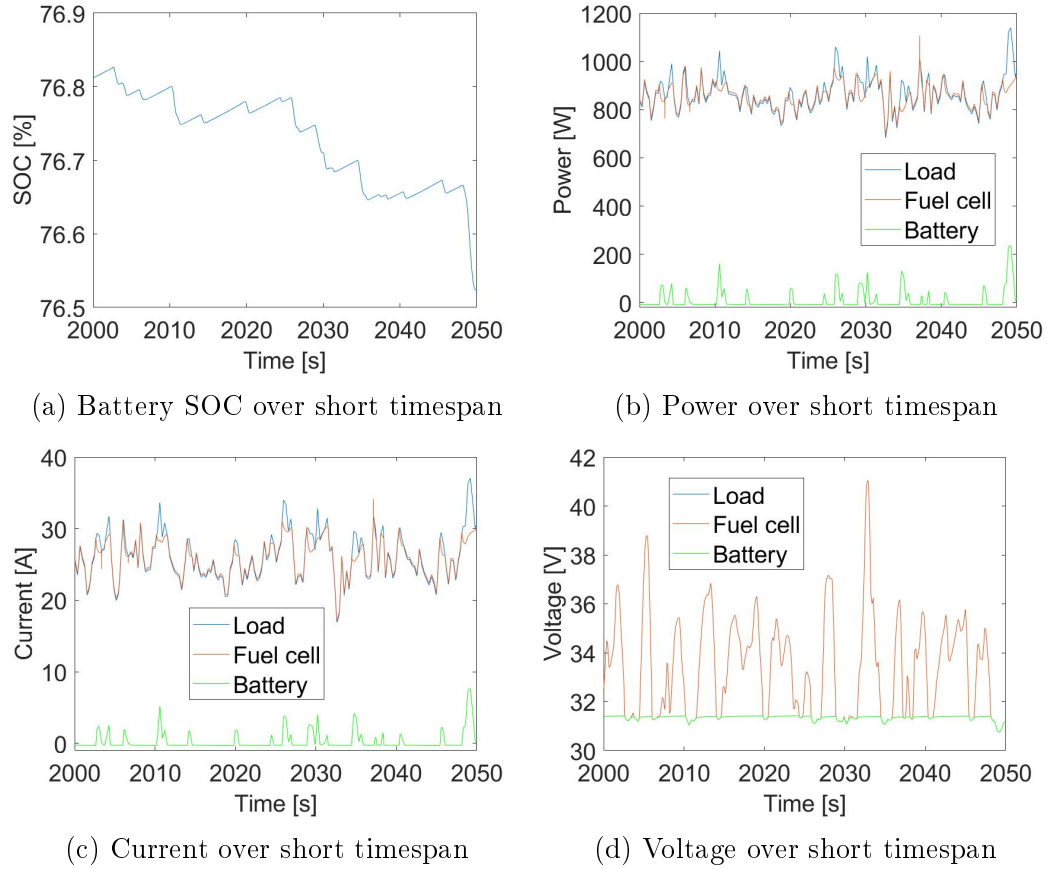


Figure 5.3: Simulation measurements over short timespan

Table 5.2: Simulation results for the initial design

Simulation	Variable	Value
Overall	All-up-mass	10.08 kg
	Maximum thrust	32.56 kg
	Thrust ratio	0.31
Normal flight	Flight time	2.53 hours
	Hydrogen mass remaining	0 g
	SOC remaining	26.70 %
Emergency flight	Emergency flight time	20.14 s
	Max C-rate	28.75

voltage is equal to the load voltage. If the load voltage is below the battery's OCV, all three voltages are equal.

It can be seen that the following always remains true: $I_{\text{Load}} = I_{\text{Fuel cell}} + I_{\text{Battery}}$ and $P_{\text{Load}} = P_{\text{Fuel cell}} + P_{\text{Battery}}$. If the load voltage is high, the fuel cell current is higher than the load current, as some of the fuel cell's current is used to charge the battery. If the load voltage is low, the load current is higher

than the fuel cell voltage, as the battery supplies current to accommodate this discrepancy.

As is expected, when the battery's current is positive, SOC reduces, and when it's negative, SOC increases (Figure 5.3a). The SOC decreases and increases over a short timespan, but the general trend is continuously decreasing (Figure 5.2b).

The hydrogen mass is depleted, causing the simulation to stop (Figure 5.2a), with the battery still having 26.70 % SOC. The remaining SOC can be seen as a safety factor. It is generally not recommended to deplete the battery too low, as this could damage the battery and fuel cell (lower battery voltage causes lower fuel cell voltage, due to their direct diode connection). Also, due to possible discrepancies between the simulation, and actual flight, the battery might deplete further than predicted. Due to these reasons, there should be a certain margin in SOC remaining predicted. Also, if the battery is depleted first, it wastes the hydrogen which has a higher energy density.

Based on information of existing fuel cell multirotors, it seems that the manufacturers design for redundancy of the fuel cell system. This means that these manufacturers design the multirotor to be able to fly a short period of time powered solely by the battery. In order for this to occur, the battery's maximum rated C-rate needs to be higher than the maximum C-rate drawn. This is the case as the battery's rated maximum C-rate of 75 is higher than the maximum C-rate drawn of 28.75 (Table 5.2). The emergency flight time of 20.14 s is significantly less than the emergency flight time of 120 s of other manufacturers.

5.2 sensitivity study

As discussed in Section 5.1.1, the major shortcomings of the initial design is that the battery SOC remaining is low, and the emergency flight time is low. In this section it will be demonstrated that the model can be used to obtain a new design with an increase in SOC remaining, while still maximizing flight time.

The objective is to obtain an SOC remaining value of at least 35 %, while maximizing flight time.

The battery capacity and hydrogen tank mass was varied. The simulation results are shown in Figure 5.4. A point on these plots was found where the SOC remaining is greater than 35 %, with a high flight time. This point is detailed in Table 5.3, and compared to the details of the initial design.

5.2.1 Discussion

The aim of the analysis in Section 5.2 was to obtain a design with a predicted SOC of at least 35 %, while still maximizing flight time. It can be inferred from

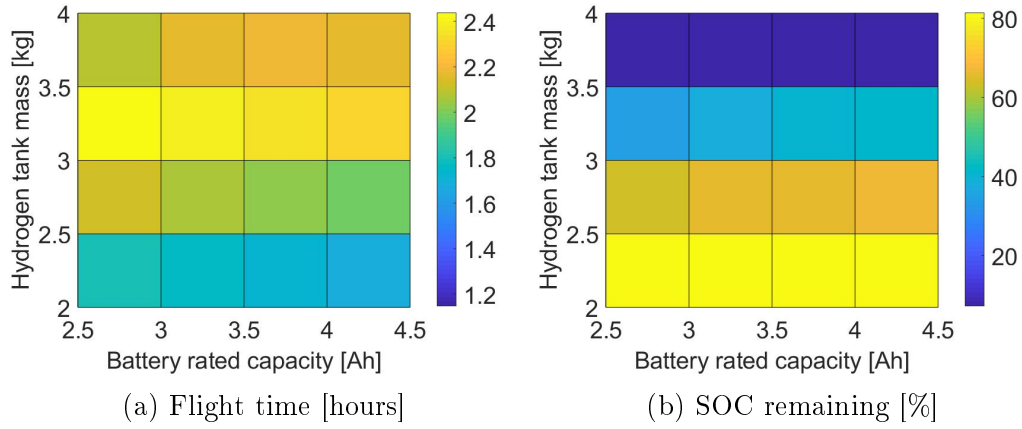


Figure 5.4: Simulation results as a function of varying battery rated capacity and hydrogen tank mass

Table 5.3: Comparison of initial design with design obtained from sensitivity study

Results and design parameters	Initial design	Sensitivity study	Percentage difference
Flight time	2.53 hours	2.39 hours	-5.54 %
Battery SOC remaining	26.70 %	38.09 %	42.66 %
Tank mass	2.8 kg	3 kg	7.14 %
Battery capacity	1.3 Ah	3 Ah	130.77 %
All-up-mass	10.08 kg	10.71 kg	6.25 %

Table 5.3 that this was achieved. The SOC remaining increased by 42.66 %, with the flight time decreasing only 5.54 %. This increase in the SOC remaining predicted gives greater certainty that the predicted flight time will be achieved.

The system model is not validated, however it can be partly verified by comparing it to the flight times of existing fuel cell multirotors. These are fuel cell multirotors able to carry 1 kg payload, same as this system: hexacopter (2.8 hours) (Horizon Energy Systems, 2018), quadcopter (2 hours) (EnergyOR, 2016) and X8 multirotor (1.83 hours) (FlightWave, 2018). The results obtained in Table 5.3 (2.39 hours) are therefore in the range of what exists on the market.

Some interesting trends can be seen in Figure 5.4. It seems 3 kg tank mass gives the highest flight time, with higher and lower tank masses reducing the flight time. It is not shown here, but increasing the tank mass too much can result in only a few minutes flight time. Increasing the tank mass reduces the SOC remaining.

There is a conflicting relationship when varying the battery capacity. Increasing the battery capacity increases the SOC remaining (in the range analysed), but decreases the flight time.

Chapter 6

Conclusion

6.1 Summary of findings

The aim of this work was to create a software design tool, useful for helping design a fuel cell multirotor. For it to be useful, it needs to be accurate, and able to provide insights useful for design.

It was found with the component models that the error was mostly small in comparison to the effect of varying a parameter. This gives confidence to the predicted effect of varying parameters. For models where parameters were not varied, the %RMSE values of the main variables were below 3 %. The predicted flight time of the system model is in the range of existing similar products.

The system model is useful in that it gave insight into the limitations of the initial design. Parameters could then be varied to improve on a specific design objective. In this instance, SOC remaining was increased, with minimal reduction in flight time. The benefit of this was discussed.

6.2 Implications of this work

Multirotors are normally custom-designed for a specific application. The work done shows the potential of having a software design tool, to aid in designing a multirotor with longer flight time than current LiPo multirotors, for a specific application.

6.3 Limitations of this work

Simplifying assumptions were made in the modelling approach. The system model wasn't validated. The usefulness of varying only two parameters was demonstrated.

6.4 Recommended future research

6.4.1 Using author's own experimental data

Most of the data used to obtain the models in this work is from literature of similar systems, and manufacturer-provided data. Future work should use more of the author's own experiments. This would increase the accuracy. Examples include:

1. The fuel cell system procured (including its PMS) should be tested. This data should be used for modelling. Its operation might be different to that of the similar systems used in literature, from where data was obtained for this work.
2. The manufacturer-provided propulsor data of the system used in this work was tested at 24 V, whereas its operation is predicted to be at 30 V - 40 V. The propulsor should therefore be tested at these voltages, and this data should be used for modelling.

6.4.2 Validating system model

Based on this work, a fuel cell multirotor prototype can now be assembled. This system should be flown, with measurements taken. This measured data should be compared to the model-predicted data. Possible discrepancies can be decreased by increasing the complexity of certain component models. This can be done based on the shortcomings of certain models discussed in this work.

6.4.3 Increasing number of parameters that can be varied

The following improvements in parameter variation can be done:

1. Battery: Currently number of cells and rated capacity. The author can also include whether LiPo (max 4.2 V/cell) or LiHV (4.35 V/cell) battery used, and C-rate (which determine internal resistance).
2. Propulsor: Currently KV values are discrete data-sets, and propeller diameter can be varied in continuous space. The author can also make KV values and associated motor parameters continuous data, and can include different propeller types, such as T-motor's folding and ultra-light products.

Appendices

Appendix A

Discussion of scope limitations in this project

This appendix outlines a proposed framework for achieving the overall aim of having a validated system model. It also discusses which components of this framework were focused on in this work, and why.

Figure A.1 shows the overall work that should be done in order to obtain a validated mathematical model of a fuel cell propulsion system for a multicopter (in my opinion). It was considered too basic (not masters level) to focus on the simple modelling and initial component selection. The development of fuel cell multicopter and assembly of system bench test setup is a lot of work with many practicalities i.e. it is an engineering project, but not an academic/scientific project. The only academic value of this development would be the measurements at the end. It is therefore a lot of work (and money) with little academic value. It was therefore decided to focus on subsystem detailed modelling and validation, as this focuses on academic disciplines such as literature review, experimenting and modelling.

A part of the refined component selection was done to demonstrate the usefulness of the research. More work could have been done here, as interesting insights could have been obtained, further aiding in component selection and design optimization. However, it was felt that this would make the scope too large. The title, and therefore scope, is modelling of the system and not modelling and design.

APPENDIX A. DISCUSSION OF SCOPE LIMITATIONS IN THIS PROJECT 85

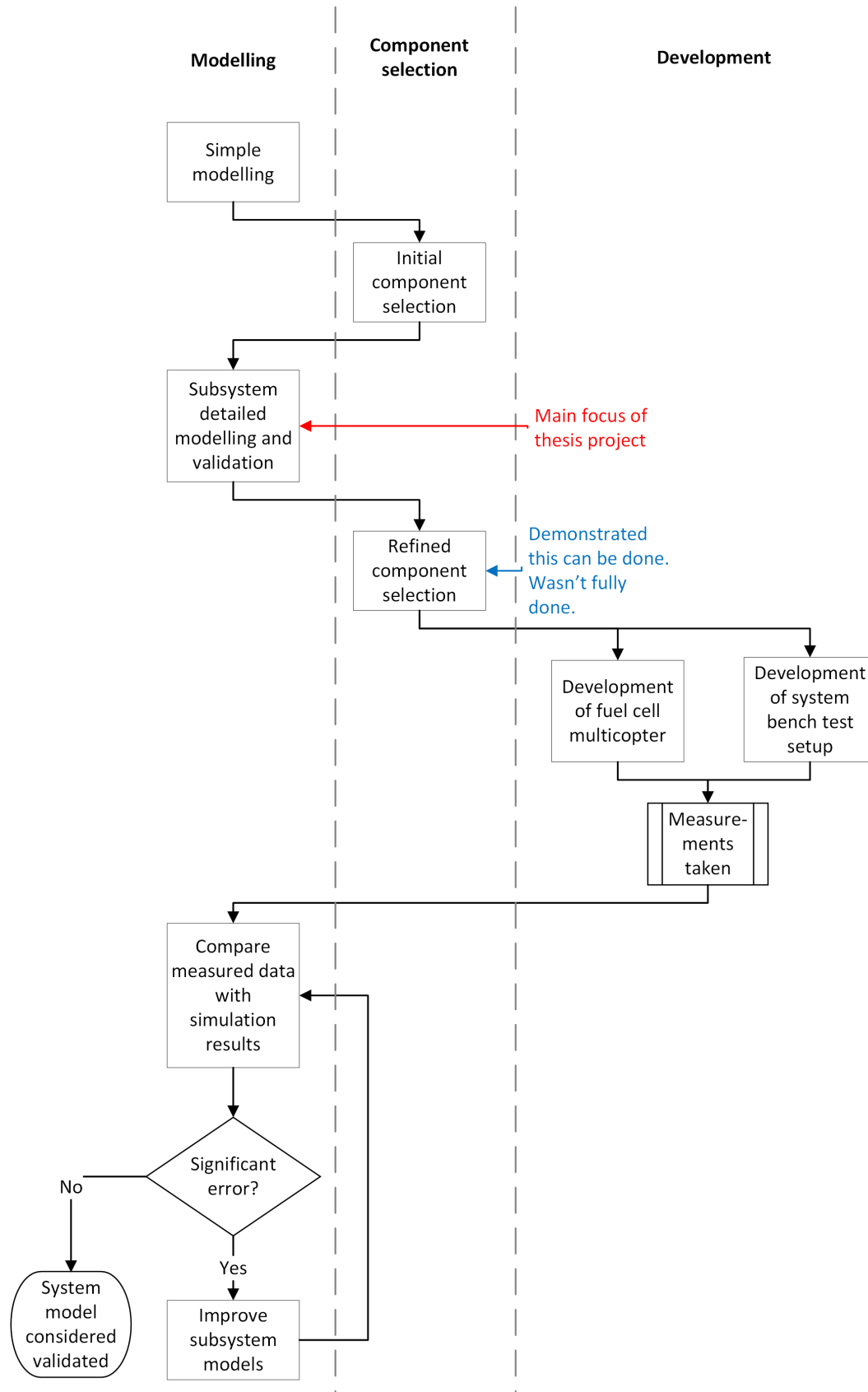


Figure A.1: Proposed overview of larger project

Appendix B

Modelling of system used to obtain transient fuel cell model

With reference to Figure B.1, the components to be modelled are the fuel cell steady-state model, the battery steady-state and transient models, and the diode.

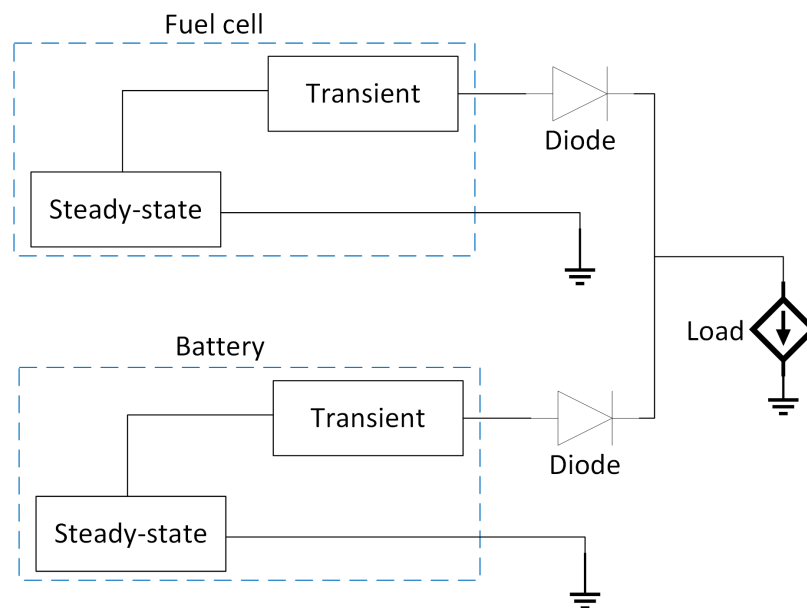


Figure B.1: Experimental setup divided into sub-models

B.1 Fuel cell steady-state model

The fuel cell used is a *Schunk FC-42*. The polarization curve (Figure B.2a) is programmed into a look-up table in Simscape, as shown in Figure B.2.

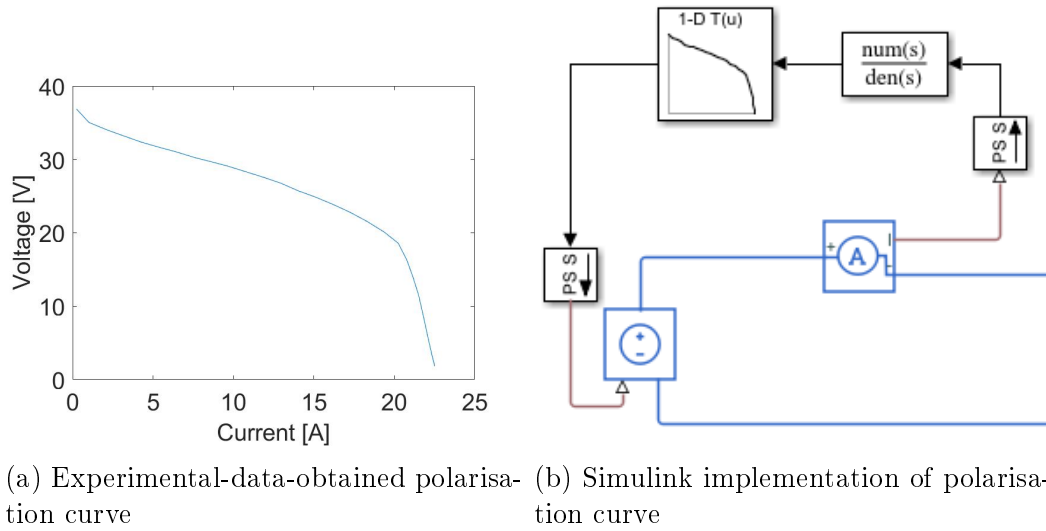


Figure B.2: Fuel cell model

B.2 Battery transient model

The battery used is a *Lithium ion module ALM12V60*. The battery used in this work (Section 3.3) is a *Tattu R-line 1300mAh 8S 75C* Lithium polymer battery. It is assumed for simplicity that because the two batteries are both lithium-based, they have similar transient models. This transient model is obtained in Section 3.3. The model is shown in Figure B.3.

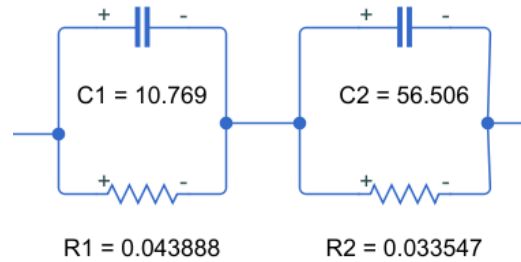


Figure B.3: Battery transient model

B.3 Battery steady-state model

The steady-state polarization curve of the *ALM12V60* battery is shown in Figure B.4a. The model fit to the curve is shown in Figure B.4b. It is assumed that the battery is discharged for short enough periods that the open circuit voltage, V_{OC} , is independent of SOC i.e. it is a constant voltage source.

The following equations were used to obtain the parameters V_{OC} and R_0 :

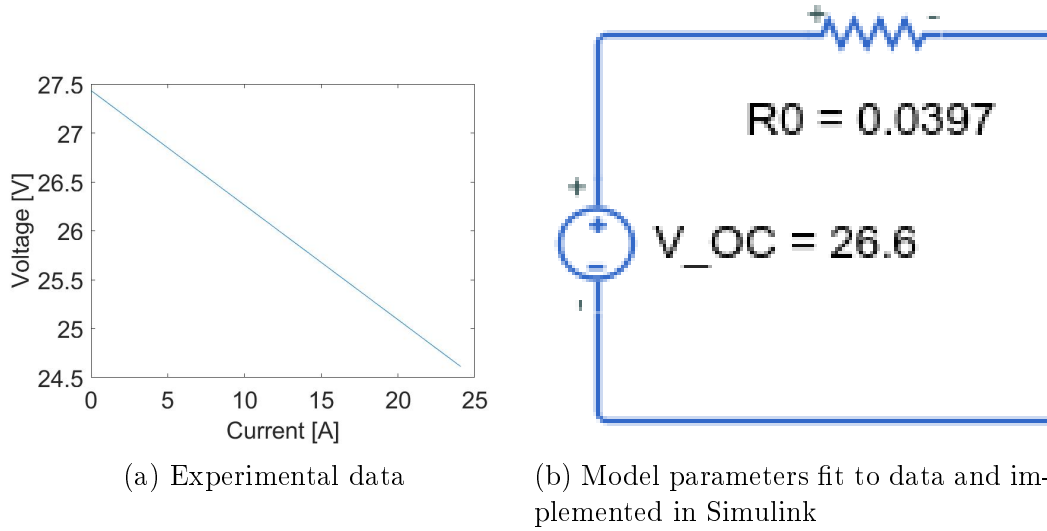


Figure B.4: Battery steady-state model

$$V = V_{OC} - IR_{total} \quad (B.1)$$

Equation B.1 was fit to the data in Figure B.4a to obtain $V_{OC} = 27.43V$ and $R_{total} = 0.1172\Omega$.

R_0 is obtained from the following equation:

$$R_{total} = R_0 + R_1 + R_2, \quad (B.2)$$

where R_1 and R_2 are parameters from the battery transient model. It was found that in the experiment of interest, the battery voltage with no current drawn is 26.6 V. Therefore, this became the value for V_{OC} . The parameter values are shown in Figure B.4b

B.4 Diode model

The diode is a *Schottky rectifier IOR 40CP060*. It is assumed that the junction temperature is $25^\circ C$. The voltage drop versus current for this junction temperature is shown in Figure B.5.

The following equation is fit to the data in Figure B.5:

$$V_{diode} = V_{diode0} - IR_{diode}, \quad (B.3)$$

where V_{diode} is the voltage drop across the diode, V_{diode0} is the voltage drop at zero current, and R_{diode} is the internal resistance. The following parameter values are obtained: $V_{diode0} = 0.3402V$ and $R_{diode} = 0.0092\Omega$. $R^2 = 0.9914$.

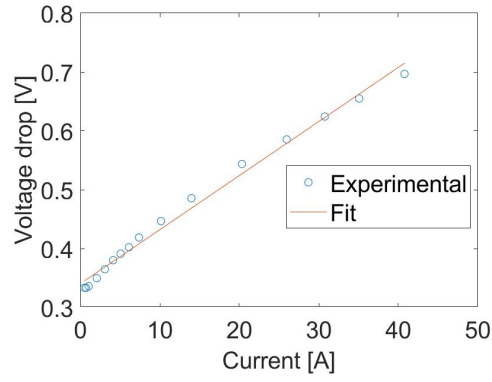


Figure B.5: Diode data from datasheet - fit with model

B.5 Summary

Excluding the fuel cell transient model, the model of the experimental setup, with parameter values is shown in Figure B.6.

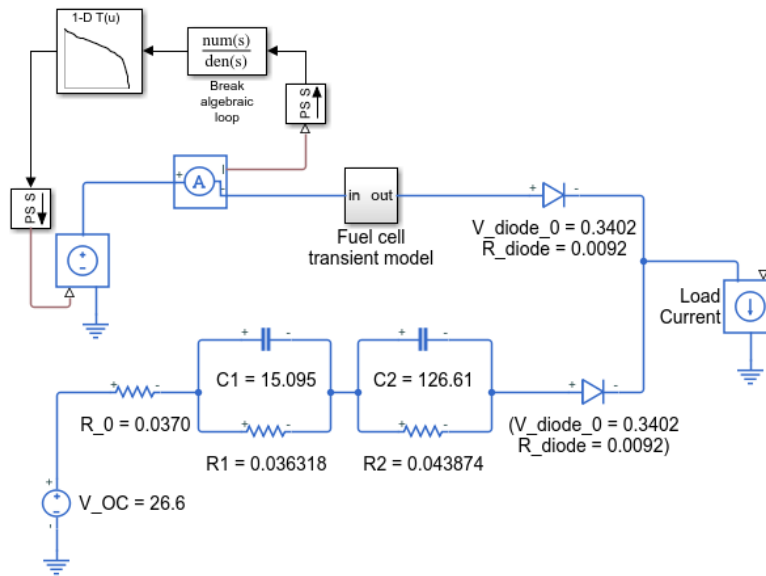


Figure B.6: Model constants obtained for experimental setup - excluding fuel cell transient model

Appendix C

Calibration of current sensor

A current sensor is calibrated, with a DC electronic load as the reference. The current sensor outputs a voltage, so it is necessary to find a relationship between this output voltage, and the current value. The experimental setup is the same as the battery experimental setup (Section 3.3.2). The current sensor is inverted in order to calibrate it for negative current values, which occurs during battery charging, which is the range in which the sensor will be used. The *auxiliary power supply* supplies power to the current sensor, *CAN module* and *CAN logger*. The *main power supply* is set to 1 V. The *DC electronic load* is stepped through a range of current values. The output voltage of the *current sensor* is measured and conditioned on the *CAN module* and logged on the *CAN logger*. The results are shown in Figure C.1a.

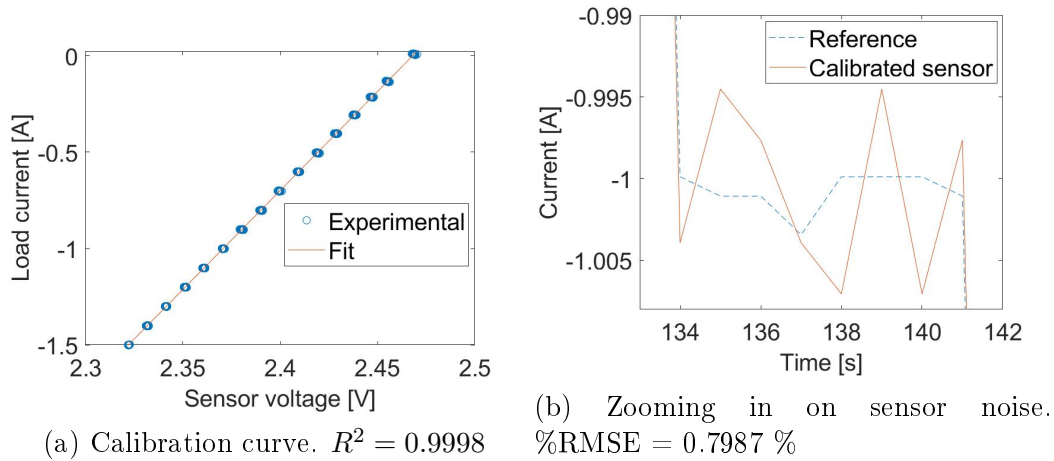


Figure C.1: Obtaining calibration curve

A first degree polynomial is fit to the results to obtain the following relationship:

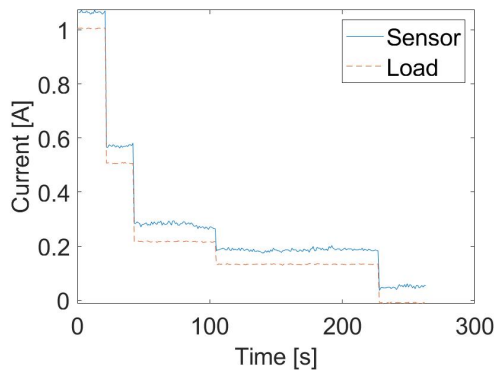
$$I = 10.2644V_{\text{sensor}} - 25.3335 \quad \text{for} \quad -1.5 \leq I \leq 0, \quad (\text{C.1})$$

where V_{sensor} is the voltage output from the sensor.

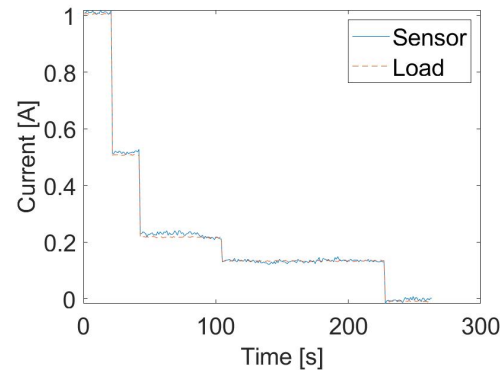
Figure C.1b shows the current readings from the DC electronic load (the reference) and the interpreted current reading from the sensor. It can be noted that there is uncertainty in the sensor measurement. This uncertainty can also be seen in Figure C.1a, with the sensor voltage uncertainty for a current value.

It was found during an experiment that a further offset was needed, probably due to experiments and calibration being performed on different days. The results without the offset (Figure C.2a) and with the offset (Figure C.2b) are compared. Equation C.1 then becomes:

$$I = 10.2644V_{sensor} - 25.3874 \quad (C.2)$$



(a) Without offset - %RMSE = 27.7015 %



(b) With offset - %RMSE = 15.7992 %

Figure C.2: Modifying calibration equation

Appendix D

Battery and fuel cell models for PMS data

D.1 Fuel cell

For the fuel cell, data from Figure D.1a is used to develop a model, which makes use of a look-up table, as shown in Figure D.1b.

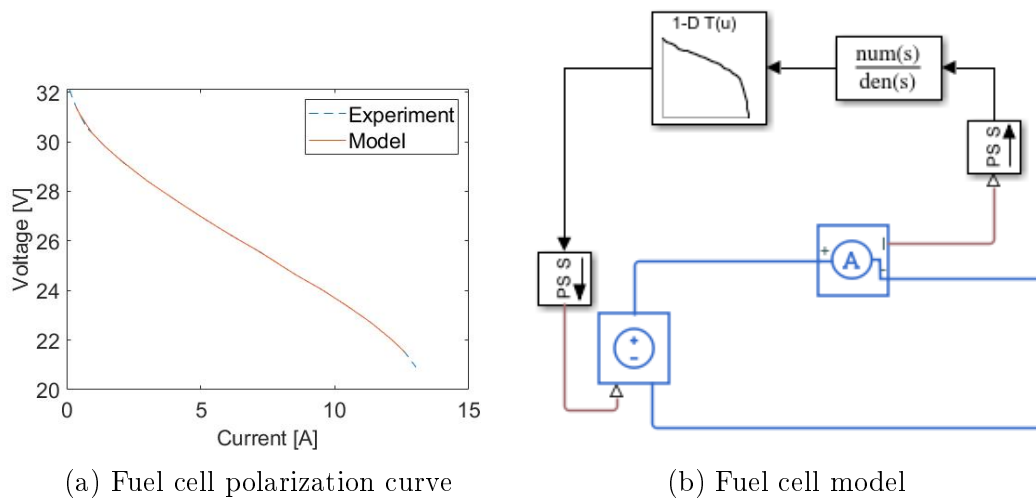


Figure D.1: Fuel cell model

D.2 Battery

For the battery model, the ideal would have been to test the battery used by Gong, and then model it according to the process in Section 3.3.3. However, to the author's knowledge, it is almost impossible to import the exact battery

Table D.1: Battery model constants

Constant	Value
K_1	-12.1574
K_2	12.8874
K_3	20.9547
K_4	-0.5420
A	0.1641
V_0	25 V
R	0.0811 Ω
C_n	1.4 Ah

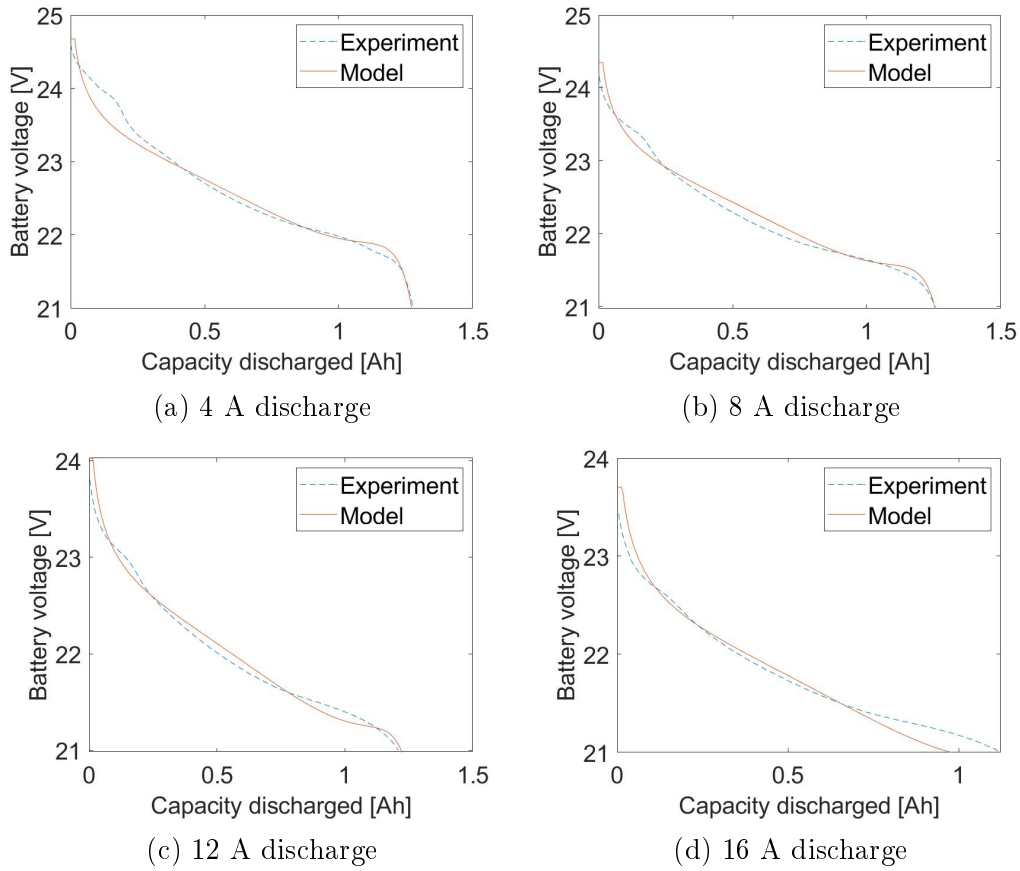


Figure D.2: Constant-current discharge data

required, especially as it is no longer the industry standard. So as an alternative, a similar battery was tested and modelled according to Section 3.3.3 (results shown in Table D.1 and Figure D.2). Some of the model parameters were then altered to better match Gong's results. These modified parameters are listed in Table D.2.

Table D.2: Battery model parameters altered to better data in Section 3.4

	Parameter values	
Parameters	Value from model fit	Altered value
R	0.0812	0.17
V_0	24.9942	25.3
C_n	1.3650	0.815 (if starting voltage = 23 V) 1.03 (otherwise)

Appendix E

Simulation with power management system

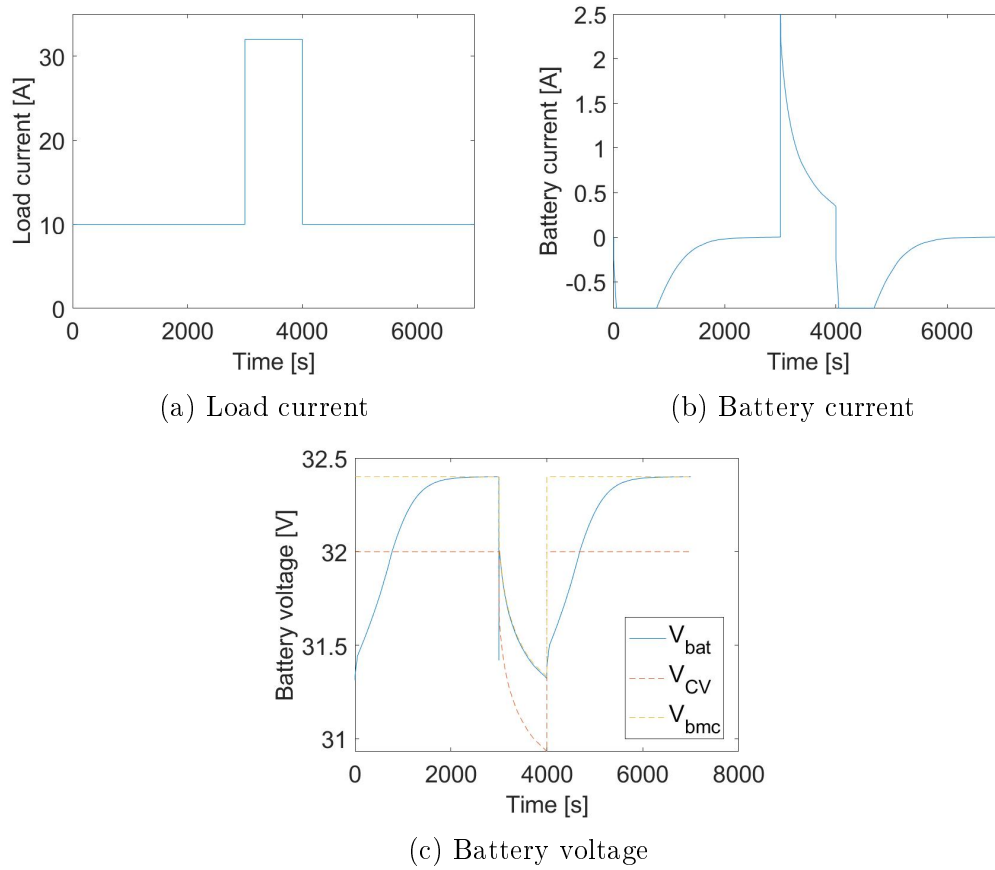


Figure E.1: Validating phase 3 (Equation 3.21)

Three different simulations were run. The first one is shown in Figure E.1 with the load current applied shown in Figure E.1a. The aim of this simulation

is to show that charge cycle can repeat itself, with the three phases (Equations 3.24d to 3.24f) being implemented. It can be seen that the first 50 seconds, phase 1 occurs, with the increasing charging current (Figure E.1b), followed by a period of constant current charge (Phase 2). When $V_{bat} \geq V_{CV}$ (in Figure E.1c), Phase 3 occurs with the charging current decreasing asymptotically to zero. The battery then discharges due to the increased load current, and then charges again with the same 3 phase process, when the load current is decreased.

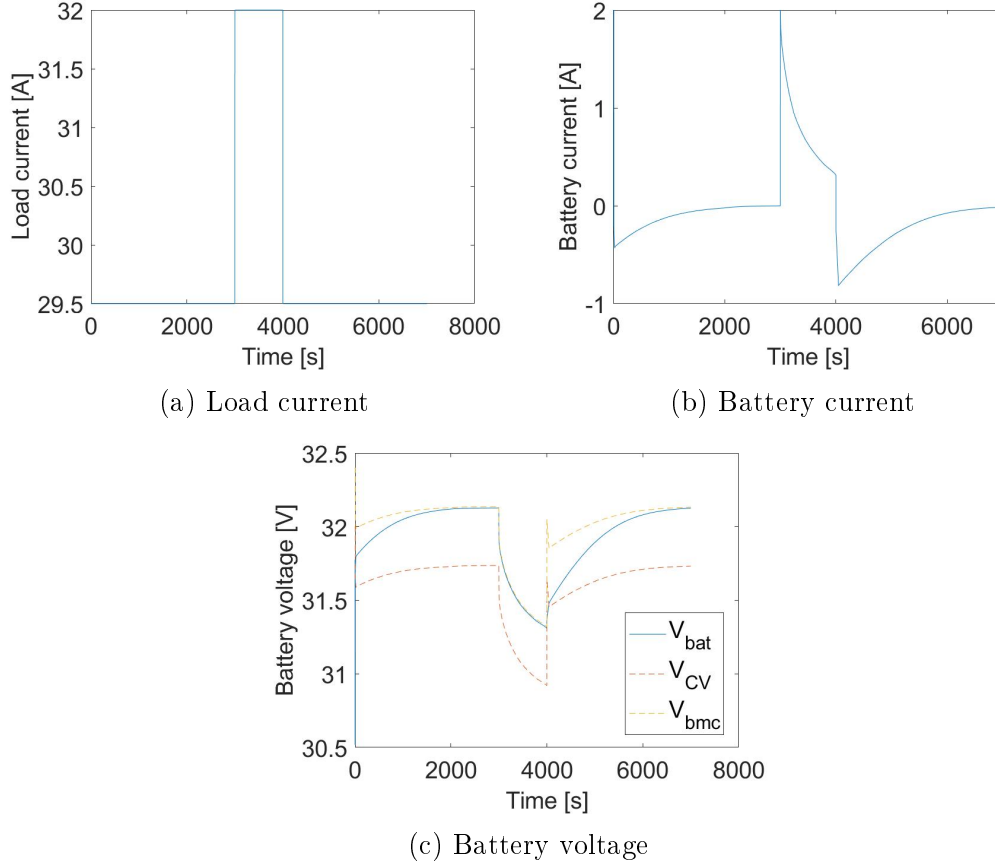


Figure E.2: Validating phase 3 (Equation 3.21)

The second simulation is shown in Figure E.2. This simulation is similar to the one shown in Figure E.1. However, the fuel cell voltage, V_{FC} , drops below V_{bmc} . This simulation shows that Equations 3.24a and 3.24b are implemented. As seen in Figure E.2c, it mostly occurs that $V_{CV} \leq V_{bat} \leq V_{bmc}$, resulting in Phase 3 mostly occurring (Shown in Figure E.2a). The maximum battery voltage is 32.13 V, compared to 32.4 V in the previous simulation (Figure E.1c).

The third simulation is shown in Figure E.3. The aim of this simulation is to validate the implementation of Equation 3.24c. Only phase 1 and 2 occurs

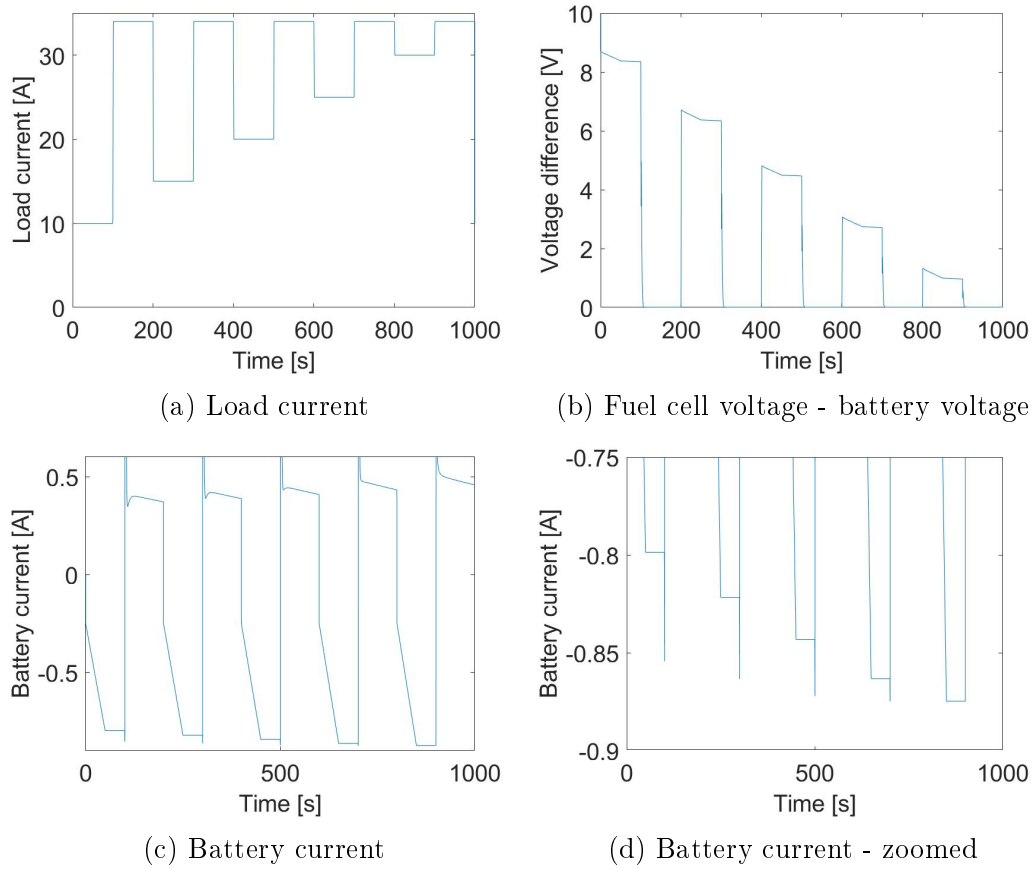


Figure E.3: Validating phase 1 and 2 with different load currents (Equation 3.22)

in this simulation, as the battery voltage remains below V_{CV} . The battery charges when the load current is low enough, causing there to be a voltage difference between the fuel cell and battery. This lower load current value is altered (Figure E.3a), causing the voltage difference to change (Figure E.3b), causing the charge current to change (Figure E.3c), as prescribed by Equation 3.24c.

Appendix F

Mechanical motor model and propeller model constants

Table F.1: Mechanical motor model and propeller model constants

ESC Model	Motor model	KV value	Motor friction	
			$C_{f,viscous}$	$C_{f,coulomb}$
Alpha 60A HV	U8 Lite	85	1.3615E-05	4.4875E-02
		100	4.9362E-04	5.8961E-02
Alpha 60A LV		150	7.1195E-06	6.2624E-02
		190	4.8842E-06	9.0040E-02
Alpha 60A HV	MN705-S	125	1.3547E-03	1.2396E-06
Flame 60A HV		260	9.1215E-04	4.3771E-02

	Propeller torque constant, C_Q
Friction modelled	7.4458E-05
Friction not modelled	8.1740E-05

Propeller thrust constant, C_T
1.8820E-03

Appendix G

Validation of ESC model

For an ESC, a model does exist, and has been validated (Gong and Verstraete, 2017a). However it isn't practical to implement this model in this work. That is because Gong's model is an equation, and the other component models are electrical circuits. Therefore, the approach is to develop an equivalent circuit model and then use Gong's data to obtain the unknown parameters and validate the model.

G.1 Description of model

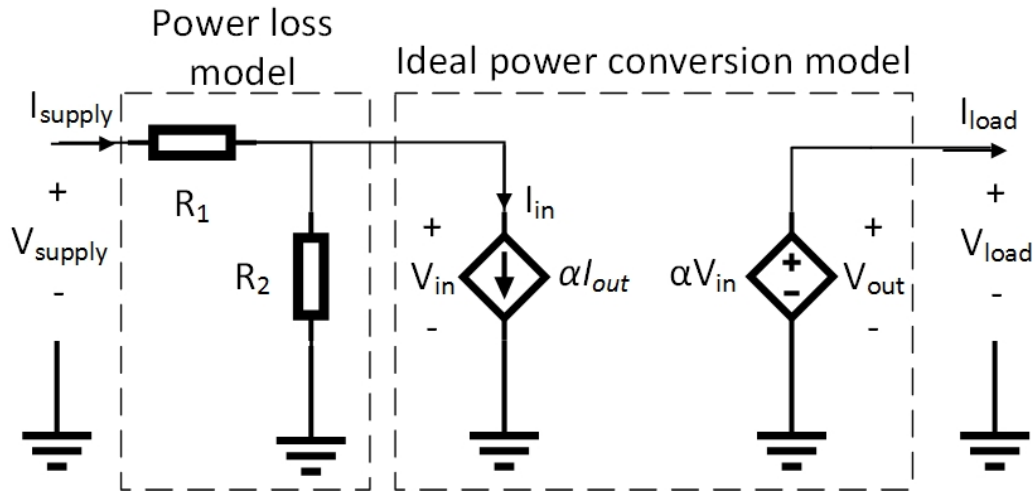


Figure G.1: ESC equivalent circuit model

The proposed ESC model is shown in Figure G.1. It is based on a DC-DC converter model (reviewed in Section 2.3.1.3), with the author's own modification. The model is divided into the *power loss model* and the *ideal power conversion model*. The input to the model is the throttle value, α , a value

between 0 and 1. The unknowns constants are R_1 and R_2 . In the system model, the V_{supply} terminal is connected to the output of the PMS model. The V_{load} terminal is connected to the motor model.

There will be two levels of complexity of this model, namely the *simple model*, M_S , and the *complex model*, M_C . With M_S , the constants R_1 and R_2 are independent of V_{supply} . With M_C , the constants R_1 and R_2 are dependent on V_{supply} .

The *ideal power conversion model* won't be validated. Only the *power loss model* is of interest. It must be noted that the efficiency of the *power loss model* is equal to the efficiency of the total ESC model. Therefore, if the efficiency of the *power loss model* is validated, the complete ESC model is validated. The efficiency of the *power loss model* is defined as:

$$\begin{aligned}\eta &= \frac{P_{in}}{P_{supply}} \\ &= \frac{V_{in}I_{in}}{V_{supply}I_{supply}}\end{aligned}\tag{G.1}$$

The resulting ESC efficiency model is therefore the *power loss model* in Figure G.1 combined with Equation G.1.

G.2 Data used

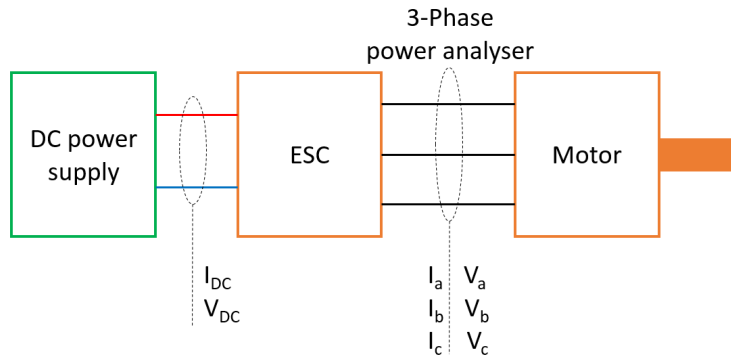


Figure G.2: Experimental setup. Adapted from (Gong and Verstraete, 2017a)

Gong tested different ESC's with the same motor, and measured the ESC efficiency. The author's varied the supply voltage with integer values of 7 - 12 V. The author's varied the motor throttle, thereby varying the supply current, from about 0.5 A to 15 A. The experimental setup is shown in Figure G.2, with the details of the setup listed in Table G.1.

It would have been ideal to simply fit the model in Section G.1 to Gong's data. However, the data is obtained for a limited current range. In Gong's

Table G.1: Details of experimental setup. Adapted from (Gong and Verstraete, 2017a)

Component	Detail
3-Phase power analyser	Magtrol 6530
ESC	Turnigy Aerostar 50 A
Motor	Turnigy Propdrive 3530 1100 kV
Propeller	Turnigy 10 x 4.5" plastic

data, the efficiency simply levels off. However, it was found by Harrington and Kroninger (2013) that the efficiency decreases with increasing torque (which is proportional to current). It was therefore decided to use the model that Gong fit to his data, and extrapolate it for higher current values.

Gong's model is as follows:

$$\eta = \frac{a \cdot I_{supply}^2}{V_{supply}} + b + \frac{c}{I_{supply}} + \frac{d}{V_{supply}} \quad (G.2)$$

The ESC data with the best fit is the Aerostar 50 A. It has an R^2 value of 0.9466, with the following constants: $a = -0.1295$, $b = 86.63$, $c = -20.40$ and $d = 15.28$.

G.3 Fitting and validating model

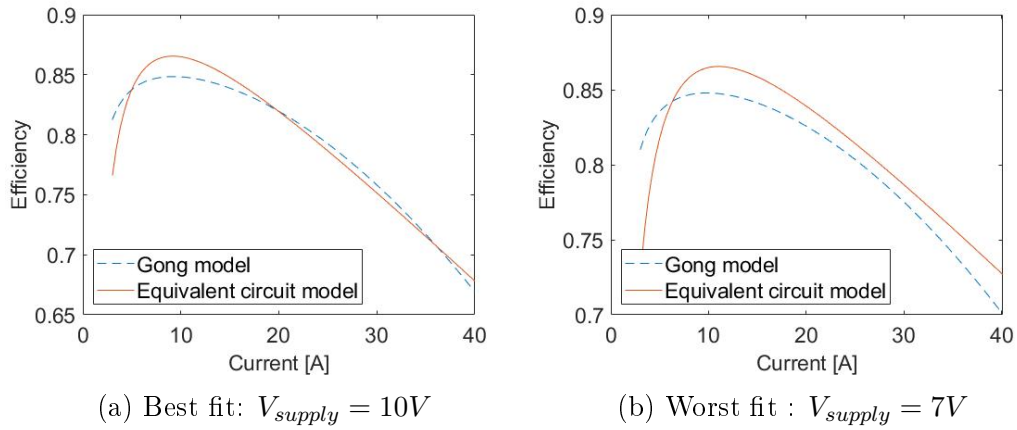


Figure G.3: Comparison between Gong model and equivalent circuit model - simple model

Model parameters are obtained for the *simple model*, M_S , and the *complex model*, M_C . Matlab's *parameter estimation* is used. The input is I_{supply} . The output is the efficiency. Calculated values from Equation G.2 with $I_{supply} = 3 - 40A$ and $V_{supply} = 7 - 12V$ (integer values) is the experimental output

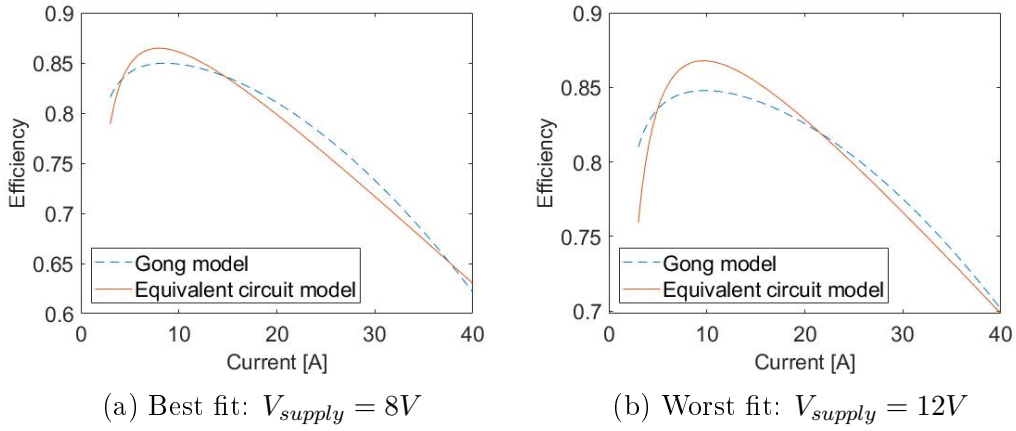


Figure G.4: Comparison between Gong model and equivalent circuit model - complex model

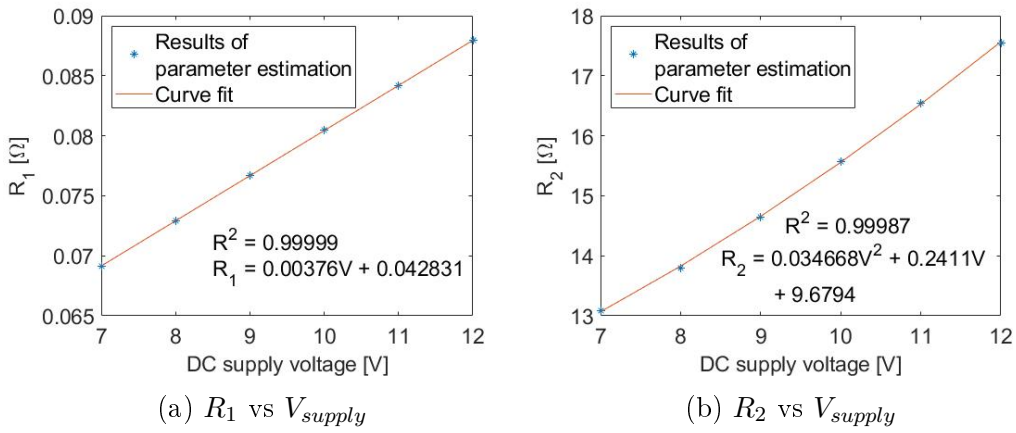


Figure G.5: Estimated parameters for different supply voltages - complex model

data. The best and worst fit for M_S and M_C is shown in Figures G.3 and G.4 respectively. The constants obtained for M_C is shown in Figure G.5, with the relationship versus V_{supply} . A comparison between M_S and M_C is shown in Figure G.6.

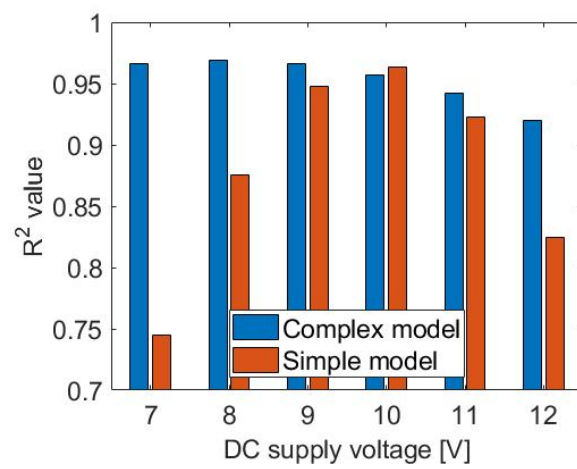


Figure G.6: Comparison between accuracy of complex model and simple model

Appendix H

Propulsor system modelling - additional data

This appendix provides additional data on the resulting complex and simple models fit in Section 4.1.4. Table H.1 compares the motor values obtained from *parameter estimation* with the manufacturer's values. Table H.2 provides the model constants and summary of equations for the complex model, while Table H.3 provides the same for the simple model.

Table H.1: Model parameters: comparing values obtained from model fit to manufacturer-provided values

ESC model	Motor model	Motor parameter	Manufacturer value	Estimated value	Percentage difference
Alpha 60 A HV	U8 Lite KV85	K_V [rpm/V]	85.00	84.75	-0.29
	U8 Lite KV100		100.00	103.75	3.75
Alpha 60 A LV	U8 Lite KV150		150.00	150.10	0.07
	U8 Lite KV190		190.00	181.61	-4.42
Alpha 60 A HV	U8 Lite KV85	I_0 [A]	0.50	0.43	-14.79
	U8 Lite KV100		0.70	0.60	-15.00
Alpha 60 A LV	U8 Lite KV150		1.00	0.95	-5.16
	U8 Lite KV190		1.30	1.36	4.99
Alpha 60 A HV	U8 Lite KV85	R_{motor} [mΩ]	225.00 (±5)	191.25	-12.78
	U8 Lite KV100		170.00(±5)	144.50	-12.06
Alpha 60 A LV	U8 Lite KV150		85.00(±5)	79.50	0.59
	U8 Lite KV190		47.00(±3)	49.80	0

Table H.2: Complex propulsor model values

Components	Model figure reference	Equations	Component name	Constants
ESC	Figure 4.8	$V_{out} = \alpha V_{in}$ (2.13) $I_{in} = \alpha I_{out}$ (2.14)	Alpha 60 A HV with U8 Lite KV85	$R_1 = 0.57438 \Omega$ $R_2 = 576.88 \Omega$
			Alpha 60 A HV with U8 Lite KV100	$R_1 = 0.4113 \Omega$ $R_2 = 599.3 \Omega$
			Alpha 60 A LV with U8 Lite KV150	$R_1 = 0.2032 \Omega$ $R_2 = 591.6 \Omega$
			Alpha 60 A LV with U8 Lite KV190	$R_1 = 0.1484 \Omega$ $R_2 = 54.679 \Omega$
Motor (electrical)	Figure 2.13	$T_{motor} = K I_{conv}$ (2.15) $V_{conv} = K \omega_{motor}$ (2.16) $K = \frac{1}{KV} \frac{60}{2\pi}$ (2.17)	U8 Lite KV85	$KV = 84.75 \text{ rpm/V}$ $I_0 = 0.42605 \text{ A}$ $R_{motor} = 0.19125 \Omega$
			U8 Lite KV100	$KV = 103.75 \text{ rpm/V}$ $I_0 = 0.59502 \text{ A}$ $R_{motor} = 0.1445 \Omega$
			U8 Lite KV150	$KV = 150.1 \text{ rpm/V}$ $I_0 = 0.9484 \text{ A}$ $R_{motor} = 0.0795 \Omega$
			U8 Lite KV190	$KV = 181.61 \text{ rpm/V}$ $I_0 = 1.3649 \text{ A}$ $R_{motor} = 0.0498 \Omega$

Table H.2: Complex propulsor model values

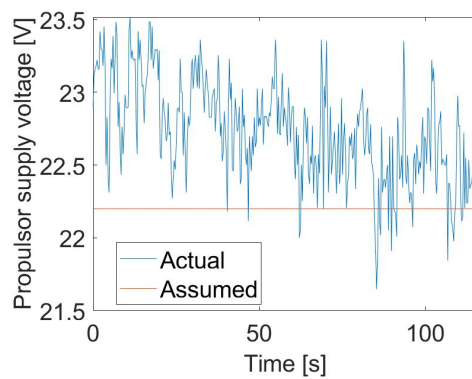
Components	Model figure reference	Equations	Component name	Constants
Motor (mechanical) /propeller	Figure 4.3	$Q_{motor} = C_Q \rho D^5 \omega^2 + C_{f,viscous} \omega + C_{f,coulomb} \quad (4.3)$ $T = C_T \rho D^4 \omega^2 \quad (4.6)$	Glossy propeller	$C_Q = 7.4458 \cdot 10^{-5}$ $C_T = 1.8820 \cdot 10^{-3}$
			U8 Lite KV85	$C_{f,viscous} = 1.3615 \cdot 10^{-5} \text{ Nm/(rad/s)}$ $C_{f,coulomb} = 4.4875 \cdot 10^{-2} \text{ Nm}$
			U8 Lite KV100	$C_{f,viscous} = 4.9362 \cdot 10^{-4} \text{ Nm/(rad/s)}$ $C_{f,coulomb} = 5.8961 \cdot 10^{-2} \text{ Nm}$
			U8 Lite KV150	$C_{f,viscous} = 7.1195 \cdot 10^{-6} \text{ Nm/(rad/s)}$ $C_{f,coulomb} = 6.2624 \cdot 10^{-2} \text{ Nm}$
			U8 Lite KV190	$C_{f,viscous} = 4.8842 \cdot 10^{-6} \text{ Nm/(rad/s)}$ $C_{f,coulomb} = 9.0040 \cdot 10^{-2} \text{ Nm}$

Table H.3: Simple propulsor model values

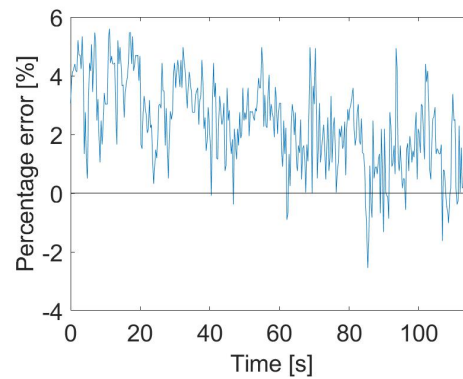
Components	Model figure reference	Equations	Component name	Constants
ESC	Figure 4.8	$V_{out} = \alpha V_{in}$ (2.13) $I_{in} = \alpha I_{out}$ (2.14)	Alpha 60 A HV	$R_1 = 0.36017 \Omega$ $R_2 = 964.01 \Omega$
			Alpha 60 A LV	$R_1 = 0.19757 \Omega$ $R_2 = 910.33 \Omega$
Motor (electrical)	Figure 2.13	$T_{motor} = K I_{conv}$ (2.15) $V_{conv} = K \omega_{motor}$ (2.16) $K = \frac{1}{KV} \frac{60}{2\pi}$ (2.17)	U8 Lite KV85	$KV = 85 \text{ rpm/V}$ $I_0 = 0.5 \text{ A}$ $R_{motor} = 0.225 \Omega$
			U8 Lite KV100	$KV = 100 \text{ rpm/V}$ $I_0 = 0.7 \text{ A}$ $R_{motor} = 0.17 \Omega$
			U8 Lite KV150	$KV = 150 \text{ rpm/V}$ $I_0 = 1.0 \text{ A}$ $R_{motor} = 0.085 \Omega$
			U8 Lite KV190	$KV = 190 \text{ rpm/V}$ $I_0 = 1.3 \text{ A}$ $R_{motor} = 0.047 \Omega$
Propeller	Figure 4.3	$Q_{motor} = C_Q \rho D^5 \omega^2$ (4.3) $T = C_T \rho D^4 \omega^2$ (4.6)	Glossy propeller	$C_Q = 8.1740 \cdot 10^{-5}$ $C_T = 1.8820 \cdot 10^{-3}$

Appendix I

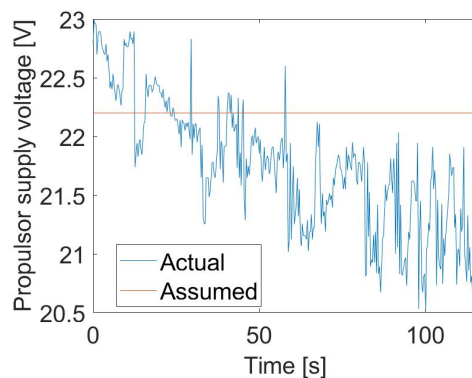
Thrust duty cycle converting - additional data



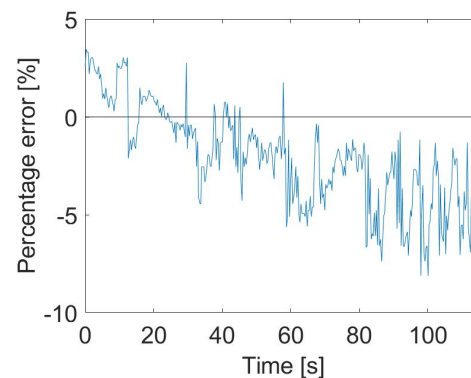
(a) Voltage - 5.976 kg flight



(b) % error - 5.976 kg flight



(c) Voltage - 7.976 kg flight



(d) % error - 7.976 kg flight

Figure I.1: Battery voltage measured during flight

List of References

- (2016). EnergyOr signs UAV joint development deal with French Air Force. *Fuel Cells Bulletin*, vol. 2016, no. 4, pp. 4–5. ISSN 14642859.
- (2017). {UAV} market takes off for Intelligent Energy in inventory solutions. *Fuel Cells Bulletin*, vol. 2017, no. 4, pp. 4–5. ISSN 1464-2859.
Available at: <http://www.sciencedirect.com/science/article/pii/S1464285917301426>
- Ampatis, C. and Papadopoulos, E. (2014). Parametric Design and Optimization of Multi-Rotor Aerial Vehicles. *Springer Optimization and Its Applications*, vol. 91, no. 3, pp. 1–25. ISSN 19316836.
- Barbir, F. (2013a). Chapter nine - fuel cell system design. In: Barbir, F. (ed.), *PEM Fuel Cells (Second Edition)*, second edition edn, pp. 305 – 372. Academic Press, Boston. ISBN 978-0-12-387710-9.
Available at: <http://www.sciencedirect.com/science/article/pii/B9780123877109000096>
- Barbir, F. (2013b). Chapter one - introduction. In: Barbir, F. (ed.), *PEM Fuel Cells (Second Edition)*, second edition edn, pp. 1 – 16. Academic Press, Boston. ISBN 978-0-12-387710-9.
Available at: <http://www.sciencedirect.com/science/article/pii/B9780123877109000011>
- Benito, J.A., Glez-de Rivera, G., Garrido, J. and Ponticelli, R. (2014). Design considerations of a small UAV platform carrying medium payloads. *Proceedings of the 2014 29th Conference on Design of Circuits and Integrated Systems, DCIS 2014*.
- Bershadsky, D., Haviland, S. and Johnson, E.N. (2016). Electric Multirotor UAV Propulsion System Sizing for Performance Prediction and Design Optimization. *57th AIAA/ASCE/AHS/ASC Structures, Structural Dynamics, and Materials Conference*, pp. 1–22.
Available at: <http://arc.aiaa.org/doi/10.2514/6.2016-0581>
- Blackwelder, M.J. and Dougal, R.A. (2004). Power coordination in a fuel cell-battery hybrid power source using commercial power controller circuits. *Journal of Power Sources*, vol. 134, no. 1, pp. 139–147. ISSN 03787753.

- Botha, R. (2018). Economic Impact of the SA drone industry. In: *DroneCon*. Available at: <https://dronecon.co.za/wp-content/uploads/2018/05/DroneCon-2018-Dr-Roelof-Botha.pdf>
- Bradley, T.H., Moffitt, B.A., Fuller, T.F., Mavris, D. and Parekh, D.E. (2008). Design Studies for Hydrogen Fuel Cell Powered Unmanned Aerial Vehicles. *Design*, , no. August, pp. 1–16. ISSN 0730725X (ISSN).
- Carri, J. (2018 11). A four-constant model for electric motors (draft no. 2).
- Chen, Y.S., Lin, S.M. and Hong, B.S. (2013). Experimental study on a passive fuel Cell/Battery hybrid power system. *Energies*, vol. 6, no. 12, pp. 6413–6422. ISSN 19961073.
- DJI (2017). Matrice 100: Quadcopter for Developers. Available at: <http://www.dji.com/matrice100/info{#}specs>
- DJI (2018a). DJI - The World Leader in Camera Drones/Quadcopters for Aerial Photography. Available at: <https://www.dji.com/matrice100/info>
- DJI (2018b). Matrice 600 Pro- Simply Professional Performance. Available at: <http://www.dji.com/matrice600>
- DroneTec (2018). The UAV. Available at: <http://www.dronetec.co.za/the-uav/>
- Du, T., Schulz, A., Zhu, B., Bickel, B. and Matusik, W. (2016). Computational multicopter design. *ACM Transactions on Graphics*, vol. 35, no. 6, pp. 1–10. ISSN 07300301. Available at: <http://dl.acm.org/citation.cfm?doid=2980179.2982427>
- EnergyOR (2016). H2QUAD 1000. Available at: <http://energyor.com/products/detail/h2quad-1000>
- EnergyOr (2018). EnergyOr H2Quad 400H2. Available at: <http://energyor.com/products/detail/h2quad-400>
- Enrique, J.M., Barragán, A.J., Durán, E. and Andújar, J.M. (2017). Theoretical Assessment of DC/DC Power Converters' Basic Topologies. A Common Static Model. *Applied Sciences*, vol. 8, no. 1, p. 19. ISSN 2076-3417. Available at: <http://www.mdpi.com/2076-3417/8/1/19>
- Erickson, R.W. (). DC-DC Power Converters.
- Eva Saadé Latorre (2011). Master thesis. Propulsion system optimization for an unmanned lightweight quadrotor. *Mycotoxin research*, vol. 6, no. 2, p. 100. ISSN 0178-7888. Available at: <http://www.ncbi.nlm.nih.gov/pubmed/21365933>

- Farag, M.S. (2013). Lithium-Ion Batteries: Modelling and State of Charge Estimation. p. 169.
- FlightWave (2018). Jupiter UAS Bundle Reservation.
Available at: <https://www.flightwave.aero/product/jupiter-uas-bundle-reservation/>
- Gartner (2013). Gartner Hype Cycle.
Available at: <http://www.gartner.com/technology/research/methodologies/hype-cycle.jsp>
- Gatti, M., Giulietti, F. and Turci, M. (2015). Maximum endurance for battery-powered rotary-wing aircraft. *Aerospace Science and Technology*, vol. 45, no. September, pp. 174–179. ISSN 12709638.
Available at: <http://dx.doi.org/10.1016/j.ast.2015.05.009>
- Gens Ace Tattu (). Tattu 1300mAh 4S 75C Lipo Battery Pack with XT60 Plug - Gens Ace.
Available at: <http://www.gensace.de/tattu-1300mah-14-8v-75c-4s1p-lipo-battery-pack.html>
- Goldman Sachs (2016). Drones - Reporting for Work.
Available at: <http://www.goldmansachs.com/our-thinking/technology-driving-innovation/drones/>
- Gong, A. and Verstraete, D. (2017a). Experimental testing of electronic speed controllers for UAVs. *53rd AIAA/SAE/ASEE Joint Propulsion Conference, 2017*, , no. July.
- Gong, A. and Verstraete, D. (2017b). Fuel cell propulsion in small fixed-wing unmanned aerial vehicles: Current status and research needs. *International Journal of Hydrogen Energy*, vol. 42, no. 33, pp. 21311–21333. ISSN 03603199.
Available at: <http://dx.doi.org/10.1016/j.ijhydene.2017.06.148>
- Gong, A. and Verstraetey, D. (2014). Role of battery in a hybrid electrical fuel Cell UAV propulsion system. *52nd AIAA Aerospace Sciences Meeting - AIAA Science and Technology Forum and Exposition, SciTech 2014*, , no. January 2014.
- Green, C.R. and McDonald, R.A. (2015). Modeling and Test of the Efficiency of Electronic Speed Controllers for Brushless DC Motors. *15th AIAA Aviation Technology, Integration, and Operations Conference*, , no. June, pp. 1–10.
Available at: <http://arc.aiaa.org/doi/10.2514/6.2015-3191>
- Guangming, L., Lu, L., Hong, F., Jianfeng, H., Li, J., Ouyang, M., Yanjing, W., Shan, X. and Ping, C. (2014). A comparative study of equivalent circuit models and enhanced equivalent circuit models of lithium-ion batteries with different model structures. *Transportation Electrification Asia-Pacific (ITEC Asia-Pacific), 2014 IEEE Conference and Expo*, pp. 1–6.

- Guinn, C. and Schauble, O. (2018). State of the drone industry 2018 report. Tech. Rep., Guinn Partners.
Available at: <https://drive.google.com/file/d/1XyQcPwT0TFV1By4o8An1AF1hUEh-apge/view>
- Han, J., Charpentier, J.F. and Tang, T. (2014). An energy management system of a fuel cell/battery hybrid boat. *Energies*, vol. 7, no. 5, pp. 2799–2820. ISSN 19961073.
- Harrington, A.M. and Kroninger, C. (2013). Characterization of Small DC Brushed and Brushless Motors. , no. March.
- He, H., Xiong, R. and Fan, J. (2011). Evaluation of lithium-ion battery equivalent circuit models for state of charge estimation by an experimental approach. *Energies*, vol. 4, no. 4, pp. 582–598. ISSN 19961073.
- Horizon Energy Systems (). Series F: 300 bar cylinders. Tech. Rep..
Available at: https://docs.wixstatic.com/ugd/c65691f_ae125f5f510648e4b998a5e8c887683c.pdf
- Horizon Energy Systems (2012). AEROPAK Fuel cell-enabled power supply for electric mini-UAS // evaluation unit TECHNICAL DATA SHEET.
Available at: <http://resources.arcolaenergy.com/docs/TechnicalDataSheets/AEROPAKTechnicalDataSheet.pdf>
- Horizon Energy Systems (2014). Aerostak AST01-01 (200W).
- Horizon Energy Systems (2018). HYCOPTER: Hydrogen powered multirotor.
Available at: <https://www.hes.sg/hycopter>
- Howroyd, S. and Chen, R. (2016). Powerpath controller for fuel cell & battery hybridisation. *International Journal of Hydrogen Energy*, vol. 41, no. 7, pp. 4229–4238. ISSN 03603199.
Available at: <http://dx.doi.org/10.1016/j.ijhydene.2016.01.038>
- Hoy, G.V. and Kutnick, D. (2017). Hype Cycle for Drones and Mobile Robots, 2017.
Available at: <https://www.gartner.com/doc/3774064/hype-cycle-drones-mobile-robots>
- Hunt, G. (2003). FreedomCAR Battery Test Manual For Power-Assist Hybrid Electric Vehicles. Tech. Rep., Environmental Idaho National Engineering and Laboratory.
Available at: https://avt.inl.gov/sites/default/files/pdf/battery/freedomcar_manual_04_15_03.pdf
- Hussein, A.A.H. and Batarseh, I. (2011). An overview of generic battery models. *IEEE Power and Energy Society General Meeting*, , no. 4, pp. 4–9. ISSN 19449925.
- Infineon (2016). Drone Electronic Speed Controller (ESC) with XMC ? , Gate Driver , OptiMOS ? , no. October.

- Intelligent Energy (2017). UAV Fuel Cell Module.
Available at: <https://www.intelligent-energy.com/uploads/product{ }docs/Final{ }UAV{ }brochure{ }web{ }version{ }OzCFad1.pdf>
- Jackey, R., Saginaw, M., Sanghvi, P., Gazzarri, J., Huria, T. and Ceraolo, M. (2013). Battery Model Parameter Estimation Using a Layered Technique: An Example Using a Lithium Iron Phosphate Cell. , no. April. ISSN 2013011547.
Available at: <http://papers.sae.org/2013-01-1547/>
- Johnson, V. (2002). Battery performance models in ADVISOR. *Journal of Power Sources*, vol. 110, no. 2, pp. 321–329. ISSN 03787753.
Available at: <http://linkinghub.elsevier.com/retrieve/pii/S0378775302001945>
- KDE Direct (). KDE Direct XF CF Brushless Performance Testing - KDE7208XF-135.
Available at: <https://cdn.shopify.com/s/files/1/0496/8205/products/KDE{ }Direct{ }XF{ }CF{ }Brushless{ }Performance{ }Testing{ }-{ }KDE7208XF-135.png?v=1526322483>
- Kuantama, E., Craciun, D., Tarca, I. and Tarca, R. (2017 10). Quadcopter propeller design and performance analysis.
- Lai, X., Zheng, Y. and Sun, T. (2018). A comparative study of different equivalent circuit models for estimating state-of-charge of lithium-ion batteries. *Electrochimica Acta*, vol. 259, pp. 566–577. ISSN 00134686.
Available at: <https://doi.org/10.1016/j.electacta.2017.10.153>
- Lu, Z., Yu, X., Zhang, L., Meng, X., Wei, L. and Jin, L. (2017). Experimental investigation on the charge-discharge performance of the commercial lithium-ion batteries. *Energy Procedia*, vol. 143, pp. 21–26. ISSN 18766102.
Available at: <https://doi.org/10.1016/j.egypro.2017.12.642>
- Magnussen, Ø., Hovland, G. and Ottestad, M. (2014). Multicopter UAV design optimization. *MESA 2014 - 10th IEEE/ASME International Conference on Mechatronic and Embedded Systems and Applications, Conference Proceedings*. ISSN 1083-4435.
- Marshall, D.M., Barnhart, R.K., Shappee, E. and Most, M. (2016). *Introduction to Unmanned Aircraft Systems*. second edi edn. CRC. ISBN 9781482263930.
Available at: <https://catalog.loc.gov/vwebv/search?searchCode=LCCN{&}searchArg=2015036667{&}searchType=1{&}permalink=y>
- Mathworks (). Implement DC chopper model for DC motor drives - Simulink.
Available at: <https://www.mathworks.com/help/physmod/sps/powersys/ref/chopper.html>
- Mathworks (2008). Battery: Implement generic battery mode.
Available at: <https://www.mathworks.com/help/physmod/sps/powersys/ref/battery.html>

- Mauro Gatti (2015). Design and Prototyping High Endurance Multi-Rotor. p. 67.
- MMC (2016). MMC Powerful Hydrogen H1-Fuel Cell.
- Mocera, F. and Vergori, E. (2018). Study and identification of the thermo-electric behavior of lithium-ion batteries for electric vehicles. *Procedia Structural Integrity*, vol. 8, pp. 126–136. ISSN 24523216.
Available at: <http://linkinghub.elsevier.com/retrieve/pii/S2452321617305073>
- Moffitt, B., Bradley, T., Parekh, D. and Mavris, D. (2006). Design and Performance Validation of a Fuel Cell Unmanned Aerial Vehicle. *44th AIAA Aerospace Sciences Meeting and Exhibit*, , no. November 2015. ISSN 01463705.
Available at: <http://arc.aiaa.org/doi/10.2514/6.2006-823>
- Moffitt, B.A., Bradley, T.H., Mavris, D. and Parekh, D.E. (2007). Reducing Uncertainty of a Fuel Cell UAV through Variable Fidelity Optimization. *AIAA Journal*, pp. 1–19.
- Müller, M. (). eCalc - xcopterCalc - the most reliable Multicopter Calculator on the Web.
Available at: <https://www.ecalc.ch/xcoptercalc.php?ecalc{&}lang=en>
- Nejad, S., Gladwin, D.T. and Stone, D.A. (2016). A systematic review of lumped-parameter equivalent circuit models for real-time estimation of lithium-ion battery states. *Journal of Power Sources*, vol. 316, pp. 183–196. ISSN 03787753.
Available at: <http://dx.doi.org/10.1016/j.jpowsour.2016.03.042>
- Nishizawa, A., Kallo, J., Garrot, O. and Weiss-Ungeth??m, J. (2013). Fuel cell and Li-ion battery direct hybridization system for aircraft applications.
- Plett, G.L. (2004). Extended Kalman filtering for battery management systems of LiPB-based HEV battery packs - Part 2. Modeling and identification. *Journal of Power Sources*, vol. 134, no. 2, pp. 262–276. ISSN 03787753.
- Plett, G.L. (2018). Equivalent-Circuit Cell Models. pp. 1–33.
- PWC (2016). Clarity from above PwC global report on the commercial applications of drone technology. *Drone Powered Solutions*, , no. May, p. 3/40.
Available at: www.dronepoweredolutions.com
- Rahmoun, A. and Biechl, H. (2012). Modelling of Li-ion batteries using equivalent circuit diagrams. *Przegląd Elektrotechniczny*, vol. 2, no. 7, pp. 152–156. ISSN 0033-2097.
Available at: <http://red.pe.org.pl/articles/2012/7b/40.pdf>
- Ramya, R. and Krishna Kumar, V. (2016). Implementation of three phase switched boost inverter for induction motor drive. *International Journal of Control Theory and Applications*, vol. 9, no. 5, pp. 2249–2255. ISSN 09745572.

- Rößler, C. (2012). *Conceptual Design of Unmanned Aircraft with Fuel Cell Propulsion System*. Ph.D. thesis.
Available at: <https://www.dr.hut-verlag.de/978-3-8439-0406-3.html>
- Silvagni, M., Chiaberge, M. and Tessari, F. (2018). Advances in Service and Industrial Robotics. vol. 49. ISSN 22110992.
Available at: <http://link.springer.com/10.1007/978-3-319-61276-8>
- Sisco, J., Robinson, P. and Osenar, P. (2017). New Fuel Cell Technologies Extend Missions for Vertical Take-Off and Landing Unmanned Aerial Vehicles. pp. 1–17.
- T-motor (). U8 PRO KV135 - Specifications.
Available at: <http://store-en.tmotor.com/goods.php?id=326>
- T-motor (2017a). U10PLUS KV100 - Specifications.
Available at: <http://store-en.tmotor.com/goods.php?id=363>
- T-motor (2017b). U8 Lite KV150 - Specifications.
Available at: <http://store-en.tmotor.com/goods.php?id=469>
- Tao Du, Adriana Schulz, B.Z. (). Multicopter Design.
Available at: [https://github.com/mit-gfx/multicopter\[_\]design](https://github.com/mit-gfx/multicopter[_]design)
- Tremblay, O. and Dessaint, L.-a. (2009). Experimental Validation of a Battery Dynamic Model for EV Applications. vol. 3, pp. 289–298.
- Tsotoulidis, S.N. and Safacas, A.N. (2011). Analysis of a Drive System in a Fuel Cell and Battery powered Electric Vehicle. *International Journal of Renewable Energy Research (IJRER)*, vol. 1, no. 3, pp. 140–151. ISSN 13090127.
Available at: <http://www.ijrer.org/ijrer/index.php/ijrer/article/view/47>
- Turnigy (). Turnigy 1300mAh 3S 20C Lipo Pack.
Available at: [https://hobbyking.com/en\[_\]us/turnigy-1300mah-4s-45c-lipoly-pack.html](https://hobbyking.com/en[_]us/turnigy-1300mah-4s-45c-lipoly-pack.html)
- Wang, B. (2018). Hype Cycle for Drones and Mobile Robots, 2018.
Available at: <https://www.gartner.com/doc/3883167/hype-cycle-drones-mobile-robots>